Temporal and Spectral Characteristics of Active Galactic Nuclei in X-rays using NuSTAR

A thesis

submitted for the degree of

Doctor of Philosophy

in

The Department of Physics,

Pondicherry University,

Puducherry - 605 014, India

by

Priyanka Rani

Indian Institute of Astrophysics,

Bangalore - 560 034, India

February 2019

Temporal and Spectral Characteristics of Active Galactic Nuclei in X-rays using NuSTAR

Priyanka Rani
Indian Institute of Astrophysics

Indian Institute of Astrophysics

Bangalore - 560 034, India

Title of the thesis	:	**Temporal and Spectral Characteristics of Active Galactic Nuclei in X-rays using NuSTAR**
Name of the author	:	**Priyanka Rani**
Address	:	Indian Institute of Astrophysics II Block, Koramangala Bangalore - 560 034, India
Email	:	priyanka@iiap.res.in
Name of the supervisor	:	**Prof. C. S. Stalin**
Address	:	Indian Institute of Astrophysics II Block, Koramangala Bangalore - 560 034, India
Email	:	stalin@iiap.res.in

Declaration of Authorship

I hereby declare that the matter contained in this thesis is the result of the investigations carried out by me at the Indian Institute of Astrophysics, Bangalore, under the supervision of Prof. C. S. Stalin. This work has not been submitted for the award of any other degree, diploma, associateship, fellowship, etc. of any other university or institute.

Signed: ________________________________

Date: ________________________________

Certificate

This is to certify that the thesis entitled **'Temporal and Spectral Characteristics of Active Galactic Nuclei in X-rays using NuSTAR'** submitted to the Pondicherry University by Ms. Priyanka Rani for the award of the degree of Doctor of Philosophy, is based on the results of the investigations carried out by her under my supervision and guidance, at the Indian Institute of Astrophysics. This thesis has not been submitted for the award of any other degree, diploma, associateship, fellowship, etc. of any other university or institute.

Signed: ____________________________

Date: ____________________________

List of Publications

1. **Priyanka Rani** & C. S. Stalin,'Hard X-ray flux variations in AGN from NuSTAR', ASI Conference Series, 2015, Vol. 12, pp 135−136.

2. **Priyanka Rani**, C.S Stalin & Suvendu Rakshit, 'X-ray flux Variability of Active Galactic Nuclei Observed using NuSTAR, 2017', *Monthly Notices of the Royal Astronomical Society*, 466, 3309.*

3. **Priyanka Rani** & C. S. Stalin, 'Measurement of coronal properties of Seyfert galaxies from NuSTAR hard X-ray spectrum, 2018', *Journal of Astrophysics and Astronomy*, 39, 15.†

4. **Priyanka Rani** & C. S. Stalin, 'Coronal Properties of the Seyfert1 Galaxy 3C 120 with NuSTAR, 2018', *The Astrophisical Journal*, 856, 120.‡

5. **Priyanka Rani**, C. S. Stalin & K. D. Goswami, 'Study of X-ray variability and coronae of Seyfert galaxies using NuSTAR, 2019', *Monthly Notices of the Royal Astronomical Society.* 484, 5113.§

6. **Priyanka Rani**, C. S. Stalin, Divyajyoti Saha & Suvendu Rakshit, 'A comparative study of the X-ray flux variability characteristics of different classes of AGN with NuSTAR', *under review in Monthly Notices of the Royal Astronomical Society.*¶

---

*presented in Chapter 3
†presented in Chapter 4 and 5
‡presented in Chapter 4
§presented in Chapter 5
¶presented in Chapter 3

Presentations

1. Oral presentation in the *Recent Trends in the Study of Compact Objects*, ARIES, Nanital, during May 2015.

2. Oral presentation in the *Extragalactic Relativistic Jets: Cause and Effect*, ICTS, Bangalore, during October 2015.

3. Oral presentation in the *Jet Triggering Mechanisms in Black Hole Sources*, TIFR, Mumbai, during January 2016.

4. Poster presentation in the *Astronomical Society of India meeting*, Kashmir University, Kashmir, during May 2016.

5. Oral presentation in the *Wide Band Spectral and Timing Studies of Cosmic X-ray Sources*, TIFR, Mumbai, during January 2017.

6. Oral presentation in *RETCO III*, IIST, Thiruvananthapuram, Kerala, during June 2017.

7. Poster presentation in *Unveiling the Physics Behind Extreme AGN Variability*, University of the Virgin Islands, USA, during July 2017.

8. Invited talk in *High Energy Emission from Active Galactic Nuclei*; University of Calicut, Kerala, during November 2017.

9. Invited participation in *Observing Universe with AstroSat*; MCNS, MAHE, Manipal, Karnataka, during September 2018.

Acknowledgements

I would like to express my sincerest gratitude and thanks to my thesis supervisor, Prof. C. S. Stalin. He has inspired and encouraged me to grow as a researcher during my entire tenure. A special mention of his early morning emails asking me to send the plots asap :-)

I would also like to thank the director IIA, all the academic and administrative staff including the Board of Graduate Studies, for their help and support in providing me a research friendly atmosphere. I thank my doctoral committee members and the administration of Pondicherry university for their help and inputs during various stages of my research. Special thanks to the IIA library team for providing the necessary books and journals whenever I needed.

My work would have been impossible without a great help from Suvendu, Bhoomika, Kshama, Amit and Aditi who also work/worked under my thesis supervisor. Working with all the project students Anju, Saikruba, Kaustav and Divyajyoti was a fun!

I had a very pleasant time in IIA and in Bhaskara hostel. All credits go to my colleagues and friends. Sudip and my ex-roommate Ramya were extremely helpful to boost my confidence in first year of my PhD. My batchmates Rubi, Prasanta, Avrajit and suman have been a consistent wellspring of help and motivation at IIA. I learnt playing Volleyball, Table Tennis and little bit of Cricket after coming to IIA and I had a great time with all the players, Selvan sir, Mohan Sir, Sudip, Varun, Sandeep, Avinash, Panini, Bhoomika, Manoj, Aneswh, Chayan, Prasanta, Phanindra, Subhankar, Tanmoy da, Partho, Soumya, Satabdwa, Ritesh, Vaibhav, Magesh, Samrat, Raghubar, Manoj Kumar, Deepak, Rubi, Sneha, Avrajit, Anirban Dutta, Sajal da, Sam da, Avijit da, Manju da, Arun da, Ashish Da, Prerna, Priya, Ekta, Deepthi, Manika, Jyoti, Athira. I also thank my favourite seniors

Susmitha, Sowmya, Supriya, Sangeetha, Honey and Ambily at IIA. Travelling together with Bhoomika, Kshama and Pavana to attend a conference was a lot of fun! I am very fortunate to make friends in IIA like Prerna, Priya, Sireesha, Ekta, Prasanta and Rubi who have been great source of support in my Ph.D. times specially when I had fractured my foot.

A special thanks to my cousin brother Amit bhaiya who has been always my motivation and inspired me to pursue higher studies.

Last but the most important, I owe a lot to my parents, Mr. Jai Prakash Singh and Mrs. Rakesh Devi. They have always encouraged, motivated and inspired me to pursue a research career and that too in Astrophysics. I should also mention my brother and sisters with whom I have shared uncountable memories: Shalu Di, Jijaji, Priti, Suruchi and my sweet little brother, Ritik. A Special thanks to an important person in my life, Dr. Sudip Mandal who has placed me ahead of everything else. He has also taught me the techniques and rules of many sports like cricket, football, volleyball and table tennis. My extended family, Mr. Atanu(Baba) and Mrs. Lakshmi Mondal(Maa), Didibhai, Jamai babu and Hapu have always been around for me. Thank you all for your help and support to see the completion of this thesis.

Priyanka Rani

Data usage

In this thesis, I have made use of data from the *NuSTAR* mission, a project led by the California Institute of Technology, managed by the Jet Propulsion Laboratory and funded by the National Aeronautics and Space Administration.

I would like to thank the *NuSTAR* Operations, Software and Calibration teams for support with the execution and analysis of these observations. This research has made use of the *NuSTAR* Data Analysis Software (NuSTARDAS) jointly developed by the ASI Science Data Center (ASDC, Italy) and the California Institute of Technology(USA).

Dedicated to

my

family, teachers and friends...

Abstract

Flux variability is one of the defining characteristics of active galactic nuclei (AGN). This has been known over the past six decades ever since the discovery of quasars in 1963. Since then AGN have been observed for flux variability over all accessible wavelengths on a range of timescales from hours to days and months. Studying flux variability of AGN is important as it is a effective tool to probe the central regions of AGN that are not accessible by any current imaging techniques set by $R_s < c \times t_{var}$, where t_{var} is the time scale of variability and R_s is the size of the emitting region. Of all the wavelengths that are used to probe AGN, hard X-ray is very important, because firstly it is known to originate in the immediate vicinity of the central supermassive black hole (SMBH) and secondly, it is less affected by absorption. However, available studies on the hard X-ray variability characteristics of different classes of AGN on hour like timescale is very limited.

The primary X-ray emission in AGN is believed to originate in a compact region called the corona situated very close to the SMBH and the accretion disk. The knowledge of the cut-off energy (E_{cut}) of the primary X-ray continuum in AGN is very important as it carries information on the physical characteristics of the hot X-ray emitting corona. Though E_{cut} has been measured in AGN in the past, the existing measurements have large error bars largely attributed to the sensitivity of the instruments used to carry out the observations. The availability of a new hard X-ray focussing instrument Nuclear Spectroscopic Telescope Array (*NuSTAR*) which is about 100 times more sensitive than earlier hard X-ray missions has opened up the possibility to explore both the hard X-ray variability characteristics of AGN as well as to obtain precise E_{cut} values on a large sample of AGN

to infer their coronal properties. Exploiting the high sensitivity of *NuSTAR* to observations in the 3−79 keV band, we in this thesis work aimed to address two problems (a) to carry out a comparative analysis of the hard X-ray flux variability characteristics of different classes of AGN to look for similarities and/or differences in the hard X-ray variability characteristics of radio-loud vis-a-vis radio-loud AGN on hour like time scales and (b) determine new E_{cut} values for a sample of AGN to infer the coronal properties and look for correlations if any between E_{cut} and other physical properties of AGN.

The first part of the thesis objective is addressed in Chapter 3, wherein we have analysed 557 sets of observations pertaining to 335 AGN that comprises of 24 BL Lac objects, 24 flat spectrum quasars (FSRQs), 20 Narrow Line Seyfert 1 galaxies, 121 Seyfert 1 galaxies and 146 Seyfert 2 galaxies. Our analysis indicates that on hour like time scales, blazars (that includes FSRQs and BL Lac objects) are more variable that their radio-quiet counterparts namely the Seyfert galaxies, which could be attributed to the contribution of relativistic jets to the observed X-ray emission in blazars. We also found brighter AGN to be less variable as well as AGN powered by more massive black holes to be less variable.

The second part of the thesis objective is addressed in two chapters, namely Chapter 4 and Chapter 5. In Chapter 4, we report the first time measurement of E_{cut} value for the radio-loud AGN, namely 3C 120, whereas in Chapter 5, we report first time measurement of E_{cut} values for nine AGN and an upper limit of one AGN. Combining our new E_{cut} measurements with those available in literature, totalling 30 AGN, we found that the correlation between E_{cut} and the photon index of AGN is complicated, thereby requiring more E_{cut} measurements on a large number of AGN in the future to understand the complicated behaviour between E_{cut} and photon index.

Contents

List of Figures

List of Tables

Abbreviations

AGN	**A**ctive **G**alactic **N**uclei
SMBH	**S**uper **M**assive **B**lack **H**ole
NuSTAR	**N**uclear **S**pectroscopic **T**elescope **A**rray
HEASARC	**H**igh **E**nergy **A**strophysics **A**rchive **R**esearch **C**enter
*NuSTAR***DAS**	NuSTAR **D**ata **A**nalysis **S**oftware
SAA	**S**outh **A**tlantic **A**nomaly
S/N	**S**ignal to **N**oise **R**atio
BL Lac	**BL** **L**acertae
FSRQ	**F**lat **S**pectrum **R**adio **Q**uasars
NLSy 1	**N**arrow **L**ine **S**eyfert 1
$\mathbf{M}_{\odot}$	Solar **M**ass
$\mathbf{R}_{\odot}$	Solar **R**adius
CRTS	**C**atalina **R**ealtime **T**ransient **S**urvey
OVRO	**O**wens **V**alley **R**adio **O**bservatory
NASA	**N**ational **A**eronautics and **S**pace **A**dministration

Chapter 1

Introduction

Active galactic nuclei (AGN) are among the most luminous extragalactic sources present in our Universe. They are associated with the nuclei of galaxies and are known to produce very high luminosities ranging from 10^{40} to greater than 10^{47} erg/sec (Fabian 1999) from a very tiny volume. This clearly indicates that the emission from these sources are dominated by non-stellar processes. It is now believed that these sources are powered by a complex physical process, namely, the accretion of matter on to super-massive black holes (SMBHs) residing at the centres of galaxies (Rees 1984). The matter accreted by the SMBH forms an optically thick, geometrically thin accretion disk (Shakura & Sunyaev 1973), with a temperature of about 10^4-10^5 K for a SMBH of mass 10^6 to 10^9 $M_\odot$, and that emits predominantly in the optical/UV region of the electromagnetic spectrum. AGN emit over the complete accessible electromagnetic spectrum ranging from low energy radio waves to high energy $\gamma-$rays.

1.1 Phenomenology of AGN and unification scheme

Seyfert (1943) was the first to investigate AGN when he identified six spiral galaxies with unusually bright nuclei in their images and broad emission lines in their spectra. AGN are broadly classified into two categories, based on their radio emission, a majority of them ($\sim$ 85%) are called radio-quiet AGN that emit little or no radio emission and a minority of them ($\sim$15%) are called radio-loud AGN that emit more in the radio band and have large scale relativistic jets. The division of AGN into radio-loud and radio-quiet AGN is based on the radio loudness parameter (R) defined as the ratio of the flux density in the radio band at 5 GHz to the flux density in the optical B-band (R = f_{5GHz}/f_B; Urry & Padovani 1995), with radio-loud sources having R > 10 (Kellermann et al. 1989). This apparent radio-loud/radio-quiet dichotomy first seen in the Palomar-Green quasar sample by Kellermann et al. (1989) is also evident in the sample of quasars from the Sloan Digital Sky survey (SDSS; Ivezić et al. 2002), however, not seen by Cirasuolo et al. (2003) in the sample of quasars from the six degree field (6dF) quasar survey. Radio-loud and radio-quiet AGN are further sub-divided into various sub-classes such as Seyfert 1 galaxies, Seyfert 2 galaxies, blazars that includes flat spectrum radio quasars (FSRQs), BL Lacertae objects (BL Lacs) etc. Observations indicate that the appearance of a given AGN will depend strongly on the observer's location relative to the axis of symmetry of the object. The classification of AGN into different types is therefore a function of the viewing angle (θ) and this is the fundamental idea of the so called unification model of AGN (Urry & Padovani 1995). Among the different types of AGN, the classes that are analysed in this thesis are the Seyfert 1 galaxies, Seyfert 2 galaxies, narrow line Seyfert 1 (NLSy1) galaxies and blazars.

1.1.1 Seyfert 1 galaxies

Seyfert galaxies come under the radio-quiet category of AGN and they are further sub-divided into two categories namely Seyfert 1 and Seyfert 2 galaxies. Seyfert 1 galaxies have both broad and narrow emission lines in their nuclear spectra (e.g. Figure 1.1). Narrow emission lines originate from the low density ionized gas having electron density $n_e \approx 10^3$-10^6 cm^{-3} with line widths of few hundred kilometres per second whereas broad emission lines are characteristic of high density ionized gas ($n_e \geq 10^9$ cm^{-3}) with line widths of up to 10000 km s^{-1}.

1.1.2 Seyfert 2 galaxies

Seyfert 2 galaxies have only narrow emission lines in their spectra as evident in Figure 1.2. According to the unification model of AGN (Urry & Padovani 1995), Seyfert 1 and Seyfert 2 galaxies are intrinsically same and the difference between these two is due to the viewing angle with Seyfert 1 galaxies being viewed pole on and Seyfert 2 galaxies being viewed edge on.

1.1.3 Blazars

Blazars are a small subset of radio-loud AGN. They have compact radio morphology and flat radio spectra ($\alpha \leq 0.5$, $S_\nu \propto \nu^{-\alpha}$, Urry & Padovani (1995)). One of their defining characteristic is that they show rapid flux variations at all wavelengths (Wagner & Witzel 1995). They show polarised emission in the radio and optical bands. They also exhibit superluminal motion (Kellermann et al. 2003). These observed characteristics of blazars are generally attributed to their relativistic jets being aligned close to the observer. Blazars are subdivided into FSRQs

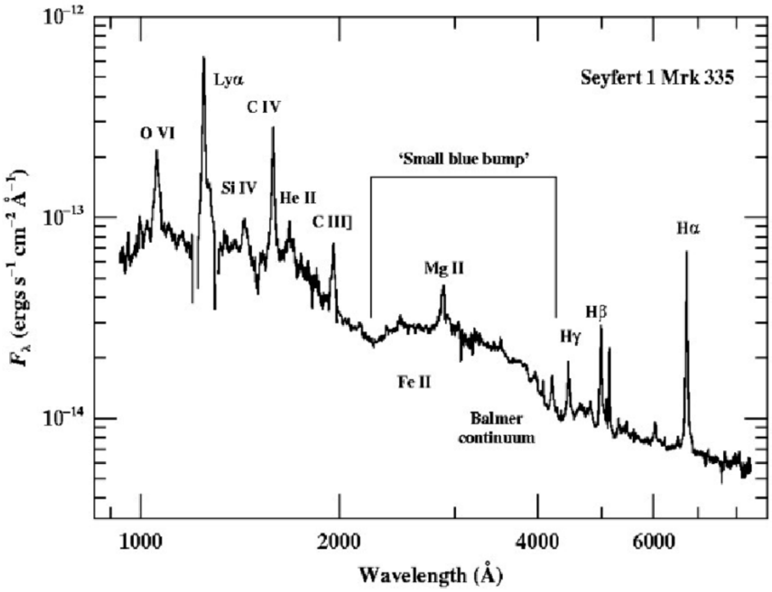

FIGURE 1.1: Optical spectrum of the Seyfert 1 galaxy Mrk 335 (Mickaelian 2015).

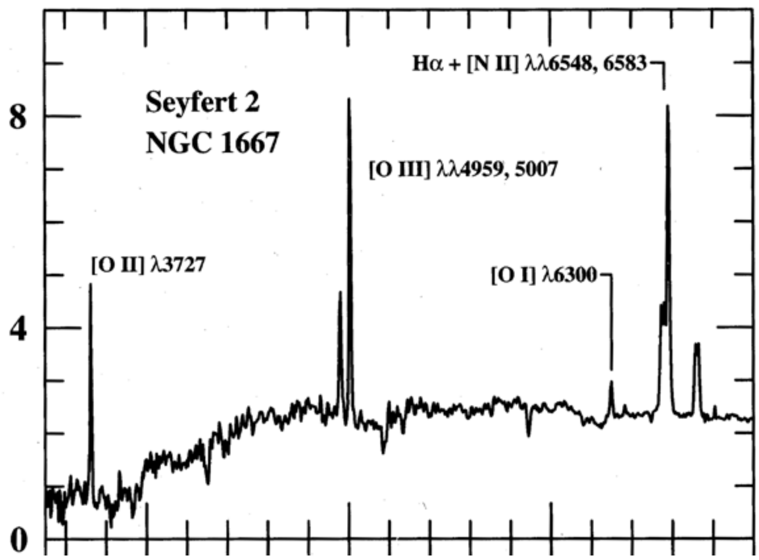

FIGURE 1.2: Optical spectrum of the Seyfert 2 galaxy NGC 1667 (Ho et al. 1993). The X-axis is in wavelength (Å), while the Y-axis is in F_λ (ergs s^{-1} cm^{-2} Å^{-1}).

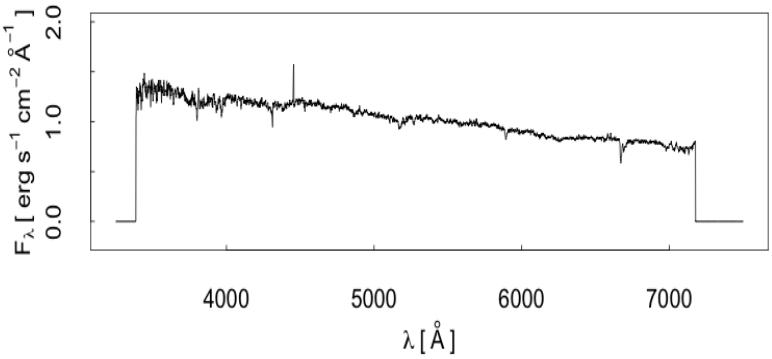

FIGURE 1.3: Optical spectrum of the BL Lac object Mrk 421 (Credit: `http://ned.ipac.caltech.edu/classic/`).

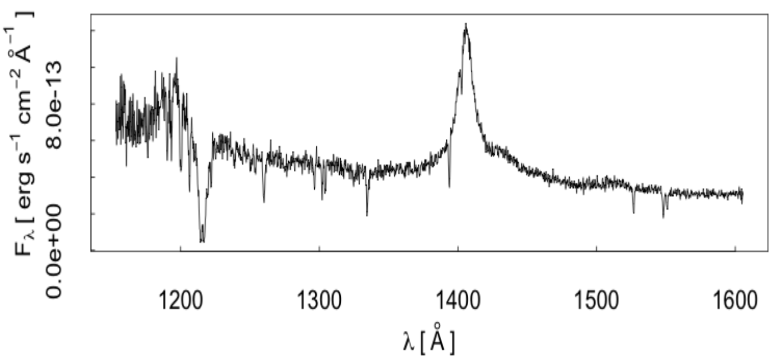

FIGURE 1.4: Optical spectrum of the FSRQ object 3C 273 (Credit: `http://ned.ipac.caltech.edu/classic/`).

and BL Lacs. FSRQs have broad emission lines in their optical spectrum (Figure 1.4) while BL Lacs either have a featureless optical spectrum or an optical spectrum (Figure 1.3) with weak emission lines (with equivalent width (EW) < 5 Å). The presence and absence/weak of emission lines in FSRQs and BL Lacs could be linked to accretion processes with FSRQs having radiatively efficient accretion disk and BL Lacs having inefficient accretion disk (Maraschi & Tavecchio 2003).

1.1.4 Narrow line Seyfert 1 galaxies(NLSy1)

NLSy1 galaxies were identified as a separate class of AGN by Osterbrock & Pogge (1985). They are characterized by narrow Balmer lines with FWHM $\leq$ 2000 km s^{-1}, weak [OIII] lines with O[III]/H$\beta < 3$ and strong optical Fe II lines (Osterbrock & Pogge 1985; Goodrich 1989). They have steep soft X-ray spectra and show rapid X-ray variability (Boller et al. 1996). These observed characteristics are attributed to them having low mass black holes $10^6$$-$$10^8$ M$_\odot$ and hosted by spiral galaxies (Kotilainen et al. 2016). NLSy1 galaxies came into prominence about a decade ago due to the detection of γ-rays in few sources by the *Fermi* γ-ray space telescope. As of now less than 2 dozen NLSy1 galaxies are known to be emitters of γ-rays, and the detection of γ-rays unambiguously points to the presence of relativistic jets in them. Multi-wavelength analysis of γ-ray emitting NLSy1 galaxies indicate that they are the low black hole mass counterparts to conventional FSRQs (Paliya et al. 2016).

1.2 Variability in AGN

One of the defining characteristics of AGN is that they show flux variations over the entire electromagnetic spectrum (Wagner & Witzel 1995; Ulrich et al. 1997) and the timescales for these flux variations can be as long as years and as short as minutes (Smith 1996). This flux variability behaviour in AGN was realised soon after the discovery of quasars (Matthews & Sandage 1963; Fitch et al. 1967) and since then, AGN have been studied for flux variations in different wavelengths and timescales ranging from minutes to years. However, we still do not have a clear understanding of the physical processes causing flux variations in different categories of AGN. In spite of that, studying AGN flux variability on short time scales, say minutes to hours is very important as it will help to probe the innermost regions of AGN not accessible by any direct imaging techniques till now via $R_s < c\ t_{var}$, where t_{var} is the variability time scale and R_s is the size of the emission region.

1.2.1 Hard X-ray variability

Though studies of flux variation in AGN serve as an effective way to probe the very central region of AGN, among different wavelength probes, hard X-ray is most suited as (i) it is known to originate in the immediate vicinity of the SMBH and (ii) it is less affected by absorption. Different processes contribute to the hard X-ray emission in radio-quiet and radio-loud AGN. In the case of radio-quiet AGN, the hard X-ray emission is due to the Comptonization of accretion disk photons by the hot corona (Haardt & Maraschi 1993). It has been observed that radio-loud AGN with optical luminosities similar to radio-quiet AGN show enhanced X-ray emission that could be linked to the jets in them (Zamorani et al. 1981; Wilkes & Elvis 1987; Cappi et al. 1997). Thus, in radio-loud AGN, in addition to the hard X-ray coronal emission, they also have hard X-ray emission through inverse Compton (IC) emission processes from relativistic jet electrons as well as synchrotron jet emission (Soldi et al. 2014). Carrying out a comparative analysis of the hard X-ray flux variability characteristics of different classes of AGN, in addition to providing clues on the processes that cause flux variations, can also test the AGN unification model. There are various studies available in the literature on the long term X-ray variability at energies less than 10 keV based on observations from the *Rossi X-ray Timing Explorer* (RXTE) and XMM-Newton (Nandra et al. 1997; Fiore et al. 1998; Turner et al. 1999; Uttley et al. 2002; Markowitz et al. 2003; Soldi et al. 2008; McHardy 2010).

1.2.2 Hard X-ray variability: Pre-NuSTAR era

Our knowledge on the hard X-ray flux variability characteristics of AGN is very limited which is based on observations from BeppoSAX (Petrucci et al. 2000), INTEGRAL (Petrucci et al. 2013) and Suzaku (Reis et al. 2012). Using the Burst Alert Telescope (BAT) on board *Swift*, hard X-ray flux variability characteristics have been studied for few AGN, but they are limited to long time scales of the order of days to years (Soldi et al. 2014).

1.2.3 Hard X-ray variability: NuSTAR era

Only few studies are available on the hard X-ray variability of AGN on hour like time scales using *NuSTAR* (Paliya et al. 2015; Ravasio et al. 2003; Tagliaferri et al. 2000). These studies do indicate that hard X-ray variability on hour like time scales is prevalent in AGN.

1.3 Corona in AGN

The observed primary X-ray continuum emission from AGN is thought to be due to the inverse Compton scattering of UV and optical photons from the accretion disk by hot electrons in a compact region called the corona (Haardt & Maraschi 1991; Haardt et al. 1994, 1997). This inverse Compton scattering of UV/optical photons from the accretion disk by the coronal electrons produces a X-ray continuum with a power-law spectral shape and a high energy cut-off (Rybicki & Lightman 1979). This high energy cut-off (E_{cut}) in the observed spectrum happens when the electrons in the corona are no longer able to add energy to the photon in the photon-electron interaction (Buisson et al. 2018). The shape of the power law continuum depends on various parameters such as the seed photon field, the coronal temperature (K_BT_e), the optical depth and the observers viewing angle, while the value of E_{cut} is determined by K_BT_e (Mushotzky et al. 1993). X-ray reverberation studies indicate the AGN corona to be located close to the accretion disk (Fabian et al. 2009; Kara et al. 2013) typically within $3 - 10$ R_G, where, R_G is the gravitational radius defined as $R_G = GM_{BH}/c^2$, and M_{BH} is the mass of the SMBH. Rapid X-ray flux variability studies (McHardy et al. 2005), the observed small time scales of X-ray eclipses (Risaliti et al. 2005, 2011) and micro-lensing studies (Chartas et al. 2009) point to the small size of the X-ray corona of $5-10$ R_G. Exchange of energy happens between particles and photons in the compact corona, the compactness of which is parameterised by the dimensionless compactness parameter (Guilbert et al. 1983).

$$l = 4\pi \frac{m_p}{m_e} \frac{R_G}{R} \frac{L}{L_E} \tag{1.1}$$

where m_p and m_e are the masses of the proton and electron respectively, R_G is the gravitational radius, R is the size of the source, L is the luminosity of the source, and L_E is the Eddington luminosity defined as $L_{Edd} = \frac{4\pi GM_{BH}m_pc}{\sigma_T} \sim 1.3 \times 10^{38}(\frac{M_{BH}}{M_\odot})$ erg s^{-1}, where σ_T is the Thomson scattering cross section. Also, the coronal electron temperature can be characterised by the dimensionless parameter as

$$\theta = K_BT_e/m_ec^2. \tag{1.2}$$

Empirically, the electron temperature and E_{cut} are related as $E_{cut} = 2 - 3K_BT_e$ (Petrucci et al. 2001). In spite of several studies, the geometry of the corona is still not known. It could be in the form of a slab (Poutanen et al. 1997) or a sphere (Dove et al. 1997). Also, it is not known if the medium of the coronal plasma is continuous or patchy (Stern et al. 1995; Petrucci et al. 2013). In addition to the big blue bump (BBB) and the primary power law X-ray continuum with a high energy cut off, a large fraction of AGN also show soft excess between $0.1 - 2$ keV, broad ($\sim 4 - 7$ keV) Fe Kα line and a Compton reflection bump peaking between

$20 - 30$ keV. These features are well explained by reflection models (Fabian et al. 2002) where the coronal photons irradiate the accretion disk and Compton scatter off the disk. Determination of E_{cut} values from the X-ray spectra of AGN can provide important constraints on the temperature of the corona $K_B T_e$.

1.3.1 Cut-off energy in AGN: Pre-NuSTAR era

E_{cut} measurements are difficult to obtain due to the requirement of X-ray data with high S/N beyond 10 keV. In spite of that, E_{cut} measurements for few nearby AGN are available via analysis of data from the *Compton Gamma Ray Observatory* (CGRO; Zdziarski et al. 2000, 1996; Johnson et al. 1997), BeppoSAX (Nicastro et al. 2000; Dadina 2007), *INTEGRAL* (Malizia et al. 2014; Lubiński et al. 2010, 2016; Ricci et al. 2011), Swift/BAT (Vasudevan et al. 2013a; Ricci et al. 2017) and Suzaku (Tazaki et al. 2011).

1.3.2 Cut-off energy in AGN: NuSTAR era

The launch of the *Nuclear Spectroscopic Telescope Array* (NuSTAR; Harrison et al. 2013) with its unique capability to focus hard X-rays and thereby providing good signal to noise ratio data in the $3-79$ keV band has allowed us to get improved values of E_{cut} measurements for a growing number of AGN. As of today E_{cut} has been measured in less than two dozen AGN using *NuSTAR* (Brenneman et al. 2014; Baloković et al. 2015; Ballantyne et al. 2014; Matt et al. 2015; Ursini et al. 2015; Lohfink et al. 2015; Tortosa et al. 2016; Lanzuisi et al. 2016; Lohfink et al. 2017; Kara et al. 2017; Tortosa et al. 2018a; Porquet et al. 2018; Buisson et al. 2018; Rani & Stalin 2018a,b). With the availability of more spectral measurements from *NuSTAR*, correlations between E_{cut} and various physical properties of the sources have been explored. From an analysis of 12 sources observed with *NuSTAR*, Rani & Stalin (2018b), found no correlation of E_{cut} with M_{BH} and Γ. Also, Tortosa et al. (2018b) using 19 sources from *NuSTAR*, found no correlation between E_{cut} and M_{BH}. The number of E_{cut} measurements from *NuSTAR* is small to unambiguously know for the existence of correlation of E_{cut} with various physical properties of AGN. It is therefore very important to determine E_{cut} for more number of AGN. Recently, using Swift/BAT data for a sample of about 200 AGN, Ricci et al. (2018) found a statistically significant negative correlation between E_{cut} and Eddington ratio. However, observations from Swift/BAT are likely to be background dominated due to its survey mode of operation necessitating more E_{cut} measurements from *NuSTAR* to confirm the correlation noticed by Ricci et al. (2018).

1.4 Major goals of the thesis

From the overview of the hard X-ray spectral and timing properties of AGN outlined in this chapter, it is very clear that many questions on the hard X-ray flux variability as well as the coronal properties of AGN need to be settled. Progress in this direction only rests on carrying out (a) systematic flux variability analysis of different types of AGN in the hard X-ray band and (b) spectral analysis of a large number of Seyfert galaxies to deduce information on the cut-off energies in AGN which could in principle lead to information on the nature of the X-ray corona in them. Therefore, the key questions that we aimed to address in this thesis work are given below

1. How do radio-loud AGN (blazars) compare with radio-quiet AGN (Seyfert 1 galaxies, Seyfert 2 galaxies and radio-quiet NLSy1 galaxies) in their hard X-ray variability characteristics on hour like timescales? Can any observed

differences in the hard X-ray variability if any be attributed to differences in the hard X-ray emission processes in them?

2. What is the dependence of hard X-ray flux variability on various physical characteristics of AGN?

3. Whether the quality of hard X-ray data available from *NuSTAR* is sufficient enough to increase the E_{cut} measurements on more number of AGN.

4. Is there any relation between E_{cut} and various physical properties of AGN?

These above problems will be addressed in this thesis.

Chapter 2

Observations, sample selection and basic data reduction

Limited results are available in literature on the hard X-ray variability characteristics of AGN on hour like timescales. This is attributed to the non-availability of sensitive hard X-ray instruments. The availability of sensitive focussing hard X-ray telescope *NuSTAR* has made open the possibility of studying the hard X-ray flux variability characteristics of AGN on hour like timescales. Therefore an effort is made in this thesis to carry out a systematic study of the flux variability characteristics of a large sample of radio-loud and radio-quiet AGN to have an understanding of the hard X-ray flux variability characteristics of radio-loud vis-a-vis radio-quiet AGN. Similarly observations with *NuSTAR* has enabled accumulation of high S/N data on a large number of AGN, which is crucial to find E_{cut} values in AGN. Therefore a strong need is felt to carry out a systematic analysis of the spectra of a large sample of AGN to find E_{cut} values.

2.1 Nuclear Spectroscopic Telescope Array (*NuSTAR*)

The data used in this thesis work is from *NuSTAR*. This is the first focussing hard X-ray instrument with sensitivity more than 100 times than earlier missions operating in the same energy range same as *NuSTAR* (see Table 2.1). *NuSTAR* (Harrison et al. 2013) is a space based hard X-ray mission, it was launched into a low-Earth equatorial orbit on 13th June, 2012 at an altitude and an inclination of nearly 600 km and 6 degrees respectively. It is the first hard X-ray focusing telescopes which operates in the high energy X-ray (3−79) keV band.
NuSTAR (Figure 2.1) uses a Wolter-I design with conical approximation to focus hard X-rays which comprises of 133 concentric mirror shells covered with Pt/SiC and W/Si multilayer, this coating helps instrument to achieve reflectivity up to 79 keV. *NuSTAR* has two focal plane modules or detector units which are called as focal plane module A (FPMA) and B (FPMB) respectively (Figure 2.1). Each focal plane module has a total field of view of $\sim 13'$. NuSTAR has better angular resolution, sensitivity and collecting area than any existing hard X-ray instrument, (see Table 2.1, Figure 2.2). Multilayer coatings and low grazing angle X-ray optics help NuSTAR to achieve collecting area of $\approx$79 keV. The summary of all the parameters of *NuSTAR* is given in Table 2.2.

2.2 Sample

Sample selection is very crucial for a comparative analysis of the hard X-ray flux variability of radio-loud and radio-quiet AGN as well as to measure E_{cut} values.

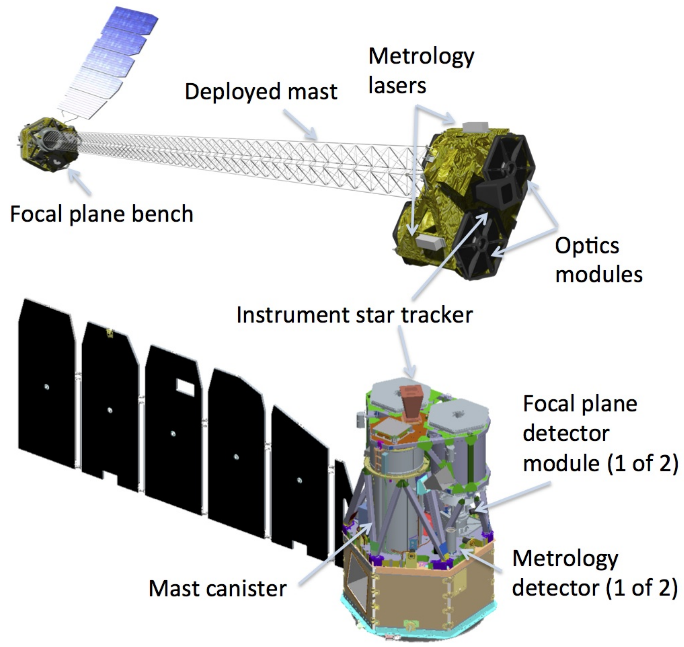

FIGURE 2.1: The schematic of NuSTAR. (Harrison et al. 2013)

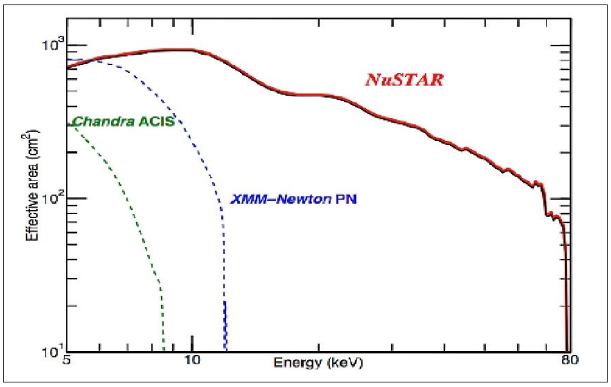

FIGURE 2.2: A comparison of the effective area curves of Chandra, XMM-Netwon and NuSTAR. Credit: `https://heasarc.gsfc.nasa.gov/docs/nustar/nustar_tech_desc.html`

TABLE 2.1: Some details of the currently operational hard X-ray instruments.

Name	Energy range	Launch year	Sensitivity	Ref.
Integral (IBIS/ISGRI)	15−1000 keV	2002	∼500μcrab (>Ms exposures)	a
Swift/BAT	15−150 keV	2002	∼800μcrab (>Ms exposures)	b
Suzaku/HXD	10−600 keV	2005	–	c
NuSTAR	3−79 keV	2012	∼0.7μcrab (1 Ms exposures)	d

a: Ubertini et al. (2003); b: Barthelmy et al. (2005), c: Takahashi et al. (2007); d: Harrison et al. (2013)

TABLE 2.2: Parameters of *NuSTAR*.

Parameter(Name)	Value
Energy range	3−79 keV
Angular resolution (HPD)	58 ″
Angular resolution (FWHM)	18 ″
Energy resolution (FWHM)	400 eV at 10 keV, 900 eV at 68 keV
Temporal resolution	2 μs
Sensitivity (6−10 keV)	2×10^{-15} erg cm^{-2} s^{-1}
Sensitivity (10−30 keV)	1×10^{-14} erg cm^{-2} s^{-1}
Background (10−30 keV)(HPD)	1.1×10^{-3} counts s^{-1}
Background (30−60 keV)(HPD)	8.4×10^{-4} counts s^{-1}

However the sample for the study in this thesis is limited by the availability of *NuSTAR* data in the public domain.

2.2.1 Timing

For flux variability studies, we used all the data of AGN from *NuSTAR* that have become public from its launch in 13 June 2012 till June 2018. This search lead us to an initial sample of about six hundred sources. On this initial list, we did the following

1. Firstly, we cross-correlated our sample with the catalog of sources in Véron-Cetty & Véron (2010). Only sources that have a definite classification in Véron-Cetty & Véron (2010) catalog were considered. In Véron-Cetty & Véron (2010), Seyfert galaxies are classified into various categories such as Sy1, Sy1.2, Sy1.5, Sy1.8 etc. All Seyfert galaxies with sub-classes up to Sy1.5 were considered under the Seyfert 1 galaxies category and sources with sub-classes beyond Sy1.5 were considered in the category of Seyfert 2 galaxies Also, sources with Sy1h classification were considered under the Seyfert 2 galaxies category.

2. Secondly, for sources that do not have an entry in Véron-Cetty & Véron (2010), we searched the BZCAT* catalog (Massaro et al. 2009) and the 105 month *Swift*-BAT† catalog (Oh et al. 2018).

Adopting the above two criteria, we arrived at a final sample of 335 sources that consists of 24 BL Lacs 24 FSRQs, 20 NLSy1 galaxies, 121 Seyfert 1 galaxies and 146 Seyfert 2 galaxies. Tables 2.3, 2.4, 2.5 and 2.6 give the details of the sources used for flux variability analysis on hour like timescales.

*https://www.ssdc.asi.it/bzcat/

†https://swift.gsfc.nasa.gov/results/bs105mon/

TABLE 2.3: Details of the sources analysed for flux variability in this work. The columns are (1) and (7): name of the source, (2) and (8) right ascension, (3) and (9) declination (4) and (10) V band magnitude, here * refers to photographic magnitude, # refers to R-band magnitude from Véron-Cetty & Véron (2010) and $ refers to R-band magnitude from BZCAT, (5) and (11) redshift, (6) and (12) type of the source.

Name	α(2000)	δ(2000)	V	z	Type	Name	α(2000)	δ(2000)	V	z	Type
(1)	(2)	(3)	(4)	(5)	(6)	(7)	(8)	(9)	(10)	(11)	(12)
Fairall 1203	00 01 46.0	−76 57 14	—	0.06	Sy2	2MASX J03181899+6829322	03 18 19.4	+68 29 31	—	0.09	Sy2
Mkn 335	00 06 19.5	+20 12 11	13.85	0.03	Sy1	NGC 1275	03 19 48.2	+41 30 42	12.48	0.02	Sy1
S5 0014+81	00 17 08.5	+81 35 08	15.90$	3.39	FSRQ	1H 0323+342	03 24 41.2	+34 10 45	15.72	0.061	NLSy1
2MASX J00341665-7905204	00 34 16.7	−79 05 21	15.40	0.07	Sy1	NGC 1320	03 24 48.7	−03 02 32	14.00	0.009	Sy2
Mrk 348	00 48 47.2	+31 57 25.0	14.59	0.014	Sy2	LCRS B032315d2-420449	03 25 02.1	−41 54 19	15.43	0.06	Sy1
Mrk 1148	00 51 54.8	+17 25 59	15.96	0.06	Sy1	IRAS 03219+4031	03 25 17.6	+40 42 00	15.20	0.05	Sy2
Ton S180	00 57 20.2	−22 22 56	14.4	0.06	NLSy1	NGC 1365	03 33 36.4	−36 08 24	12.95	0.006	Sy2
ESO195 IG021 NED03	01 00 36.5	−47 52 03	16.70	0.05	Sy2	1ES 0347-121	03 49 23.2	−11 59 27	19.10	0.19	BL Lac
NGC 424	01 11 27.7	−38 05 10	14.12	0.011	Sy2	PKS 0352-686	03 52 57.6	−68 31 17	13.60	0.09	BL Lac
NGC 454E	01 14 23.1	−55 23 51	13.58	0.01	Sy2	SWIFT J0357d5-6255	03 56 20.0	−62 51 39	—	0.11	Sy2
MCG+08-03-018	01 22 34.4	+50 03 18	—	0.02	Sy2	MRSS302-039347	03 56 56.5	−40 41 46	—	0.08	Sy2
Fairall 9	01 23 45.8	−58 48 21	13.83	0.05	Sy1	3C 098	03 58 54.5	+10 26 02	15.41	0.03	Sy2
BZB J0123-2310	01 23 38.3	−23 10 59	17.60$	0.40	BL Lac	4C+50.11	03 59 29.7	+50 57 50	18.10$	1.52	BL Lac
NGC 513	01 24 26.8	+33 47 58	13.40	0.019	Sy2	PKS 0402-362	04 03 53.8	−36 05 01	17.17	1.42	FSRQ
4C 25.05	01 26 42.8	+25 59 01	17.50	2.37	FSRQ	3C 105	04 07 16.4	+03 42 25	18.50	0.09	Sy2
MCG-03-04-072	01 28 06.7	−18 48 31	15.70	0.05	Sy1	1ES 0414+009	04 16 52.4	+01 05 24	16.30	0.29	BL Lac
NGC 612	01 33 57.8	−36 29 36	13.20	0.030	Sy2	1H 0419-577	04 26 00.8	−57 12 01	13.20*	0.1	Sy1
2MASX J01402676-5319389	01 40 26.8	−53 19 39	—	0.07	Sy2	3C 120	04 33 11.1	+05 21 15	15.05	0.033	Sy1
MCG +01−05−047	01 52 49.0	−03 26 49	14.24	0.017	Sy2	2MASX J04372814-4711298	04 37 28.1	−47 11 29	15.30	0.05	Sy1
1ES0152+022	01 55 25.0	+02 28 15	17.70	0.08	Sy1	IRAS 04392-2713	04 41 22.6	−27 08 20	15.32	0.08	Sy1
NGC 788	02 01 06.5	−06 48 56	12.76	0.013	Sy2	MCG +03−13−01	04 46 29.7	+18 27 40	15.00	0.016	Sy2
Mrk 1018	02 06 16.0	−00 17 28	15.50	0.04	Sy2	PKS 0451-28	04 53 14.6	−28 07 37	18.20*	2.56	FSRQ
ESO 197-27	02 10 53.3	−49 41 45	14.80	0.05	Sy2	2MASX J04532576+0403416	04 53 25.7	+04 03 42	15.00	0.03	Sy2
2MASX J02141794+5144520	02 14 10.4	+51 43 08	16.50	0.05	BL Lac	ESO033 G002	04 55 58.8	−75 32 28	14.60	0.02	Sy2
RBS 0295	02 14 37.3	−64 30 04	15.90	0.07	Sy1	2MASX J05043414-7349269	05 04 34.2	−73 49 27	—	0.05	Sy2
Mrk 590	02 14 33.6	−00 46 00	13.81	0.03	Sy1	XSS J05054−2348	05 05 45.7	−23 51 14	17.00	0.035	Sy2
HB89 0212+735	02 17 30.9	+73 49 33	20.00	2.37	FSRQ	1ES 0502+675	05 07 56.1	+67 37 24	18.50	0.42	BL Lac
VZw 232	02 23 33.9	+45 49 07	—	0.06	Sy2	2MASX J05081967+1721483	05 08 19.7	+17 21 47	13.50	0.02	Sy2
B 0222+185	02 25 04.7	+18 46 49	19.10	2.69	FSRQ	Ark 120	05 16 11.4	−00 09 00	13.92	0.03	Sy1
AM 0224-283	02 26 25.7	−28 20 59	16.76	0.06	Sy1	SWIFT J0516.5-5179	05 16 38.0	−51 46 50	18.00	0.22	Sy1
Mrk 1040	02 28 14.4	+31 18 41.0	14.74	0.016	Sy1	ESO 362−G18	05 19 35.8	-32 39 27.0	13.37	0.013	Sy1
Mrk 1044	02 30 05.5	−08 59 53	14.29	0.02	NLSy1	Pictor A	05 19 49.6	−45 46 44	15.77	0.04	Sy2
1ES 0229+200	02 32 48.6	+20 17 17	18.00	0.14	BL Lac	IRAS F05189-2524	05 21 01.4	−25 21 45	14.75	0.04	Sy2
NGC 985	02 34 37.8	−08 47 15	14.28	0.043	Sy1	PMN J0525-2338	05 25 06.5	−23 38 10	17.74#	3.1	FSRQ
ESO416 G002	02 35 13.4	−29 36 17	14.90	0.06	Sy2	ESO253 3	05 25 18.4	−46 00 18	14.20	0.04	Sy2
Mrk 595	02 41 34.9	+07 11 14	14.69	0.03	Sy1	1RXS J054357d3-553206	05 43 57.3	−55 32 08	17.40	0.27	BL Lac
NGC 1068	02 42 40.7	−00 00 47	10.83	0.004	Sy2	NGC 2110	05 52 11.4	−07 27 23	13.51	0.007	Sy2
2MFGC02171	02 44 03.0	+53 28 28	—	0.04	Sy2	MCG+8-11-11	05 54 53.6	+46 26 21	14.62	0.02	Sy1
HB89 0241+622	02 44 57.6	+62 28 06	12.19	0.04	Sy1	B3 0552+398	05 55 30.8	+39 48 49	18.30#	2.36	FSRQ
NGC 1194	03 03 49.2	−01 06 15	14.18	0.01	Sy2	PKS 0558-504	05 59 47.4	−50 26 51	14.97	0.14	NLSy1
ESO 031-G008	03 07 35.0	−72 50 04	14.98	0.03	Sy1	IRAS 05581+0006	06 00 40.1	+00 06 18	17.60#	0.12	Sy1
NGC 1229	03 08 10.8	−22 57 39	14.45	0.04	Sy2	Mrk 3	06 15 36.3	+71 02 15	13.34	0.01	Sy2
HB89 0312-770	03 11 55.3	−76 51 51	15.40$	0.22	FSRQ	2MASX J06230765-6436211	06 23 07.7	−64 36 19	13.70$	0.13	FSRQ
MCG+00-09-042	03 17 02.2	+01 15 18	—	0.02	Sy2	ESO121 IG028	06 23 46.0	−60 58 36	15.20	0.04	Sy2

TABLE 2.4: Details of the sources analysed for flux variability in this work. Columns have the same meaning as in Table 2.3

Name	α(2000)	δ(2000)	V	z	Ty pe	Name	α(2000)	δ(2000)	V	z	Type
2MASX J06403799-4321211	06 40 38.0	−43 21 21	—	0.06	Sy2	SDSS J104326.47+110524.2	10 43 26.5	+11 05 23	17.01	0.05	Sy1
NGC 2273	06 50 08.7	+60 50 45	13.54	0.01	Sy2	S5 1039+81	10 44 23.1	+80 54 39	17.90*	1.26	FSRQ
Mkn 6	06 52 12.4	+74 25 38	14.19	0.02	Sy1	MCG+12 10 067	10 44 08.4	+70 24 19	14.20	0.03	Sy2
1H 0707−495	07 08 41.5	−49 33 06	15.70	0.041	NLSy1	MCG+06-24-008	10 44 49.0	+38 10 52	—	0.03	Sy2
2MASX J07084326-4642494	07 08 43.2	−46 42 49	—	0.05	Sy2	NGC 3393	10 48 23.4	−25 09 44	13.95	0.01	Sy2
RGB J0710+591	07 10 30.1	+59 08 21	18.40	0.13	BL Lac	Mrk 417	10 49 30.9	+22 57 52	16.00	0.03	Sy2
Mrk 376	07 14 15.1	+45 41 57	14.62	0.06	Sy1	2MASX J10523297+1036205	10 52 33.0	+10 36 20	18.61	0.09	Sy1
ESO428 G014	07 16 31.2	−29 19 28	13.52	0.01	Sy2	Mrk 728	11 01 01.8	+11 02 50	16.93	0.036	Sy2
S5 0716+714	07 21 53.3	+71 20 36	15.50	0.3	BL Lac	1ES 1101-232	11 03 37.7	−23 29 31	16.55	0.19	BL Lac
IRAS 07245−3548	07 26 26.3	−35 54 22	16.80	0.029	Sy2	PG 1100+772	11 04 13.8	+76 58 58	15.72	0.31	Sy1
1RXS J073308.7+455511	07 33 09.2	+45 55 05	16.01	0.14	Sy1	Mrk 421	11 04 27.2	+38 12 32	12.90	0.03	BL Lac
Mrk 9	07 36 57.0	+58 46 13	14.37	0.039	Sy1	NGC 3516	11 06 47.4	+72 34 07	12.40	0.009	Sy1
IRAS 07378−3136	07 39 44.7	−31 43 02	16.80*	0.025	Sy2	ESO438-G009	11 10 48.0	−28 30 04	14.17	0.02	Sy1
3C 184.1	07 43 01.4	+80 26 26	17.00	0.12	Sy1	Mrk 732	11 13 49.8	+09 35 10	14.17	0.030	Sy1
UGC 03995A	07 44 09.1	+29 14 49	13.33	0.02	Sy2	MCG+13-08-056	11 14 43.9	+79 43 36	—	0.04	Sy2
SDSS J0758+3923	07 58 21.0	+39 23 36	18.49	0.22	Sy2	IRAS F11119+3257	11 14 38.9	+32 41 33	17.96	0.19	NLSy1
Mrk 1210	08 04 05.9	+05 06 50	13.70	0.013	Sy2	QSO B1114-2846	11 17 04.0	−29 02 29	15.81*	0.07	NLSy1
MCG+02 21 013	08 04 46.4	+10 46 34	14.50	0.04	Sy1	RBS 0970	11 20 48.1	+42 12 13	17.11	0.12	BL Lac
PG 0804+761	08 10 58.5	+76 02 43	14.71	0.10	Sy1	ESO439 G009	11 27 23.4	−29 15 27	14.80	0.02	Sy2
FAIRALL 0272	08 23 01.1	−04 56 05	16.00	0.021	Sy2	Mrk 739E	11 36 29.3	+21 35 45	14.08	0.03	NLSy1
F2M 0830+3759	08 30 11.2	+37 59 51	20.07	0.41	Sy1	IGR J11366-6002	11 36 42.1	−60 03 07	—	0.01	Sy2
FAIRALL 1146	08 38 30.8	−35 59 33	16.10	0.031	Sy1	NGC 3783	11 39 01.8	-37 44 19.0	13.43	0.009	Sy1
3C 206	08 39 50.6	−12 14 34	15.76	0.20	Sy1	SBS 1136+594	11 39 09.0	+59 11 55	15.77	0.06	Sy1
HB 0836+710	08 41 24.4	+70 53 42	17.30*	2.22	FSRQ	NGC 3822	11 42 11.3	+10 16 40	13.70	0.02	Sy2
2MASX J08434495+3549421	08 43 45.0	+35 49 42	17.55	0.05	Sy2	UGC 06728	11 45 16.1	+79 40 54	15.88	0.01	Sy1
SWIFT J0845.0−3531	08 45 21.4	−35 30 24	—	0.137	Sy1	2MASX J11462959+7421289	11 46 29.6	+74 21 28	16.60	0.06	Sy2
PMN J0847-2337	08 47 01.56	−23 37 02	13.00$	0.06	BL Lac	SDSS J114921.52+532013.4	11 49 21.6	+53 20 13	18.15	0.10	Sy1
OJ 287	08 54 48.8	+20 06 30	15.4$	0.31	BL Lac	RBS 1037	11 49 18.6	−04 16 52	17.40	0.09	Sy1
MCG+11 11 032	08 55 12.5	+64 23 46	—	0.04	Sy2	MCG 01 30 041	11 52 37.9	−05 12 26	15.00	0.02	Sy2
NGC 2712	08 59 30.5	+44 54 50	—	0.01	Sy2	NGC 3998	11 57 56.1	+55 27 13	12.10	0.004	Sy2
2MASX J09112999+4528060	09 11 30.0	+45 28 06	—	0.03	Sy2	IC 751	11 58 52.5	+42 34 15	14.39	0.03	Sy2
Mrk 704	09 18 26.0	+16 18 20	14.20	0.03	Sy1	Mrk 1310	12 01 14.5	−03 40 40	15.89	0.02	Sy1
IC 2461	09 19 58.0	+37 11 29	—	0.01	Sy2	NGC 4051	12 03 09.6	+44 31 53	12.92	0.002	NLSy1
MCG +01−24−012	09 20 46.2	−08 03 21	13.70	0.020	Sy2	B2 1204+34	12 07 32.9	+33 52 40	—	0.08	Sy2
MCG +04−22−042	09 23 43.1	+22 54 33	14.80	0.033	NLSy1	NGC 4151	12 10 32.5	+39 24 21	11.85	0.003	Sy1
2MASX J09235371-3141305	09 23 53.7	−31 41 31	15.00#	0.04	Sy2	PG 1211+143	12 14 17.7	+14 03 13	14.19	0.08	NLSy1
Mrk 110	09 25 12.9	+52 17 11	16.41	0.04	Sy1	WAS 49b	12 14 17.8	+29 31 43	15.40	0.064	Sy2
SWIFT J0926.1+6931	09 25 47.6	+69 27 54	—	0.04	Sy2	ESO505 30	12 17 00.0	−26 12 36	15.49	0.04	Sy2
2MASX J09261742-8421330	09 26 18.0	−84 21 37	15.60	0.06	Sy2	Mrk 766	12 18 26.5	+29 48 47	13.57	0.01	NLSy1
NGC 2992	09 45 42.0	-14 19 35.0	13.78	0.008	Sy2	NGC 4258	12 18 57.5	+47 18 14	11.65	0.002	Sy2
MCG-5-23-16	09 47 40.2	−30 56 54	13.69	0.01	Sy1	PKS J1220+0203	12 20 11.9	+02 03 42	15.97	0.24	Sy1
3C 227	09 47 45.1	+07 25 20	16.97	0.086	Sy1	1ES 1218p+04	12 21 21.9	+30 10 37	15.85	0.18	BL Lac
PMN J0948+0022	09 48 47.3	+00 22 26	—	0.59	NLSy1	Mrk 205	12 21 44.1	+75 18 38	15.24	0.07	Sy1
NGC 3079	10 01 58.5	+55 40 50	12.18	0.004	Sy2	NGC 4388	12 25 46.7	+12 39 41	13.90	0.01	Sy2
SWIFT J1009.3-4250	10 09 48.2	−42 48 40	14.95	0.03	Sy2	NGC 4395	12 25 48.9	+33 32 48	10.27	0.001	Sy2
NGC 3147	10 16 53.2	+73 24 02	12.65	0.01	Sy2	3C 273	12 29 06.7	+02 03 08	12.85	0.16	FSRQ
Ark 241	10 21 40.2	−03 27 14	15.70	0.04	Sy1	2MASX J12313717-4758019	12 31 37.2	−47 58 03	16.50	0.03	Sy1
NGC 3227	10 23 30.6	+19 51 56	11.79	0.004	Sy1	RBS 1125	12 32 03.7	+20 09 29	15.30	0.06	Sy1
ESO500 34	10 24 31.5	−23 33 10	14.21	0.01	Sy2	NGC 4507	12 35 36.5	−39 54 33	13.54	0.01	Sy2
NGC 3281	10 31 52.1	−34 51 13	14.02	0.01	Sy2	NGC 4579	12 37 43.5	+11 49 05	11.72	0.01	Sy2

Table 2.5: Details of the sources analysed for flux variability in this work. Columns have the same meaning as in Table 2.3

Name	α(2000)	δ(2000)	V	z	Ty pe	Name	α(2000)	δ(2000)	V	z	Type
IGR J12391-1612	12 39 06.3	−16 10 48	14.80	0.04	Sy2	PKS 1549-79	15 56 58.5	−79 14 05	18.50	0.15	Sy1
NGC 4593	12 39 39.4	−05 20 39	13.15	0.01	Sy1	UGC 10120	15 59 09.6	+35 01 47	15.06	0.03	NLSy1
WKK 1263	12 41 25.5	−57 49 51	16.90	0.02	Sy2	LEDA 100168	16 07 23.8	+85 01 51	17.40	0.18	Sy1
NGC 4785	12 53 26.8	−48 45 03	12.09	0.01	Sy2	IC 1198	16 08 36.3	+12 19 51	14.94	0.03	Sy1
6dF J1254564-265702	12 54 56.3	−26 57 04	16.50	0.06	Sy1	WKK 6092	16 11 51.5	−60 37 55	14.70	0.02	Sy1
3C 279	12 56 11.1	−05 47 22	17.75	0.538	FSRQ	3C 332	16 17 42.7	+32 22 34	17.45	0.15	Sy1
Mrk 231	12 56 14.2	+56 52 25	13.84	0.041	Sy1	MCG+14 08 004	16 19 19.2	+81 02 48	—	0.03	Sy2
NGC 4939	13 04 14.3	−10 20 23	13.80	0.01	Sy2	VII Zw653	16 25 26.1	+85 29 42	16.30	0.06	Sy1
NGC 4945	13 05 27.6	−49 28 03	14.40	0.00	Sy2	Mrk 1498	16 28 04.2	+51 46 31	17.00	0.06	Sy2
ESO 323-G077	13 06 26.2	−40 24 52	13.42	0.02	Sy1	ESO137 34	16 35 14.2	−58 04 41	12.20	0.01	Sy2
NGC 4992	13 09 05.6	+11 38 03	14.34	0.03	Sy1	3C 345	16 42 58.8	+39 48 37	16.59	0.6	FSRQ
Mrk 248	13 15 17.3	+44 24 25	15.10	0.04	Sy2	2MASX J16481523-3035037	16 48 15.2	−30 35 04	15.80	0.03	Sy1
NGC 5100NED02	13 20 59.6	+08 58 42	—	0.03	Sy2	2MASX J16504275+0436180	16 50 42.7	+04 36 18	14.60	0.03	Sy2
IRAS 13197-1627	13 22 24.5	−16 43 42	13.90	0.02	Sy2	ESO 138-G1	16 51 20.5	−59 14 11	13.63	0.01	Sy2
IRAS 13224-3809	13 25 19.2	−38 24 54	13.80*	0.07	NLSy1	NGC 6221	16 52 58.2	−59 13 12	—	0.01	Sy2
ESO509-G038	13 31 13.8	−25 24 09	14.80	0.03	Sy1	NGC 6240	16 52 58.9	+02 24 01	13.37	0.02	Sy2
ESO383 18	13 33 26.0	−34 00 56	13.60	0.01	Sy2	2MASXJ 16531506+2349431	16 53 15.0	+23 49 42	17.80	0.1	Sy2
ESO509 66	13 34 39.7	−23 26 47	16.60	0.03	Sy2	Mrk 501	16 53 52.2	+39 45 36	13.78	0.03	BL Lac
MCG −06−30−15	13 35 53.4	−34 17 48	13.61	0.008	Sy1	2MASS J16561677-3302127	16 56 16.8	−33 02 12	17.50	2.4	FSRQ
NGC 5252	13 38 15.9	+04 32 33	14.21	0.022	Sy2	MCG +05−40−026	17 01 07.8	+29 24 25	15.78	0.036	NLSy1
NGC 5273	13 42 08.3	+35 39 15	13.12	0.003	Sy2	NGC 6300	17 16 59.2	−62 49 05	13.08	0.004	Sy2
Mrk 273	13 44 42.1	+55 53 13	14.91	0.037	Sy2	GRS 1734-292	17 27 28.3	−29 08 02	—	0.02	Sy1
2MASS J1346085+732053	13 46 08.5	+73 20 54	17.40*	0.29	Sy1	PDS 456	17 28 19.9	−14 15 56	14.03	0.18	NLSy1
4U 1344−60	13 47 36.0	-60 37 03.0	19.00	0.013	Sy1	2E 1739.1-1210	17 41 55.3	−12 11 57	16.40	0.04	Sy1
IC 4329A	13 49 19.3	−30 18 34	13.66	0.016	Sy1	4C+18.51	17 42 07.0	+18 27 20	17.50	0.19	Sy1
UM 614	13 49 52.8	+02 04 45	16.23	0.03	Sy2	1RXS J174538.1+290823	17 45 38.3	+29 08 22	14.20	0.11	Sy1
2MASX J14104482-4228325	14 10 44.8	−42 28 33	—	0.03	Sy1	IGR J17476-2253	17 47 35.5	−22 51 18	—	0.05	Sy1
PKS 1409−651	14 13 09.8	−65 20 17	12.10	0.001	Sy2	2MASXi J1802473-145454	18 02 47.3	−14 54 54	16.55#	0.04	Sy1
NGC 5506	14 13 14.8	−03 12 26	14.38	0.007	Sy1	MCG+07 37 031	18 16 09.4	+42 39 22	15.90	0.04	Sy2
NGC 5548	14 17 59.6	+25 08 13	13.73	0.017	Sy1	IGR J18244−5622	18 24 19.4	−56 22 09	14.40	0.017	Sy2
Mrk 813	14 27 25.0	+19 49 51	15.27	0.11	Sy1	LEDA 3097193	18 26 32.4	+32 51 30	....	0.022	Sy2
GBB 1428+4217	14 30 23.7	+42 04 37	22.04	4.72	FSRQ	SX J18305065+0928414	18 30 50.6	+09 28 42	—	0.02	Sy2
NGC 5674	14 33 52.3	+05 27 30	13.70	0.025	Sy2	PKS 1830-21	18 33 39.9	−21 03 40	18.70	2.51	FSRQ
Mrk 817	14 36 22.1	+58 47 40	13.79	0.03	Sy1	3C 382	18 35 03.4	+32 41 47	15.39	0.06	Sy1
Mrk 477	14 40 38.1	+53 30 15	15.03	0.04	Sy2	ESO 103-35	18 38 20.5	−65 25 39	14.53	0.01	Sy2
NGC 5728	14 42 23.9	−17 15 11	13.40	0.009	Sy2	3C 390.3	18 42 09.0	+79 46 17	15.38	0.057	Sy1
IGR J14471-6414	14 46 28.2	−64 16 24	—	0.05	Sy1	1RXS J184642.2+842506	18 46 52.4	+84 25 06	—	—	Sy1
IGR J14552−5133	14 55 17.8	−51 34 17	17.10	0.016	NLSy1	2MASX J18560128+1538059	18 56 00.5	+15 38 56	18.4	0.08	Sy1
IC 4518A	14 57 41.2	−43 07 56	15.00	0.016	Sy2	2E 1849.2−7832	18 57 07.7	−78 28 21	14.50*	0.042	Sy1
3C 309.1	14 59 07.6	+71 40 20	16.78	0.9	Sy1	ESO 231-G026	19 13 14.7	−50 10 59	—	0.06	Sy2
Mrk 841	15 04 01.2	+10 26 16	14.27	0.04	Sy1	PKS 1916-300	19 19 28.0	−29 58 10	—	0.17	Sy2
Mrk 1392	15 05 56.6	+03 42 26	15.50	0.04	Sy2	ESO141-G55	19 21 14.3	-58 40 13.0	13.64	0.037	Sy1
Mrk 1393	15 08 54.0	−00 11 49	16.65	0.05	Sy1	4C+73.18	19 27 48.6	+73 58 02	16.06	0.3	FSRQ
SWIFT J1514.5-8123	15 14 42.0	−81 23 38	17.30*	0.068	Sy1	2MASX J19301380+3410495	19 30 13.8	+34 10 49	15.90#	0.06	Sy1
NGC 5899	15 15 03.3	+42 02 59	13.21	0.01	Sy2	2MASS J19334715+3254259	19 33 47.1	+32 54 26	14.50#	0.06	Sy1
SDSS J152132.21+391206.9	15 21 33.1	+39 12 02	14.10	0.03	Sy1	PMN J1936-4719	19 36 56.1	−47 19 50	20.30	0.27	BL Lac
2MASX J15295830-1300397	15 29 58.3	−13 00 40	—	0.1	Sy2	IGR J19378-0617	19 37 33.1	−06 13 05	15.35	0.01	Sy1
1E 1530-085	15 33 18.9	−08 41 25	15.70	0.02	Sy2	2MASX J19380437-5109497	19 38 04.5	−51 09 47	15.20	0.04	Sy1
Mrk 290	15 35 52.3	+57 54 09	15.30	0.030	Sy1	NGC 6814	19 42 40.7	−10 19 23	14.21	0.01	Sy1
NGC 5995	15 48 25.0	−13 45 27	13.69	0.03	Sy2	IGR J19473+4452	19 47 19.4	+44 49 42	15.70	0.053	Sy2

Table 2.6: Details of the sources analysed for flux variability in this work. Columns have the same meaning as in Table 2.3

Name	α(2000)	δ(2000)	V	z	Ty pe	Name	α(2000)	δ(2000)	V	z	Type
3C 403	19 52 15.9	+02 30 24	16.50	0.059	Sy2	PKS 2155−304	21 58 52.0	−30 13 32	13.09	0.116	BL Lac
1RXS J195815.6-301119	19 58 14.9	−30 11 12	14.00$	0.12	BL Lac	Mrk 520	22 00 41.4	+10 33 09	15.20	0.03	Sy2
MCG +07−41−003	19 59 28.3	+40 44 02	15.10	0.056	Sy2	NGC 7172	22 02 01.9	-31 52 08.0	13.61	0.009	Sy2
1ES 1959+650	19 59 59.9	+65 08 55	12.80	0.05	BL Lac	BL Lac	22 02 43.3	+42 16 39	14.72	0.069	BL Lac
2MASX J20005575-1810274	20 00 55.7	−18 10 28	15.21	0.04	Sy2	ESO 344-G016	22 14 42.0	−38 48 24	14.54	0.04	Sy1
PKS 2008-159	20 11 15.7	−15 46 40	18.30	1.18	FSRQ	3C 445	22 23 49.7	−02 06 13	15.77	0.06	Sy1
SWIFT J2015.2+2526	20 14 59.3	+25 23 01	—	0.045	Sy2	CTA 102	22 32 36.4	+11 43 51	16.70$	1.04	FSRQ
QSO B2013+370	20 15 30.6	+37 12 49	—	0.86	FSRQ	NGC 7314	22 35 46.1	-26 03 02.0	13.11	0.005	Sy2
IGR J20187+4041	20 18 38.7	+40 41 00	....	0.014	Sy2	Mrk 915	22 36 46.5	−12 32 42	14.50	0.03	Sy2
IGR J20216+4359	20 21 49.0	+44 00 39	19.14#	0.02	Sy2	MCG+01-57-016	22 40 17.1	+08 03 14	14.45	0.03	Sy2
4C+21.55	20 33 32.0	+21 46 21	16.20#	0.17	Sy1	Ark 564	22 42 39.3	+29 43 32	14.16	0.03	NLSy1
2MASX J20350566+2603301	20 35 05.6	+26 03 30	—	0.05	Sy1	3C 452	22 45 48.8	+39 41 15	16.56	0.08	Sy2
4C 74.26	20 42 37.3	+75 08 02	15.13	0.1	Sy1	MCG 03 58 007	22 49 37.1	−19 16 27	14.79	0.03	Sy2
Mrk 509	20 44 09.7	-10 43 24.0	13.12	0.035	Sy1	MR 2251-178	22 54 05.9	−17 34 55	14.36	0.06	Sy1
IC 5063	20 52 02.2	−57 04 08	13.60	0.011	Sy2	2MASX J23013626-5913210	23 01 36.2	−59 13 19	17.40*	0.15	Sy1
S5 2116+81	21 14 01.6	+82 04 47	15.70	0.09	Sy1	NGC 7469	23 03 15.6	+08 52 26	13.04	0.02	Sy1
2MASX J21192912+3332566	21 19 29.1	+33 32 57	—	0.05	Sy1	Mrk 926	23 04 43.5	−08 41 08	15.91	0.05	Sy1
IGR J21247+5058	21 24 39.4	+50 58 25	15.40#	0.02	Sy1	UGC 12348	23 05 18.9	+00 11 21	15.30	0.03	Sy2
IGR J21277+5656	21 27 44.9	+56 56 40	18.79	0.014	NLSy1	NGC 7582	23 18 23.5	−42 22 14	13.57	0.01	Sy1
1RXS J213445.2-272551	21 34 45.1	−27 25 55	—	0.07	Sy1	NGC 7674	23 27 56.7	+08 46 44	14.36	0.03	Sy2
RX J2145.5+1102	21 45 32.8	+11 02 56	17.24	0.21	Sy1	IGR J23524+5842	23 52 22.1	+58 45 31	18.62#	0.16	Sy2
PKS 2145+06	21 48 05.5	+06 57 39	16.47	1	FSRQ	PKS 2356-61	23 59 04.3	−60 54 59	16.00	0.1	Sy2
IRAS 21483+1352	21 50 46.8	+14 06 37	—	0.03	Sy2	H 2356-309	23 59 07.8	−30 37 39	15.80$	0.17	BL Lac
PKS 2149−306	21 51 55.4	−30 27 54	17.90	2.345	FSRQ						

2.2.2 Spectral

Spectral analysis requires quality data with high S/N. We therefore looked at the HEASARC archives [‡] for observations from *NuSTAR* that are open for use between the period June 2012 - June 2018. From this, we focussed on 12 nearby objects, that are also reasonably bright with net count rate in the 3−79 keV band greater than 0.1. The details of these 12 objects selected for this study are given in Table 2.7.

[‡] https://heasarc.gsfc.nasa.gov/cgi-bin/W3Browse/w3browse.pl

TABLE 2.7: Details of the selected objects for spectral analysis. The columns are: (1) running number,(2) name of the source, (3) right ascension, (4) declination, (5) redshift, (6) V-band magnitude, (7) type of the source, (8) Observational IDs, (9) date of observation and (10) the exposure time in seconds. The values of α_{2000}, δ_{2000}, z, V-band magnitude and type of the source were taken from Véron-Cetty & Véron (2010) catalog

No. (1)	Name (2)	α_{2000} (3)	δ_{2000} (4)	z (5)	V (mag) (6)	Type (7)	OBSID (8)	Date (9)	Exposure (10)
1.	Mrk 348	00:48:47.2	+31:57:25.0	0.014	14.59	Sy1h	60160026002	2015-10-28	21520
2.	Mrk 1040	02:28:14.4	+31:18:41.0	0.016	14.74	Sy1	60101002002	2015-08-12	62960
							60101002004	2015-08-15	64252
3.	3C 120	04 33 11.1	+05 21 15	0.033	15.05	Sy1	60001042003	2013-02-06	127731
4.	ESO 362−G18	05:19:35.8	-32:39:27.0	0.013	13.37	Sy1.5	60201046002	2016-09-24	101906
5.	NGC 2992	09:45:42.0	-14:19:35.0	0.008	13.78	Sy1.9	60160371002	2015-12-02	20798
6.	NGC 3783	11:39:01.8	-37:44:19.0	0.009	13.43	Sy1.5	60101110002	2016-08-22	41271
							60101110004	2016-08-24	42434
7.	NGC 4151	12:10:32.5	+39:24:21	0.003	11.85	Sy1	60001111002	2012-11-12	21864
							60001111003	2012-11-12	57036
							60001111005	2012-11-14	61531
8.	4U 1344−60	13:47:36.0	-60:37:03.0	0.013	19.00	Sy1	60201041002	2016-09-17	99464
9.	ESO141-G55	19:21:14.3	-58:40:13.0	0.037	13.64	Sy1.2	60201042002	2016-07-15	93011
10.	Mrk 509	20:44:09.7	-10:43:24.0	0.035	13.12	Sy1.5	60101043002	2015-04-29	165893
							60101043004	2015-06-02	36475
11.	NGC 7172	22:02:01.9	-31:52:08.0	0.009	13.61	Sy2	60061308002	2014-10-07	32001
12.	NGC 7314	22:35:46.1	-26:03:02.0	0.005	13.11	Sy1h	60201031002	2016-05-13	100424

2.3 Data reduction: Timing

We reduced the data using the standard tasks *nupipeline* and *nuproducts* available in the *NuSTAR* Data Analysis Software package *NuSTARDAS* version 1.6.0 [§] and distributed by the High Energy Astrophysics Archive Research Center (HEASARC). We used *NuSTAR* CALDB 20161207 to generate the cleaned and screened event files. We also accounted for the passage of the satellite through the South Atlantic Anomaly while doing the analysis. Source light curves were extracted using a circular region of radius 60″ centred on the source for both the focal plane modules

[§]https://heasarc.gsfc.nasa.gov/docs/nustar/analysis/nustar_swguide.pdf

FPMA and FPMB ¶. A circular region of radius 70″ was used to extract the background light curves away from the source on the same detector. Light curves were generated using a time bin of 300 seconds in the soft (3−10 keV), hard (10−79 keV) and total (3−79 keV) energy ranges for both the focal plane modules. The task *lcmath* available in FTOOLS V6.19 was used to combine the light curves from the two modules FPMA and FPMB. Once the combined light curves were generated, we analysed them for the presence of outliers as well as the presence of points with large error bars. To remove both outliers and those with large error bars, we calculated the mean and standard deviation of the light curves as well as the mean and standard deviation of the errors. The following two conditions were then imposed on the light curves to generate the final light curves namely (a) the error on any data point in a light curve must be less than 5 times the standard deviation of the errors and (b) the difference between a data point in a light curve and the mean of the same light curve must be less than 5 times the standard deviation of the light curve.

2.4 Data reduction: Spectral

Initial processing of the data was carried out following the procedures outlined in Section 2.3. We extracted the spectra and corresponding response files using *nuproducts* task, with a circular region of 60″ at the peak of the source and 70″ radius circular background region away from the source on the same chip. For spectral analysis, we fitted both the focal plane modules FPMA and FPMB spectra simultaneously allowing the cross normalization for both modules to vary. In this fitting process, the abundances of the elements were fixed to their solar values (Anders & Grevesse 1989). We used *XSPEC* (version 12.9.0; Arnaud 1996) for the spectral fitting. The χ^2 minimization technique in *XSPEC* was used to get the

¶https://heasarc.gsfc.nasa.gov/docs/nustar/

best model description of the data and all errors were calculated using $\chi^2 = 2.71$ criterion i.e. 90% confidence range for one parameter of interest.

Chapter 3

A comparative study of the X-ray flux variability characteristics of different classes of AGN with NuSTAR †

In this chapter, we present the results on our comparative study on the hard X-ray flux variability characteristics of different classes of AGN on hour like timescales. The details on the selection of sample for this comparative study and the procedures followed to generate light curves are given in Chapter 2. Our final sample for this comparative study consists of 335 sources. They include 24 BL Lacs, 24 FSRQs, 20 NLSy1 galaxies, 121 Seyfert 1 galaxies and 146 Seyfert 2 galaxies. The distribution of the sources is shown in Figure 3.1. In the same figure is also shown the fractional distribution of the different types of AGN. In terms of percentage,

†The contents of this chapter are
1. Under review in Rani et al. 2019, MNRAS
2. Published in Rani P., Stalin C. S., Rakshit S., 2017, MNRAS, 466, 3309 .

44% of the sources are Seyfert 2 galaxies, 36% are Seyfert 1 galaxies, 7% are BL Lacs, 6% are NLSy1 galaxies, and FSRQs comprise 7%. In addition to finding differences if any in the hard X-ray variability characteristics of different classes of AGN, we also investigated here the dependence of variability against various physical characteristics of the sources.

3.1 Variability Amplitude

An example light curve of one of the objects in our sample analysed for flux variability is given in Figure 3.2. From the figure, it is evident that the source has varied in the soft (3-10 keV), hard (10-79 keV) and total (3−79 keV) energy bands. To check for flux variations in the observed count rates in soft, hard and total energy bands and to quantify the flux variability, we calculated the excess variance also called the fractional root mean square variability amplitude ($F_{\rm var}$). $F_{\rm var}$ gives an estimate of the intrinsic variability amplitude of the sources relative to their mean count rate after removal of the contribution of the measurement errors and thus gives an estimate of the intrinsic variability amplitude of the sources (Edelson et al. 2002; Vaughan et al. 2003). Following Vaughan et al. (2003), $F_{\rm var}$ is defined as

$$F_{\rm var} = \sqrt{\frac{S^2 - \bar{\sigma^2}_{\rm err}}{\bar{x}^2}} \tag{3.1}$$

where S^2 represents the sample variance, $\bar{x}$ is the arithmetic mean of x_i and $\bar{\sigma^2}_{\rm err}$ represents the mean square error. S^2 and $\bar{\sigma^2}_{\rm err}$ are given as

$$S^2 = \frac{1}{N-1}\sum_{i=1}^{N}(x_i - \bar{x})^2 \tag{3.2}$$

$$\bar{\sigma^2}_{\rm err} = \frac{1}{N}\sum_{i=1}^{N}\sigma^2_{\rm err,i} \tag{3.3}$$

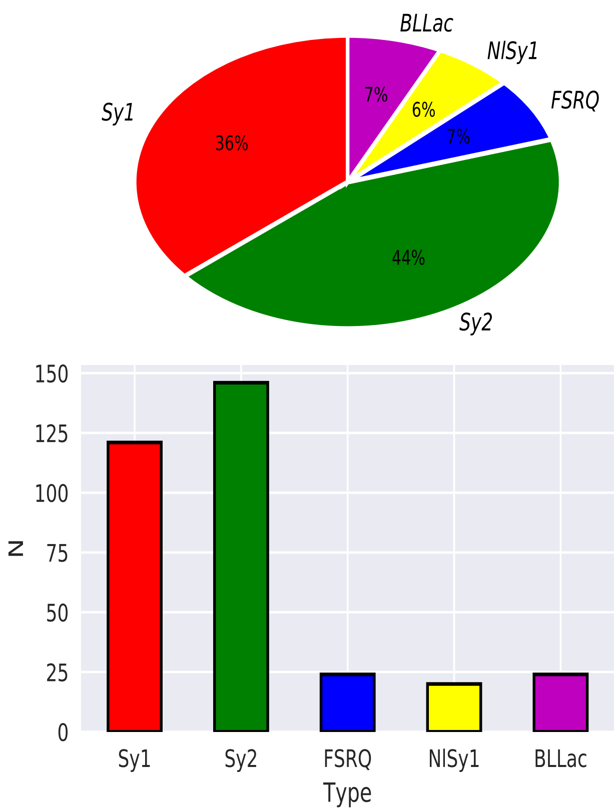

FIGURE 3.1: Top: Pie chart showing the relative number of the different classes of AGN. Bottom: Histogram of the number of different type of sources.

The uncertainty in $F_{\rm var}$ is given by

$$err(F_{\rm var}) = \sqrt{\left(\sqrt{\frac{1}{2N}}\frac{\overline{\sigma^2}_{\rm err}}{\bar{x}^2 F_{\rm var}}\right)^2 + \left(\sqrt{\frac{\overline{\sigma^2}_{\rm err}}{N}}\frac{1}{\bar{x}}\right)^2} \tag{3.4}$$

The values of $F_{\rm var}$ for the sources that are found to be variable are listed in Tables 3.1, 3.2, 3.3, 3.4, 3.5, 3.6, 3.7 and 3.8. About 60% of the sources in our sample are found to be variable. The number of observations (OBSIDs) where variability has been observed are 65 in blazars (BL Lacs = 46, FSRQs = 19), 113 in Seyfert 1 galaxies, 113 in Seyfert 2 galaxies and 32 in NLSy1 galaxies. The weighted mean values of $F_{\rm var}$ in different classes of AGN are given in Table 3.9.

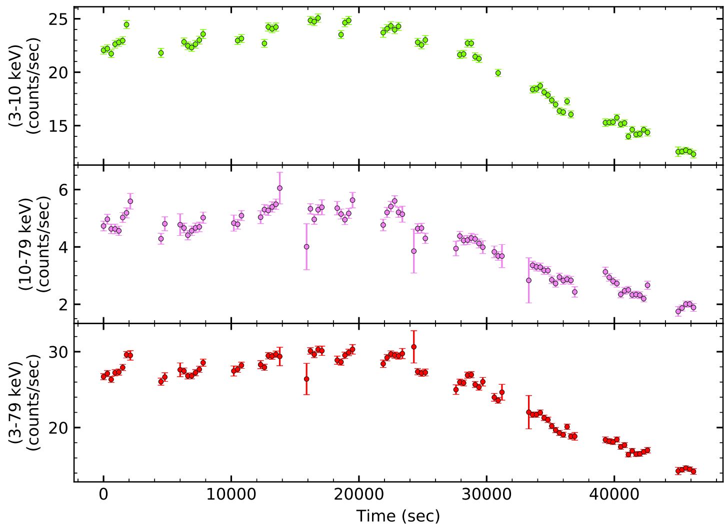

FIGURE 3.2: Light curves of the BL Lac object Mrk 421 corresponding to the observational ID 60202048004 and observed by *NuSTAR* on 2017-01-31 for a duration of 21564 sec. Shown from the top to the bottom are the flux variations in the energy ranges of 3−10 keV (soft band), 10−79 keV (hard band) and 3−79 keV (total band) respectively. Each point corresponds to a binning of 300 seconds.

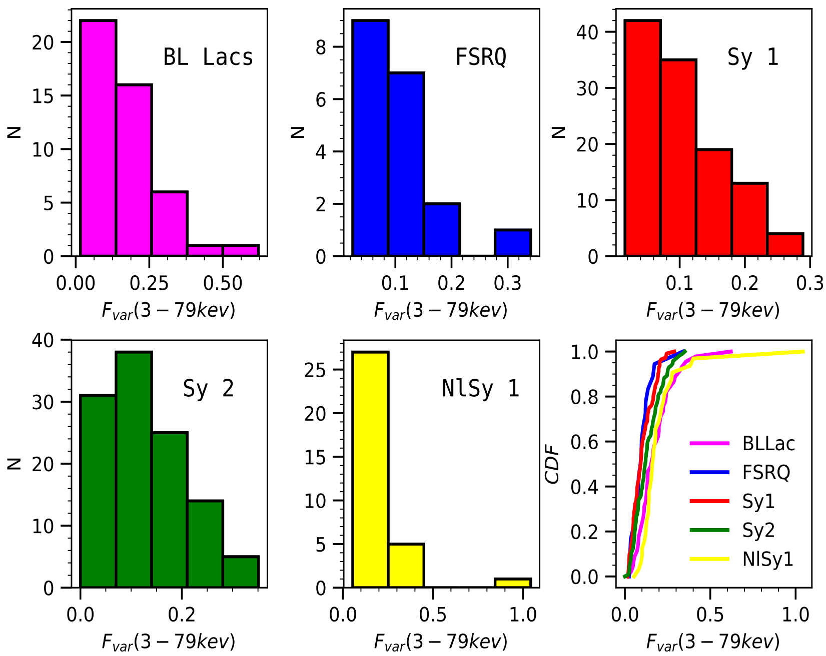

FIGURE 3.3: Histogram of $F_{\rm var}$ in the 3−79 keV band for different classes of AGN. The bottom right panel is the cumulative distribution function of $F_{\rm var}$ in the 3−79 keV band for different types of AGN.

TABLE 3.1: Results of the analysis of variability. Column information are as follows (1) name of the source (2) type of the source, (3) observational ID, (4) date of observation, (5) exposure time in seconds (6), (7), (8) are the $F_{\rm var}$ and error in the soft, hard and total bands respectively.

Name	Type	OBS ID	Date	Exposure	$F_{\rm var} \pm err(F_{\rm var})$		
					3−10 keV	10−79 keV	3−79 keV
1ES 0502+675	BL Lac	60202026002	2016-11-02	24708	0.029±0.012	0.217±0.037	0.057±0.011
1ES 1218+304	BL Lac	60101034002	2015-11-23	49551	0.114±0.011	0.156±0.025	0.112±0.011
1ES 1959+650	BL Lac	60002055002	2014-09-17	19612	0.276±0.009	0.375±0.017	0.287±0.008
BZB J0123-2310	BL Lac	60101060002	2015-09-08	21761	0.113±0.023	0.273±0.052	0.128±0.021
Mrk 421	BL Lac	10002015001	2012-07-07	42034	0.209±0.003	0.247±0.008	0.225±0.004
		10002016001	2012-07-08	24885	0.305±0.003	0.430±0.009	0.358±0.004
		60002023002	2013-01-02	9152	0.068±0.010	0.168±0.027	0.088±0.013
		60002023004	2013-01-10	22633	0.119±0.008	0.146±0.021	0.132±0.010
		60002023006	2013-01-15	24182	0.199±0.004	0.302±0.012	0.243±0.005
		60002023008	2013-01-20	24968	0.084±0.007	0.159±0.020	0.095±0.009
		60002023010	2013-02-06	19307	0.097±0.005	0.095±0.014	0.108±0.006
		60002023012	2013-02-12	14780	0.204±0.005	0.280±0.012	0.241±0.006
		60002023014	2013-02-16	17359	0.231±0.013	0.220±0.034	0.237±0.020
		60002023016	2013-03-04	17252	0.122±0.005	0.115±0.016	0.122±0.007
		60002023018	2013-03-11	17474	0.144±0.005	0.112±0.014	0.125±0.006
		60002023020	2013-03-17	16558	0.088±0.004	0.125±0.012	0.102±0.006
		60002023022	2013-04-02	24772	0.223±0.004	0.378±0.011	0.295±0.006
		60002023024	2013-04-10	5758	0.146±0.005	0.164±0.013	0.165±0.006
		60002023025	2013-04-11	57509	0.599±0.001	0.638±0.004	0.621±0.002
		60002023027	2013-04-12	7630	0.134±0.002	0.172±0.005	0.150±0.002
		60002023029	2013-04-13	16510	0.221±0.002	0.226±0.005	0.224±0.002
		60002023031	2013-04-14	15606	0.312±0.001	0.361±0.002	0.335±0.001
		60002023033	2013-04-15	17278	0.192±0.006	0.248±0.005	0.199±0.008
		60002023035	2013-04-16	20279	0.391±0.002	0.441±0.004	0.414±0.002
		60002023037	2013-04-18	17795	0.181±0.005	0.212±0.013	0.199±0.006
		60002023039	2013-04-19	15958	0.120±0.005	0.149±0.013	0.134±0.006
		60202048002	2017-01-03	23691	0.079±0.002	0.074±0.006	0.076±0.002
		60202048004	2017-01-31	21564	0.190±0.002	0.283±0.005	0.205±0.002
		60202048006	2017-02-28	23906	0.166±0.002	0.192±0.006	0.169±0.002
		60202048008	2017-03-27	31228	0.260±0.003	0.305±0.007	0.266±0.003
Mrk 501	BL Lac	60002024004	2013-05-08	26141	0.138±0.007	0.238±0.019	0.163±0.008
		60002024006	2013-07-12	10857	0.043±0.004	0.059±0.008	0.047±0.005
		60002024008	2013-07-13	10343	0.069±0.007	0.094±0.012	0.081±0.007
		60202049002	2017-04-27	23151	0.047±0.006	0.086±0.012	0.051±0.005
RBS 0970	BL Lac	60101062002	2015-11-04	22502	0.113±0.023	0.110±0.066	0.113±0.022
RGB J0710+591	BL Lac	60101037002	2015-09-01	3920	0.063±0.023	0.130±0.051	0.070±0.021
		60101037004	2015-09-01	26477	0.013±0.011	0.088±0.022	0.037±0.010

Table 3.2: Results of the analysis of variability. Column information are the same as in Table 3.1.

Name	Type	OBS ID	Date	Exposure	$F_{\rm var} \pm err(F_{\rm var})$		
					3−10 keV	10−79 keV	3−79 keV
OJ 287	BL Lac	90201054002	2017-04-09	53002	0.133±0.013	0.119±0.023	0.130±0.011
S5 0716+714	BL Lac	90002003002	2015-01-24	18583	0.185±0.014	0.187±0.026	0.183±0.012
PKS 0352−686	BL Lac	60160169002	2016-04-14	21227	0.018±0.011	0.143±0.026	0.016±0.010
PMN J0847−2337	BL Lac	60101059002	2015-12-19	32143	0.214±0.018	0.144±0.044	0.195±0.017
PKS 2155−304	BL Lac	10002010001	2012-07-08	33838	0.108±0.008	0.270±0.020	0.127±0.010
		60002022004	2013-07-16	13856	0.124±0.020	0.223±0.046	0.134±0.022
		60002022008	2013-08-08	13496	0.110±0.040	0.093±0.054	0.156±0.054
		60002022012	2013-08-26	11356	0.198±0.013	0.197±0.030	0.209±0.015
		60002022014	2013-09-04	12282	0.151±0.019	0.074±0.043	0.079±0.024
3C 273	FSRQ	00015013001	2012-07-02	2573	0.341±0.013	0.344±0.019	0.341±0.012
		00015016001	2012-07-02	2990	0.140±0.018	0.181±0.028	0.164±0.017
		10002020001	2012-07-14	244003	0.068±0.002	0.075±0.002	0.072±0.001
		10012007001	2012-07-13	4530	0.090±0.013	0.099±0.021	0.096±0.013
		10002020003	2015-07-13	49414	0.028±0.004	0.020±0.005	0.024±0.003
		10202020002	2016-06-26	35416	0.028±0.003	0.040±0.004	0.027±0.002
		10302020002	2017-06-26	35398	0.029±0.004	0.039±0.005	0.034±0.003
3C 279	FSRQ	60002020002	2013-12-16	39594	0.104±0.009	0.102±0.014	0.098±0.009
		60002020004	2013-12-31	42810	0.164±0.007	0.174±0.010	0.173±0.006
PKS 2149−306	FSRQ	60001099004	2014-04-18	44167	0.092±0.008	0.055±0.011	0.120±0.007
4C 25.05	FSRQ	60201047002	2017-01-15	41783	0.125±0.021	0.066±0.033	0.091±0.018
HB0836+710	FSRQ	60002045002	2013-12-15	29697	0.056±0.009	0.113±0.015	0.080±0.008
		60002045004	2014-01-18	36398	0.032±0.006	0.064±0.009	0.031±0.005
CTA 102	FSRQ	90202044002	2016-12-30	26211	0.067±0.005	0.028±0.006	0.057±0.004
S5 1039+81	FSRQ	90201018002	2016-04-12	14692	0.144±0.023	0.178±0.033	0.107±0.020
2MASS J16561677-3302127	FSRQ	60160657002	2015-09-27	21140	0.137±0.019	0.065±0.031	0.135±0.016
HB89 0212+735	FSRQ	60160099002	2016-02-24	30344	0.056±0.012	0.030±0.018	0.051±0.010
PMN J0525-2338	FSRQ	60160234002	2017-04-26	20934	0.145±0.027	0.242±0.042	0.122±0.023
GBB 1428+4217	FSRQ	60001103002	2014-07-14	49186	0.038±0.023	0.228±0.035	0.078±0.019
TON S180	NLSy1	60201057002	2016-06-10	127353	0.282±0.010	0.232±0.022	0.254±0.009
Mrk 1044	NLSy1	60160109002	2016-02-08	21684	0.180±0.014	0.261±0.027	0.158±0.012
PKS 0558-504	NLSy1	60160254002	2016-11-19	20983	0.118±0.017	0.217±0.036	0.114±0.014
IRAS F11119+3257	NLSy1	60101045002	2015-05-12	104494	0.165±0.019	0.319±0.043	0.149±0.018
QSO B1114-2846	NLSy1	60061209002	2017-05-05	19923	0.258±0.031	0.178±0.047	0.208±0.027
Mrk 739E	NLSy1	60260008002	2017-03-16	18547	0.198±0.022	0.140±0.038	0.215±0.019
PG 1211+143	NLSy1	60001100002	2014-02-18	111438	0.168±0.010	0.036±0.021	0.155±0.009
		60001100004	2014-04-08	48949	0.150±0.013	0.146±0.024	0.141±0.011
		60001100005	2014-04-09	64430	0.114±0.010	0.119±0.020	0.094±0.009
		60001100007	2014-07-07	74887	0.128±0.013	0.201±0.022	0.121±0.011
Mrk 766	NLSy1	60101022002	2015-07-05	23567	0.232±0.010	0.213±0.019	0.226±0.009
		60001048002	2015-01-24	90174	0.173±0.004	0.144±0.008	0.166±0.004
IRAS 13224-3809	NLSy1	60202001012	2016-08-01	171657	0.935±0.022	1.725±0.143	1.043±0.036
UGC 10120	NLSy1	60361013002	2018-03-22	26036	0.161±0.026	0.189±0.051	0.141±0.023
1H 0323+342	NLSy1	60061360002	2014-03-15	101633	0.141±0.010	0.172±0.017	0.138±0.010
MCG +04−22−042	NLSy1	60061092002	2012-12-26	18845	0.020±0.009	0.085±0.015	0.081±0.009

TABLE 3.3: Results of the analysis of variability. Column information are the same as in Table 3.1.

Name	Type	OBS ID	Date	Exposure	$F_{\rm var} \pm err(F_{\rm var})$		
					3−10 keV	10−79 keV	3−79 keV
NGC 4051	NLSy1	60001050002	2013-06-17	9434	0.225±0.014	0.058±0.024	0.168±0.014
		60001050003	2013-06-17	45737	0.341±0.006	0.214±0.010	0.277±0.006
		60001050005	2013-10-09	10202	0.164±0.016	0.064±0.024	0.128±0.015
		60001050006	2013-10-09	49621	0.352±0.009	0.198±0.012	0.273±0.008
		60001050008	2014-02-16	56683	0.226±0.005	0.132±0.009	0.180±0.005
IGR J14552−5133	NLSy1	60061259002	2013-09-19	21943	0.170±0.017	0.148±0.027	0.160±0.017
MCG +05−40−026	NLSy1	60061276002	2013-12-19	20999	0.147±0.019	0.111±0.029	0.073±0.018
PDS 456	NLSy1	60002032010	2014-02-26	109717	0.144±0.020	0.161±0.037	0.180±0.022
		90101008002	2015-07-21	77127	0.174±0.014	0.171±0.028	0.176±0.013
		90101008004	2015-07-24	40885	0.256±0.018	0.278±0.038	0.232±0.016
		60201020002	2017-03-23	158173	0.411±0.018	0.542±0.044	0.400±0.017
Ark 564	NLSy1	60101031002	2015-05-22	211226	0.386±0.003	0.385±0.009	0.383±0.003
IGR J21277+5656	NLSy1	60001110002	2012-11-04	49202	0.143±0.006	0.122±0.010	0.138±0.006
		60001110003	2012-11-05	28765	0.096±0.007	0.019±0.012	0.054±0.007
		60001110005	2012-11-06	74583	0.139±0.004	0.112±0.007	0.124±0.004
		60001110007	2012-11-08	42110	0.128±0.006	0.085±0.009	0.101±0.006
Mkn 335	Sy1	60001041002	2013-06-13	21299	0.190±0.026	0.292±0.032	0.204±0.022
		60001041003	2013-06-13	21525	0.179±0.025	0.045±0.034	0.188±0.023
		60001041005	2013-06-25	93028	0.157±0.009	0.045±0.013	0.114±0.008
		80001020002	2014-09-20	68908	0.167±0.008	0.163±0.014	0.160±0.007
3C 120	Sy1	60001042002	2013-02-06	21606	0.047±0.006	0.035±0.010	0.036±0.006
		60001042003	2013-02-06	127731	0.074±0.003	0.017±0.005	0.044±0.003
Mrk 9	Sy1	60061326002	2013-10-29	23310	0.066±0.026	0.104±0.035	0.113±0.024
2MASX J00341665-7905204	Sy1	60160015002	2016-03-28	22668	0.038±0.014	0.419±0.126	0.041±0.012
MCG-03-04-072	Sy1	60160061002	2015-01-12	21879	0.027±0.012	0.054±0.019	0.047±0.010
RBS 0295	Sy1	60061021002	2017-01-14	23367	0.187±0.018	0.195±0.030	0.191±0.015
Mrk 590	Sy1	90201043002	2016-12-02	51003	0.146±0.014	0.171±0.023	0.124±0.012
		60160095002	2016-02-05	21206	0.119±0.024	0.127±0.038	0.133±0.020
AM 0224-283	Sy1	60363002002	2017-06-17	22063	0.042±0.024	0.290±0.040	0.134±0.021
NGC 1275	Sy1	60061361002	2015-11-03	19874	0.014±0.005	0.053±0.011	0.021±0.004
		90202046004	2017-02-04	28169	0.014±0.004	0.139±0.009	0.016±0.004
1H 0419-577	Sy1	60101039002	2015-06-03	169473	0.040±0.004	0.037±0.006	0.036±0.003
2MASX J04372814-4711298	Sy1	60160197002	2015-12-09	19986	0.211±0.020	0.168±0.037	0.178±0.017
IRAS 04392-2713	Sy1	60160201002	2015-12-20	19556	0.081±0.016	0.113±0.028	0.083±0.014
Ark 120	Sy1	60001044004	2014-03-22	65458	0.051±0.004	0.058±0.006	0.049±0.003
4U 1344−60	Sy1	60201041002	2016-09-17	99464	0.105±0.003	0.094±0.004	0.101±0.002
ESO 141−G055	Sy1	60201042002	2016-07-15	93011	0.099±0.004	0.075±0.006	0.094±0.003
ESO 362−G18	Sy1	60201046002	2016-09-24	101906	0.222±0.006	0.150±0.008	0.195±0.005
Mrk 1040	Sy1	60101002002	2015-08-12	62960	0.089±0.005	0.069±0.007	0.081±0.004
		60101002004	2015-08-15	64252	0.099±0.005	0.070±0.008	0.090±0.004
Mrk 509	Sy1	60101043002	2015-04-29	165893	0.033±0.002	0.044±0.003	0.032±0.002
		60101043004	2015-06-02	36475	0.044±0.005	0.085±0.008	0.049±0.004
NGC 3783	Sy1	60101110002	2016-08-22	41271	0.097±0.006	0.041±0.009	0.093±0.005
		60101110004	2016-08-24	42434	0.057±0.005	0.017±0.006	0.044±0.004

TABLE 3.4: Results of the analysis of variability. Column information are the same as in Table 3.1.

Name	Type	OBS ID	Date	Exposure	$F_{\rm var} \pm err(F_{\rm var})$		
					3−10 keV	10−79 keV	3−79 keV
MCG+8-11-11	Sy1	60201027002	2016-08-16	97925	0.053±0.003	0.048±0.004	0.050±0.003
IRAS 05581+0006	Sy1	60160255002	2015-12-12	21146	0.103±0.030	0.146±0.033	0.053±0.022
MCG+02 21 013	Sy1	60260001002	2017-03-11	20336	0.181±0.020	0.186±0.026	0.166±0.016
Mrk 704	Sy1	60061090002	2014-12-28	21523	0.096±0.013	0.140±0.017	0.071±0.011
Mrk 110	Sy1	60201025002	2017-01-23	184563	0.054±0.002	0.049±0.004	0.053±0.002
MCG-5-23-16	Sy1	10002019001	2012-07-16	33927	0.088±0.003	0.074±0.005	0.082±0.003
		60001046002	2013-06-03	160478	0.104±0.003	0.097±0.005	0.096±0.003
		60001046004	2015-02-15	210887	0.138±0.002	0.120±0.002	0.132±0.001
		60001046006	2015-02-21	98472	0.104±0.002	0.083±0.004	0.096±0.002
		60001046008	2015-03-13	220845	0.110±0.001	0.091±0.002	0.103±0.001
3C 227	Sy1	60061329004	2014-02-26	12064	0.036±0.018	0.158±0.023	0.066±0.016
NGC 3516	Sy1	60002042004	2014-07-11	72089	0.053±0.010	0.122±0.014	0.060±0.009
Mrk 732	Sy1	60061208002	2013-06-11	26359	0.043±0.013	0.041±0.019	0.085±0.013
NGC 4151	Sy1	60001111002	2012-11-12	21864	0.049±0.003	0.058±0.004	0.050±0.002
		60001111003	2012-11-12	57036	0.099±0.004	0.081±0.003	0.069±0.003
		60001111005	2012-11-14	61531	0.099±0.002	0.082±0.003	0.088±0.002
Mrk 231	Sy1	60002025004	2013-05-09	28557	0.215±0.044	0.149±0.062	0.047±0.041
MCG −06−30−15	Sy1	60001047002	2013-01-29	23270	0.225±0.007	0.181±0.012	0.199±0.007
		60001047003	2013-01-30	127232	0.314±0.003	0.263±0.005	0.289±0.003
		60001047005	2013-02-02	29646	0.173±0.007	0.140±0.010	0.154±0.006
NGC 5506	Sy1	60061323002	2014-04-01	56585	0.072±0.004	0.052±0.006	0.063±0.004
NGC 5548	Sy1	60002044006	2013-09-10	51460	0.066±0.005	0.094±0.007	0.066±0.005
		60002044008	2013-12-20	50103	0.057±0.006	0.054±0.008	0.073±0.006
Mrk 290	Sy1	60061266002	2013-11-14	25012	0.087±0.013	0.032±0.020	0.023±0.013
		60061266004	2013-11-27	26348	0.038±0.014	0.173±0.021	0.057±0.013
3C 390.3	Sy1	60001082002	2013-05-24	23643	0.042±0.006	0.062±0.010	0.053±0.006
		60001082003	2013-05-24	47559	0.020±0.005	0.072±0.007	0.020±0.005
ARK 241	Sy1	60160392002	2017-12-22	20329	0.203±0.015	0.207±0.026	0.204±0.013
NGC 3227	Sy1	60202002002	2016-11-09	49800	0.198±0.004	0.119±0.006	0.161±0.004
		60202002004	2016-11-25	42462	0.211±0.007	0.184±0.008	0.193±0.005
		60202002006	2016-11-29	39689	0.218±0.006	0.143±0.008	0.194±0.005
		60202002008	2016-12-01	41818	0.160±0.005	0.096±0.008	0.143±0.004
		60202002010	2016-12-05	40887	0.090±0.006	0.099±0.007	0.083±0.004
		60202002012	2016-12-09	39282	0.091±0.011	0.203±0.007	0.118±0.008
		60202002014	2017-01-21	47602	0.183±0.004	0.133±0.006	0.167±0.003
SDSS J104326d47+110524d2	Sy1	60160406002	2016-06-14	20158	0.212±0.023	0.323±0.048	0.198±0.020
2MASX J10523297+1036205	Sy1	60160414002	2017-01-30	40696	0.127±0.015	0.088±0.021	0.098±0.012
PG 1100+772	Sy1	60463031002	2018-01-02	19803	0.097±0.021	0.096±0.040	0.070±0.019
SBS 1136+594	Sy1	60160443002	2014-12-26	23531	0.060±0.012	0.159±0.021	0.097±0.011
UGC 06728	Sy1	60376007002	2017-10-13	58077	0.258±0.006	0.215±0.010	0.244±0.005
RBS 1037	Sy1	60061215002	2017-02-02	40679	0.080±0.018	0.052±0.032	0.058±0.016
PKS J1220+0203	Sy1	60301001002	2017-06-06	50517	0.173±0.012	0.239±0.022	0.177±0.011
2MASX J12313717−4758019	Sy1	60160498002	2016-08-21	19359	0.267±0.020	0.268±0.032	0.242±0.018
RBS 1125	Sy1	60061229002	2016-07-28	19936	0.135±0.023	0.261±0.045	0.073±0.021

Table 3.5: Results of the analysis of variability. Column information are the same as in Table 3.1.

Name	Type	OBS ID	Date	Exposure	$F_{\rm var} \pm err(F_{\rm var})$		
					3−10 keV	10−79 keV	3−79 keV
NGC 4593	Sy1	60001149002	2014-12-29	23319	0.195±0.016	0.127±0.012	0.170±0.012
		60001149004	2014-12-31	21681	0.087±0.011	0.160±0.015	0.100±0.009
		60001149006	2015-01-02	21333	0.080±0.010	0.034±0.016	0.076±0.009
		60001149010	2015-01-06	21209	0.162±0.008	0.105±0.012	0.109±0.007
6dF J1254564−265702	Sy1	60363001002	2017-06-25	20296	0.076±0.018	0.187±0.031	0.050±0.015
ESO 323-G077	Sy1	60202021002	2016-12-14	39361	0.116±0.017	0.150±0.015	0.084±0.011
		60202021004	2016-12-20	42533	0.148±0.018	0.111±0.016	0.071±0.012
		60202021006	2017-01-04	43403	0.132±0.016	0.111±0.014	0.095±0.011
		60202021008	2017-02-03	43295	0.206±0.015	0.167±0.017	0.172±0.012
NGC 4992	Sy1	60061239002	2015-01-27	23465	0.155±0.023	0.203±0.018	0.174±0.014
2MASS J1346085+732053	Sy1	60160556002	2017-06-25	17965	0.147±0.029	0.239±0.053	0.132±0.025
Mrk 813	Sy1	60160583002	2017-01-23	24562	0.166±0.014	0.129±0.026	0.166±0.013
Mrk 817	Sy1	60160590002	2015-07-25	21922	0.211±0.016	0.221±0.025	0.211±0.013
3C 309.1	Sy1	60376006002	2017-11-16	61099	0.101±0.018	0.063±0.032	0.092±0.016
IC 1198	Sy1	60361014002	2017-05-07	26973	0.080±0.017	0.057±0.025	0.089±0.014
WKK 6092	Sy1	60160632002	2018-04-27	22052	0.177±0.012	0.207±0.019	0.075±0.010
VII Zw653	Sy1	60160639002	2017-06-08	27580	0.109±0.016	0.170±0.030	0.025±0.014
4C +18.51	Sy1	60160672002	2017-03-27	22512	0.121±0.026	0.114±0.047	0.138±0.022
3C 382	Sy1	60202015006	2016-09-22	20825	0.033±0.006	0.017±0.010	0.024±0.005
1RXS J184642.2+842506	Sy1	60464157002	2018-03-27	16004	0.151±0.030	0.233±0.052	0.198±0.027
IGR J19378-0617	Sy1	60101003002	2015-10-01	65527	0.218±0.005	0.200±0.011	0.205±0.005
NGC 6814	Sy1	60201028002	2016-07-04	148436	0.261±0.003	0.202±0.004	0.239±0.002
4C 74.26	Sy1	60001080002	2014-09-21	19065	0.199±0.009	0.160±0.016	0.026±0.009
2MASX J21192912+3332566	Sy1	60061358002	2015-01-17	21484	0.053±0.013	0.086±0.023	0.071±0.012
1RXS J213445.2−272551	Sy1	60061306002	2013-10-22	19809	0.045±0.017	0.139±0.029	0.026±0.017
		60363005002	2017-04-16	21064	0.078±0.015	0.049±0.026	0.047±0.013
ESO 344-G016	Sy1	60361017002	2017-06-29	24868	0.112±0.011	0.135±0.021	0.121±0.010
3C 445	Sy1	60160788002	2016-05-15	19930	0.054±0.016	0.052±0.019	0.059±0.012
MR 2251-178	Sy1	60102025002	2015-05-18	23116	0.023±0.006	0.024±0.009	0.025±0.005
		60102025008	2015-12-11	21709	0.027±0.006	0.072±0.009	0.022±0.005
2MASX J23013626−5913210	Sy1	60160814002	2017-10-05	19500	0.050±0.017	0.104±0.029	0.037±0.015
NGC 7469	Sy1	60101001002	2015-06-12	21579	0.106±0.008	0.053±0.012	0.096±0.007
		60101001006	2015-12-15	22521	0.062±0.008	0.049±0.012	0.042±0.007
		60101001008	2015-12-22	23483	0.041±0.007	0.035±0.011	0.033±0.006
		60101001010	2015-12-25	20846	0.049±0.006	0.064±0.010	0.040±0.005
		60101001014	2015-12-28	23400	0.064±0.006	0.065±0.010	0.056±0.005
Mrk 926	Sy1	60201029002	2016-11-21	106205	0.017±0.003	0.026±0.004	0.022±0.002
NGC 7582	Sy1	60201003002	2016-04-28	48495	0.218±0.007	0.152±0.007	0.183±0.005
		60061318002	2012-08-31	16463	0.152±0.018	0.108±0.016	0.137±0.013
GRS1734-292	Sy1	60061279002	2014-09-16	20293	0.030±0.005	0.025±0.008	0.018±0.005
IC 4329A	Sy1	60001045002	2012-08-12	162399	0.118±0.002	0.103±0.004	0.109±0.002
Fairall 1203	Sy2	60160002002	2015-04-11	34128	0.058±0.018	0.142±0.028	0.077±0.016
Mrk 348	Sy2	60160026002	2015-10-28	21520	0.029±0.006	0.029±0.008	0.026±0.005
NGC 2992	Sy2	60160371002	2015-12-02	20798	0.069±0.005	0.064±0.008	0.067±0.004
NGC 7172	Sy2	60061308002	2014-10-07	32001	0.071±0.005	0.071±0.006	0.077±0.004

TABLE 3.6: Results of the analysis of variability. Column information are the same as in Table 3.1.

Name	Type	OBS ID	Date	Exposure	$F_{\rm var} \pm err(F_{\rm var})$		
					3−10 keV	10−79 keV	3−79 keV
NGC 7314	Sy2	60201031002	2016-05-13	100424	0.271±0.003	0.195±0.005	0.250±0.003
NGC 454E	Sy2	60061009002	2016-02-14	24229	0.265±0.044	0.158±0.038	0.210±0.028
2MASX J01402676-5319389	Sy2	60160072002	2015-03-03	22558	0.118±0.021	0.140±0.028	0.105±0.017
NGC 513	Sy2	60061012002	2013-02-16	16040	0.113±0.027	0.097±0.033	0.115±0.023
NGC 788	Sy2	60061018002	2013-01-28	15411	0.088±0.031	0.110±0.024	0.093±0.020
NGC 1068	Sy2	60002030002	2012-12-18	57851	0.057±0.010	0.054±0.013	0.027±0.008
		60002030004	2012-12-20	48560	0.035±0.010	0.071±0.013	0.065±0.009
		60002030006	2012-12-21	19461	0.052±0.016	0.120±0.020	0.087±0.013
NGC 1365	Sy2	60002046002	2012-07-25	36258	0.276±0.010	0.311±0.034	0.215±0.019
		60002046003	2012-07-26	40588	0.157±0.011	0.103±0.011	0.130±0.008
		60002046005	2012-12-24	66297	0.202±0.005	0.161±0.007	0.172±0.004
		60002046007	2013-01-23	73650	0.431±0.004	0.255±0.007	0.338±0.004
		60002046009	2013-02-12	69877	0.397±0.006	0.218±0.009	0.280±0.006
MCG +03−13−01	Sy2	60061051002	2014-03-18	20088	0.139±0.045	0.047±0.040	0.122±0.031
XSS J05054−2348	Sy2	60061056002	2013-08-21	21161	0.035±0.010	0.077±0.013	0.060±0.009
		60002033002	2014-08-18	52062	0.055±0.011	0.099±0.013	0.056±0.008
MCG+00-09-042	Sy2	60160148002	2016-10-15	24191	0.154±0.016	0.091±0.025	0.080±0.014
SWIFT J0357.5-6255	Sy2	60201034002	2016-05-06	26562	0.121±0.034	0.177±0.026	0.110±0.020
MRSS 302-039347	Sy2	60061341002	2015-04-13	21904	0.189±0.023	0.207±0.041	0.195±0.020
3C 105	Sy2	60261003002	2016-08-21	20740	0.164±0.039	0.158±0.038	0.127±0.027
ESO033 G002	Sy2	60061054002	2014-05-04	23573	0.105±0.011	0.090±0.018	0.103±0.010
2MASX J05043414-7349269	Sy2	60160217002	2016-09-30	22668	0.244±0.042	0.291±0.050	0.167±0.033
Pictor A	Sy2	60101047002	2015-12-03	109459	0.041±0.006	0.141±0.011	0.054±0.005
IRAS 05189−2524	Sy2	60002027002	2013-02-20	23141	0.060±0.023	0.236±0.038	0.177±0.023
		60002027004	2013-10-02	25370	0.213±0.026	0.181±0.045	0.227±0.025
		60201022002	2016-09-05	155096	0.263±0.008	0.341±0.015	0.280±0.007
NGC 2110	Sy2	60061061004	2013-02-14	12019	0.028±0.008	0.028±0.011	0.073±0.007
IRAS 07378−3136	Sy2	60061351002	2014-04-20	23952	0.077±0.020	0.075±0.020	0.038±0.015
Mrk 1210	Sy2	60061078002	2012-10-05	15447	0.115±0.014	0.120±0.015	0.121±0.011
MCG +01−24−012	Sy2	60061091002	2013-04-03	12376	0.063±0.014	0.076±0.020	0.048±0.013
		60061091004	2013-04-10	9386	0.141±0.016	0.044±0.022	0.111±0.014
		60061091006	2013-04-18	12178	0.171±0.015	0.026±0.028	0.053±0.016
		60061091010	2013-05-12	15334	0.050±0.011	0.050±0.016	0.024±0.010
		60061091012	2013-05-22	12289	0.063±0.012	0.020±0.017	0.038±0.011
NGC 3079	Sy2	60061097002	2013-11-12	21542	0.126±0.054	0.131±0.029	0.125±0.026
NGC 4395	Sy2	60061322002	2013-05-10	19249	0.365±0.015	0.281±0.018	0.320±0.013
Mrk 3	Sy2	60002049004	2015-04-05	24703	0.041±0.010	0.026±0.008	0.032±0.007
		60002049010	2015-04-20	27987	0.047±0.010	0.030±0.009	0.035±0.007
ESO 121-IG028	Sy2	60061065002	2014-08-08	22049	0.102±0.025	0.164±0.024	0.095±0.018
NGC 2273	Sy2	60001064002	2014-03-23	23233	0.155±0.037	0.227±0.040	0.124±0.027
2MASX J07084326-4642494	Sy2	60160284002	2015-07-18	25681	0.109±0.020	0.229±0.041	0.169±0.020
ESO 428-G014	Sy2	60001152002	2015-01-11	40246	0.269±0.038	0.206±0.037	0.190±0.027
SDSS J0758+3923	Sy2	60001131002	2014-09-12	45132	0.264±0.014	0.238±0.024	0.256±0.012
NGC 2712	Sy2	60161342002	2017-12-03	17710	0.226±0.027	0.283±0.044	0.231±0.023

Table 3.7: Results of the analysis of variability. Column information are the same as in Table 3.1.

Name	Type	OBS ID	Date	Exposure	$F_{\rm var} \pm err(F_{\rm var})$		
					3−10 keV	10−79 keV	3−79 keV
IC 2461	Sy2	60061353002	2014-06-13	32913	0.195±0.017	0.213±0.025	0.193±0.014
2MASX J09235371-3141305	Sy2	60061339002	2014-04-19	21306	0.168±0.031	0.065±0.025	0.113±0.019
SWIFT J0926.1+6931	Sy2	60201030002	2016-06-30	45610	0.121±0.016	0.077±0.023	0.122±0.013
2MASX J09261742-8421330	Sy2	60160360002	2015-11-3	35128	0.217±0.017	0.238±0.033	0.195±0.016
NGC 3147	Sy2	60101032002	2015-12-27	49264	0.120±0.016	0.172±0.026	0.096±0.014
ESO 500-34	Sy2	60061100002	2017-12-15	18298	0.361±0.034	0.279±0.042	0.306±0.027
NGC 3281	Sy2	60061201002	2016-01-22	22986	0.117±0.027	0.175±0.021	0.156±0.017
MCG+12-10-067	Sy2	60061204002	2015-01-15	24776	0.136±0.027	0.071±0.039	0.114±0.023
MCG+06-24-008	Sy2	60061359002	2014-11-02	24108	0.172±0.023	0.135±0.037	0.102±0.020
NGC 3393	Sy2	60061205002	2013-01-28	15661	0.203±0.084	0.173±0.033	0.179±0.030
IGRJ 11366-6002	Sy2	60061213002	2014-10-29	21566	0.269±0.018	0.253±0.030	0.271±0.015
NGC 3822	Sy2	60061332002	2016-01-12	21299	0.201±0.026	0.258±0.050	0.179±0.024
2MASX J11462959+7421289	Sy2	60061214002	2013-12-10	22833	0.165±0.025	0.246±0.046	0.118±0.022
MCG 01-30-041	Sy2	60061216002	2017-06-14	26904	0.224±0.016	0.189±0.028	0.210±0.014
NGC 3998	Sy2	60201050002	2016-10-25	103936	0.044±0.010	0.134±0.017	0.059±0.009
IC 751	Sy2	60001148002	2014-11-28	26290	0.267±0.031	0.320±0.043	0.292±0.027
ESO 505-30	Sy2	60061226002	2018-01-28	21670	0.164±0.018	0.227±0.024	0.153±0.015
NGC 4258	Sy2	60101046002	2015-11-16	54785	0.131±0.015	0.184±0.024	0.079±0.013
		60101046004	2016-01-10	103616	0.104±0.013	0.195±0.020	0.102±0.011
NGC 4579	Sy2	60201051002	2016-12-06	117843	0.148±0.007	0.062±0.015	0.130±0.007
IGR J12391-1612	Sy2	60061232002	2016-01-15	21354	0.152±0.024	0.259±0.039	0.150±0.020
WKK 1263	Sy2	60160510002	2016-04-27	16373	0.034±0.008	0.061±0.014	0.022±0.007
NGC 4785	Sy2	60001143002	2014-08-20	48832	0.095±0.026	0.199±0.028	0.000±0.020
NGC 4939	Sy2	60002036002	2017-02-17	22043	0.098±0.029	0.150±0.026	0.137±0.020
NGC 4945	Sy2	60002051002	2013-02-10	45215	0.161±0.015	0.199±0.008	0.183±0.007
		60002051004	2013-06-15	54616	0.074±0.012	0.194±0.005	0.163±0.005
		60002051006	2013-07-05	34713	0.150±0.021	0.280±0.010	0.247±0.009
Mrk 248	Sy2	60061241002	2013-04-21	12901	0.033±0.019	0.017±0.025	0.036±0.017
		60061241004	2013-11-17	28909	0.040±0.013	0.016±0.018	0.065±0.011
		60061241006	2013-11-23	23056	0.127±0.015	0.115±0.022	0.107±0.014
		60363006002	2017-11-15	22053	0.063±0.013	0.099±0.020	0.061±0.011
NGC 5273	Sy2	60061350002	2014-07-14	21119	0.167±0.009	0.130±0.013	0.153±0.009
NGC 5674	Sy2	60061337002	2014-07-10	20671	0.073±0.014	0.107±0.021	0.051±0.013
Mrk 477	Sy2	60061255002	2014-05-15	18076	0.085±0.022	0.027±0.025	0.027±0.018
IRAS 13197-1627	Sy2	60101020002	2016-01-17	78501	0.254±0.013	0.244±0.011	0.248±0.008
ESO 383-18	Sy2	60261002002	2016-01-20	106583	0.121±0.007	0.114±0.008	0.096±0.005
		60061243002	2014-09-11	17343	0.088±0.019	0.102±0.020	0.078±0.014
UM 614	Sy2	60160560002	2015-03-31	18200	0.074±0.016	0.078±0.025	0.062±0.014
NGC 5899	Sy2	60061348002	2014-04-08	23880	0.124±0.016	0.163±0.021	0.111±0.013
Mrk 1498	Sy2	60160640002	2015-05-11	23697	0.053±0.011	0.021±0.014	0.034±0.009
NGC 6221	Sy2	60160651002	2016-05-23	18470	0.243±0.020	0.096±0.031	0.222±0.017
NGC 6240	Sy2	60102042004	2015-09-06	23010	0.185±0.024	0.034±0.016	0.045±0.013
2MASX J16531506+2349431	Sy2	60160654002	2018-01-19	27636	0.189±0.024	0.188±0.032	0.164±0.020

TABLE 3.8: Results of the analysis of variability. Column information are the same as in Table 3.1.

Name	Type	OBS ID	Date	Exposure	$F_{\rm var} \pm err(F_{\rm var})$		
					3−10 keV	10−79 keV	3−79 keV
NGC 6300	Sy2	60061277002	2013-02-25	17706	0.280±0.010	0.184±0.012	0.226±0.008
		60261001002	2016-01-24	20433	0.245±0.010	0.159±0.013	0.200±0.008
		60261001004	2016-08-24	23543	0.218±0.012	0.136±0.015	0.187±0.009
LEDA 3097193	Sy2	60061354002	2014-05-19	15645	0.114±0.015	0.132±0.019	0.133±0.013
2MASX J18305065+0928414	Sy2	60061285002	2015-11-15	22719	0.165±0.029	0.239±0.043	0.131±0.025
ESO 103-35	Sy2	60061288002	2013-02-24	27391	0.054±0.007	0.021±0.009	0.057±0.006
		60061288002	2013-02-24	27391	0.047±0.007	0.045±0.009	0.049±0.006
IGR J19473+4452	Sy2	60061292002	2012-11-06	18214	0.024±0.017	0.069±0.024	0.057±0.015
MCG +07−41−003	Sy2	60001083004	2013-03-01	20715	0.019±0.006	0.040±0.009	0.029±0.006
IGR J20187+4041	Sy2	60061297002	2013-12-21	20967	0.099±0.017	0.065±0.021	0.080±0.014
PKS 1916-300	Sy2	60160707002	2017-08-08	21789	0.178±0.018	0.182±0.031	0.162±0.016
2MASX J20005575-1810274	Sy2	60061295002	2016-10-25	21903	0.075±0.013	0.119±0.021	0.066±0.011
IGR J20216+4359	Sy2	60061298002	2014-10-03	21100	0.112±0.031	0.128±0.033	0.129±0.020
Mrk 915	Sy2	60002060002	2014-12-02	52980	0.086±0.008	0.116±0.014	0.073±0.007
		60002060004	2014-12-07	54253	0.168±0.011	0.153±0.015	0.141±0.009
		60002060006	2014-12-12	50684	0.233±0.013	0.263±0.018	0.224±0.011
MCG+01-57-016	Sy2	60061343002	2014-11-18	21366	0.298±0.020	0.206±0.032	0.252±0.017
3C 452	Sy2	60261004002	2017-05-01	51814	0.163±0.013	0.129±0.013	0.055±0.009
MCG 03-58-007	Sy2	60101027002	2015-12-06	137921	0.419±0.012	0.231±0.018	0.351±0.010
UGC 12348	Sy2	60001147002	2014-12-09	26708	0.182±0.017	0.186±0.031	0.176±0.015
PKS 2356−61	Sy2	60061330002	2014-08-10	23091	0.145±0.022	0.202±0.034	0.117±0.018
SWIFT J2015.2+2526	Sy2	60201032002	2017-05-27	28131	0.155±0.021	0.185±0.032	0.156±0.018

TABLE 3.9: Weighted mean variability characteristics of different classes of AGN. N1 and N2 represent the number of objects and the number of OBSIDs respectively.

Type	N1	N2	$(F_{\rm var} \pm err(F_{\rm var}))$		
			3−10 keV	10−79 keV	3−79 keV
FSRQ	11	19	0.060±0.042	0.064±0.038	0.062±0.033
BL_Lac	13	46	0.303±0.179	0.316±0.147	0.268±0.142
Sy1	74	113	0.103±0.061	0.093±0.050	0.099±0.057
Sy2	87	113	0.162±0.124	0.132±0.079	0.135±0.093
NLSy1	18	32	0.227±0.119	0.157±0.098	0.207±0.112
Blazars	24	65	0.273±0.186	0.219±0.170	0.201±0.153

TABLE 3.10: Results of the shortest flux doubling/halving time in minutes and its significance. Column information are (1) name of the source, (2) type of the source (3) OBSID, (4) flux doubling time scale and its error in minutes in the 3−10 keV band, (5) significance of the doubling time scale in the 3−10 keV band, (6) flux doubling time scale and its error in minutes in the 10−79 keV band and (7) significance of the doubling time scale in the 10−79 keV band.

Name	Type	OBSID	τ	Sig.	τ	Sig.
			(3−10 keV)		(10−79 keV)	
		(min.)		(min.)		
(1)	(2)	(3)	(4)	(5)	(6)	(7)
3C 120	Sy1	60001042002	17.36 ± 5.60	3.11	5.25 ± 2.01	3.33
MCG +07−41−003	Sy2	60001083002	16.82 ± 5.49	3.07	9.13 ± 2.63	3.56
NGC 4051	NLSy1	60001050008	6.96 ± 1.25	5.65	5.70 ± 1.48	3.91
NGC 4151	Sy1	60001111005	16.42 ± 5.78	3.08	23.53 ± 6.36	3.70
Mrk 421	BLLac	10002015001	23.40 ± 6.66	3.52	43.40 ± 13.44	3.85
		60002023006	22.32 ± 6.80	3.29	3.04 ± 1.23	3.75
		60002023022	113.64 ± 15.26	7.71	96.20 ± 26.51	3.78
		60002023025	37.08 ± 8.69	4.27	16.59 ± 4.44	3.98
		60002023027	55.84 ± 4.72	11.57	47.44 ± 8.28	5.58
		60002023031	34.13 ± 3.47	9.84	34.72 ± 9.89	3.43
		60002023033	55.96 ± 16.92	3.31	22.33 ± 6.48	3.45
		60002023035	25.11 ± 2.54	9.88	25.07 ± 5.60	4.48
3C 273	FSRQ	10002020001	20.64 ± 6.36	3.25	11.06 ± 2.45	4.52
IC 4329A	Sy1	60001045002	22.11 ± 7.27	3.05	14.12 ± 4.19	3.38
MCG −05−23−16	Sy1	60001046002	99.58 ± 23.12	4.23	3.35 ± 1.45	3.89
MCG −06−30−15	Sy1	60001047003	10.45 ± 3.18	3.30	7.89 ± 2.53	3.15
PDS 456	NLSy1	60002032002	4.94 ± 1.45	3.27	1.99 ± 0.85	3.34
IGR J21277+5656	NLSy1	60001110002	10.36 ± 2.84	3.68	32.59 ± 8.63	3.56
		60001110005	5.78 ± 1.93	3.79	51.47 ± 17.07	3.04
NGC 1068	Sy2	60002030004	17.63 ± 8.07	3.98	5.12 ± 1.72	3.02
NGC 1365	Sy2	60002046005	10.49 ± 2.45	4.32	5.36 ± 2.17	3.14
		60002046007	8.45 ± 2.16	3.94	7.70 ± 2.83	3.04
		60002046009	10.56 ± 3.16	3.35	7.76 ± 2.39	3.28
NGC 1052	Sy2	60061027002	3.53 ± 1.45	3.10	1.86 ± 1.02	3.67
NGC 4395	Sy2	60061322002	3.08 ± 0.44	7.33	4.35 ± 1.08	4.13
NGC 3227	Sy1	60202002004	25.922 ± 12.271	3.479	16.315 ± 9.671	3.728
		60202002012	32.748 ± 11.004	3.297	10.952 ± 3.576	3.025
IGRJ19378−0617	Sy1	60101003002	6.772 ± 1.463	4.693	6.116 ± 1.933	3.208
NGC 6814	Sy1	60201028002	12.457 ± 3.603	3.462	6.911 ± 2.470	3.082
MR2251−178	Sy1	60102025002	16.806 ± 5.285	3.186	9.529 ± 2.974	3.243
		60102025008	5.456 ± 0.712	7.870	4.258 ± 0.747	5.952
Ark 120	Sy1	60001044004	14.566 ± 4.581	3.187	8.862 ± 2.876	3.117
MCG+8−11−11	Sy1	60201027002	16.651 ± 5.034	3.313	10.938 ± 3.459	3.181
MCG−5−23−16	Sy1	60001046008	12.233 ± 4.422	3.083	14.719 ± 4.859	3.037
Pictor A	Sy2	60101047002	4.042 ± 1.307	3.864	1.595 ± 0.988	3.017
NGC 3998	Sy2	60201050002	3.344 ± 1.127	3.388	3.147 ± 1.155	3.020
NGC 4579	Sy2	60201051002	4.288 ± 1.682	3.171	2.451 ± 0.819	3.198
NGC 4945	Sy2	60002051002	4.724 ± 1.612	3.018	9.480 ± 2.760	3.472
ESO383-18	Sy2	60261002002	5.101 ± 1.657	3.197	16.048 ± 9.410	3.419
Mrk 915	Sy2	60002060004	6.926 ± 2.289	3.059	3.715 ± 1.280	3.199
Ark 564	NLSy1	60101031002	6.163 ± 1.344	4.008	3.462 ± 1.263	3.006

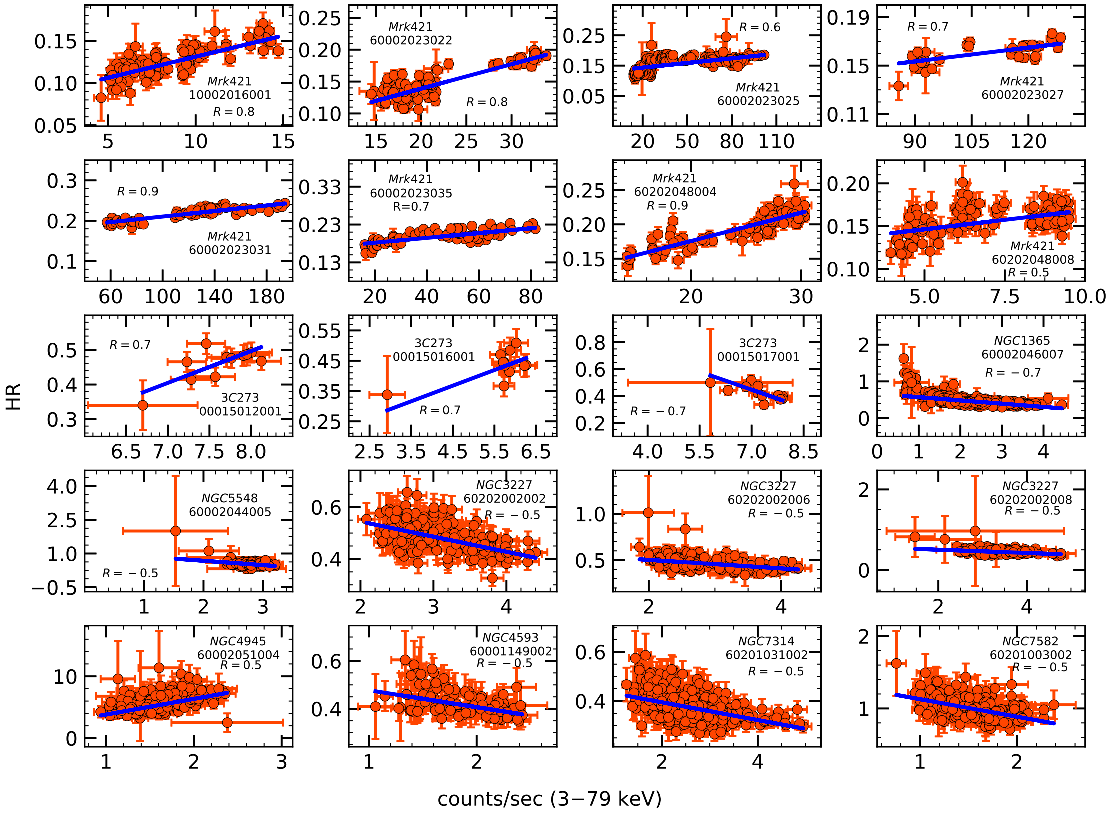

FIGURE 3.4: Correlation between HR and the count rate in the 3−79 keV band. The blue solid line is the weighted linear least squares fit to the data. Here R refers to correlation co-efficient.

3.2 Flux variability time scale

AGN in X-ray wavelengths are known to vary rapidly in the range of hours to minutes and the knowledge of these time scales is very important because it has implications on the size of the continuum-emitting region. For sources that have shown flux variations, we scanned their light curves in the energy range 3−10 keV and 10−79 keV to find the time scale of flux variations. To find the flux doubling time/halving time we used the following relation:

$$F(t) = F(t_0) \times 2^{(t-t_0)/\tau} \tag{3.5}$$

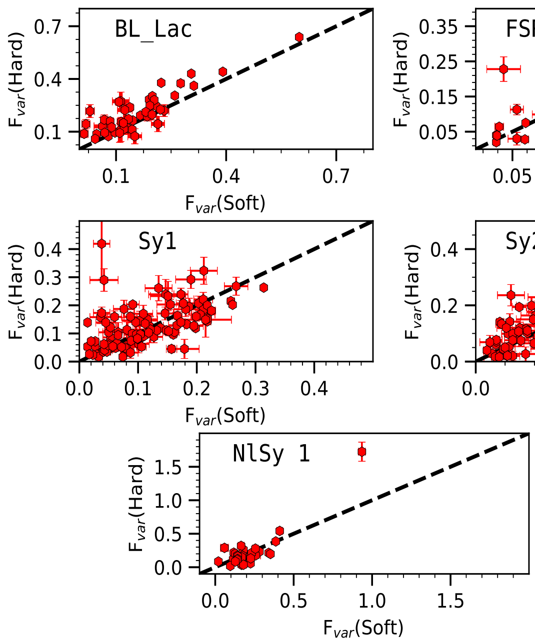

FIGURE 3.5: Correlation of flux variations between soft and hard bands for the different classes of AGN. Soft band and hard band correspond to 3−10 and 10−79 keV respectively. The dashed lines have a slope of unity and indicate identical variation of $F_{\rm var}$ values between soft and hard bands.

here, τ represents the characteristic flux doubling/halving time scale and $F(t_0)$ and $F(t)$ are values of the fluxes at time t_0 and t respectively. We calculated the flux doubling/halving time by imposing the condition that the difference between the fluxes at times t_0 and t is greater than 3σ (Foschini et al. 2011). This 3σ criteria ensures that the derived flux doubling/halving times are statistically significant. The output of this analysis obtained from Equation 5 is listed in Table 3.10. The quoted uncertainties in τ are the 1 σ errors. A total of 29 sources are found to have flux doubling/halving time scale. We noticed that all type of sources are found to have flux doubling/halving time scale. In the soft band the shortest flux doubling time of 3.08 ± 0.44 min was seen in NGC 4395, while in the hard band, the shortest flux doubling time scale was noticed in Pictor A with a value of 1.6 $\pm$ 1.0 min.

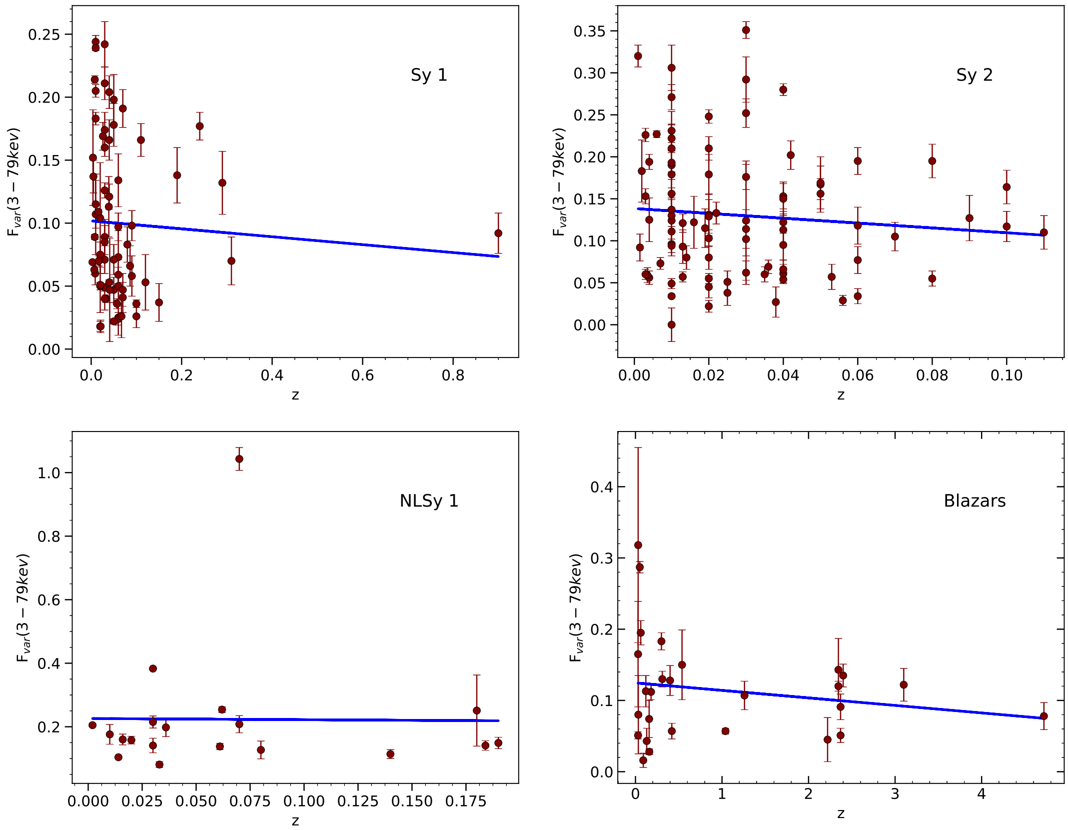

FIGURE 3.6: Correlation between $F_{\rm var}$ in the 3−79 keV band and z for different classes of AGN. Solid line is the linear least squares fit to the data.

3.3 Spectral variability

To characterise the spectral variations, we followed a model independent approach by constructing the diagrams of hardness ratio (HR) plotted as a function of total count rates in the 3−79 keV energy range. HR is estimated using the following relation

$$HR = F_{\rm hard}/F_{\rm soft} \tag{3.6}$$

where, $F_{\rm hard}$ and $F_{\rm soft}$ refers to the fluxes in the 10−79 keV and the 3−10 keV bands respectively. The HR is computed from light curves that cover a wide energy range. Therefore the disadvantage in using HR to characterize spectral

TABLE 3.11: Results of correlation analysis between HR and flux variations in the 3 − 79 keV band. The column information are as follows (1) name, (2) type of the source (3) OBSID, (4) date of observation (5) exposure time in seconds, (6) slope and error in slope, (7) intercept and error in intercept, (8) reduced χ^2, (9) probability for no correlation and (10) linear correlation coefficient.

Name	Type	OBSID	Date	Exposure	Slope	Intercept	$\chi^2_{\rm red}$	P	R
Mrk 421	BL Lac	10002016001	2012-07-08	24885	0.005 ± 0.000	0.081 ± 0.003	0.900	$< 10^{-5}$	0.8
		60002023022	2013-04-02	24772	0.003 ± 0.000	0.062 ± 0.006	3.030	$< 10^{-5}$	0.8
		60002023025	2013-04-11	57509	0.001 ± 0.000	0.133 ± 0.000	6.954	$< 10^{-5}$	0.5
		60002023027	2013-04-12	7630	0.000 ± 0.000	0.119 ± 0.000	1.984	$< 10^{-5}$	0.7
		60002023031	2013-04-14	15606	0.000 ± 0.000	0.176 ± 0.000	2.924	$< 10^{-5}$	0.9
		60002023035	2013-04-16	20279	0.001 ± 0.000	0.169 ± 0.000	3.562	$< 10^{-5}$	0.7
		60202048004	2017-01-31	21564	0.004 ± 0.000	0.093 ± 0.006	1.454	1.2×10^{-26}	0.9
		60202048008	2017-03-27	31228	0.004 ± 0.001	0.124 ± 0.006	1.281	6.8×10^{-08}	0.5
3C 273	FSRQ	00015012001	2012-07-01	2881	0.085 ± 0.034	−0.186 ± 0.262	1.193	0.010	0.7
		00015016001	2012-07-02	2990	0.049 ± 0.032	0.168 ± 0.187	0.984	0.029	0.7
		00015017001	2012-07-02	3003	−0.085 ± 0.028	1.038 ± 0.208	1.809	0.015	−0.7
NGC 1365	Sy2	60002046007	2013-01-23	73650	−0.093 ± 0.007	0.679 ± 0.018	1.890	$< 10^{-5}$	−0.7
NGC 5548	Sy1	60002044005	2013-07-23	49521	−0.192 ± 0.027	1.060 ± 0.077	1.301	$< 10^{-5}$	−0.5
NGC 3227	Sy1	60202002002	2016-11-09	49800	−0.058 ± 0.007	0.661 ± 0.021	1.086	2.9×10^{-13}	−0.5
		60202002006	2016-11-29	39689	−0.046 ± 0.007	0.594 ± 0.020	1.056	7.9×10^{-09}	−0.5
		60202002008	2016-12-01	41818	−0.040 ± 0.007	0.584 ± 0.024	0.999	1.8×10^{-10}	−0.5
NGC 4945	Sy2	60002051004	2013-06-15	54616	2.521 ± 0.242	1.310 ± 0.380	0.927	3.4×10^{-12}	0.5
NGC 4593	Sy1	60001149002	2014-12-29	23319	−0.079 ± 0.013	0.564 ± 0.025	0.786	4.4×10^{-10}	−0.6
NGC 7314	Sy2	60201031002	2016-05-13	100424	−0.036±0.003	0.467±0.009	1.088	7.02×10^{-28}	−0.5
NGC 7582	Sy1	60201003002	2016-04-28	48495	-0.242 ± 0.031	1.370 ± 0.052	0.930	1.4×10^{-11}	−0.5

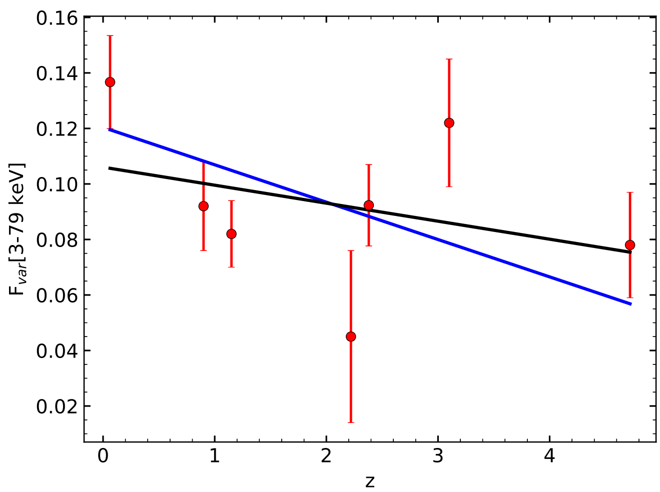

FIGURE 3.7: Correlation between $F_{\rm var}$ and z for the full sample of sources. The data are binned in redshift with a bin size of 0.47. The black and blue solid lines are respectively the weighted and unweighted linear least squares fit to the data.

TABLE 3.12: Results of statistical tests to compare the F_{var} properties of different classes of AGN. Here, Yes indicates that the null hypothesis is rejected, while No indicates the acceptance of the null hypothesis

Parameters	Mann-Whitney U test				Kolmogorov-Smirnov test			
	U_{obs}	U_{crit}	Null hypothesis	P	D	D_{crit}	Null hypothesis	P
Sy1 & Sy2 (soft band)	5035.5	5420.7	Yes	0.007	0.2034	0.1809	Yes	0.019
Sy1 & Sy2 (hard band)	5176.5	5420.7	Yes	0.014	0.1947	0.1809	Yes	0.028
Sy1 & Sy2 (full band)	4962.5	5420.7	Yes	0.004	0.2301	0.1809	Yes	0.005
BL Lac & FSRQ (soft band)	257.5	300.6	Yes	0.010	0.3707	0.3709	No	0.050
BL Lac & FSRQ (hard band)	204.0	300.6	Yes	0.008	0.4668	0.3709	Yes	0.006
BL Lac & FSRQ (full band)	227.5	300.6	Yes	0.003	0.4416	0.3709	Yes	0.011
Sy & blazars (soft band)	6974.5	6172.7	No	0.535	0.0998	0.1914	No	0.696
Sy & blazars (hard band)	5683.0	6172.7	Yes	< 0.005	0.1901	0.1914	No	< 0.052
Sy & blazars (full band)	5931.0	6172.7	Yes	< 0.018	0.1628	0.1914	No	0.138
Sy1 (hard v/s soft)	6120.0	5420.7	No	0.589	0.0708	0.1809	No	0.940
Sy2 (hard v/s soft)	6235.0	5420.7	No	0.764	0.0973	0.1809	No	0.658
BL Lac (hard v/s soft)	781.0	806.5	Yes	0.031	0.2174	0.2835	No	0.227
FSRQ (hard v/s soft)	169.0	112.9	No	0.749	0.2632	0.4412	No	0.526
NLSy1 (hard v/s soft)	445.0	365.5	No	0.373	0.1875	0.3400	No	0.627
NLSy1 & BLSy1 (soft)	821.5	1396.4	Yes	< 0.001	0.5304	0.2723	Yes	< 0.001
NLSy1 & BLSy1 (hard)	1133.0	1396.4	Yes	0.001	0.3258	0.2723	Yes	0.010
NLSy1 & BLSy1 (full band)	793.5	1396.4	Yes	< 0.001	0.4986	0.2723	Yes	< 0.001
NLSy1 & blazars (soft)	609.0	784.0	Yes	0.001	0.3981	0.2937	Yes	0.002
NLSy1 & blazars (hard)	1006.0	784.0	No	0.795	0.1356	0.2937	No	0.825
NLSy1 & blazars (full band)	758.0	784.0	Yes	0.031	0.3188	0.2937	Yes	0.026

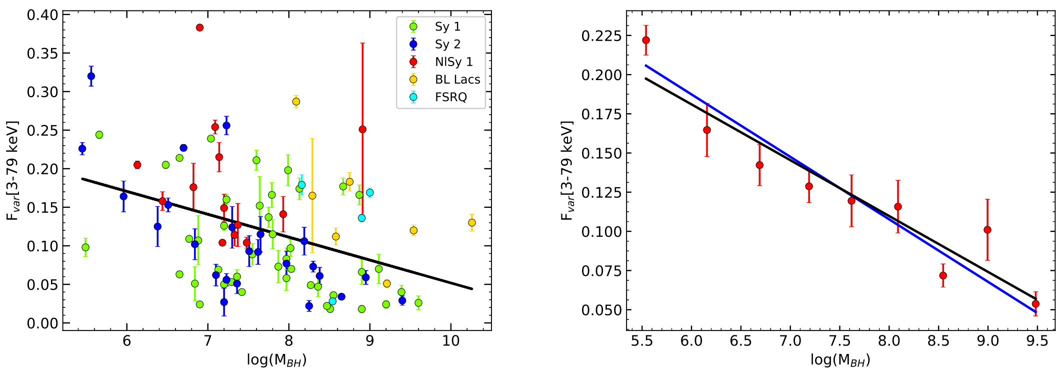

FIGURE 3.8: Left panel: F_{var} in the total band versus black hole mass. Different classes of sources are indicated in different colours. Right panel: correlation between F_{var} and black hole mass wherein the points are binned in black hole masses with a bin width of 0.477. Here, black solid line refers to the unweighted linear least squares fit, while the blue solid line is the weighted linear least squares fit.

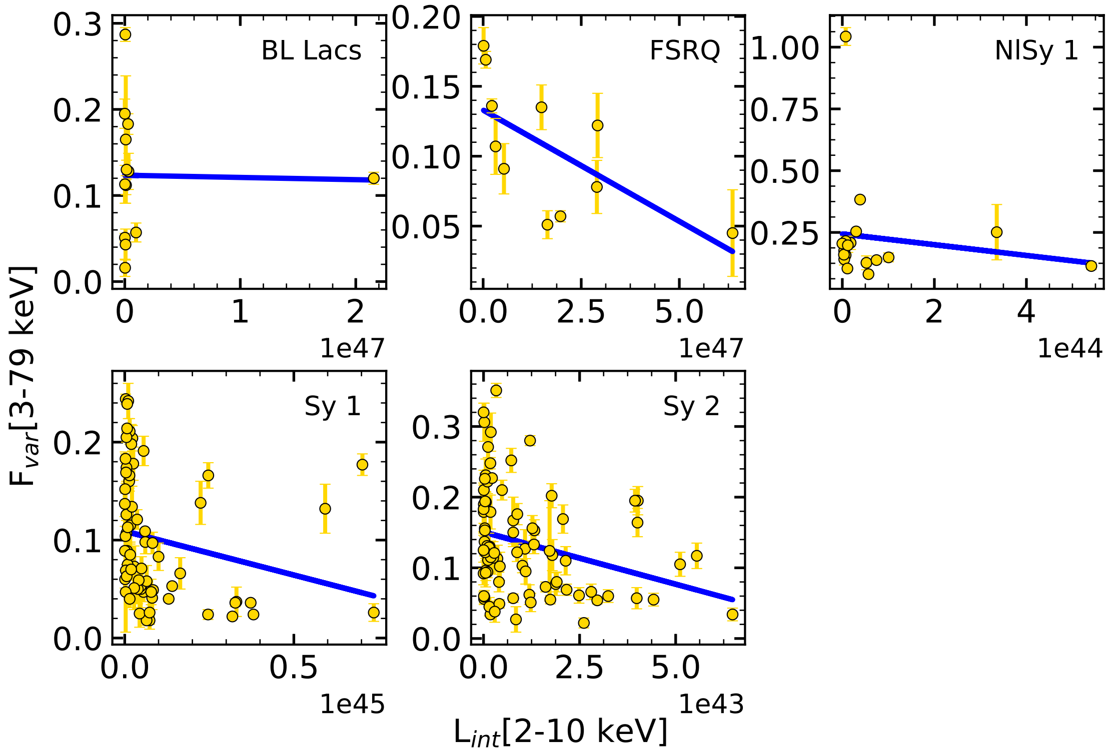

FIGURE 3.9: Correlation between $F_{\rm var}$ and the intrinsic luminosity in the 2-10 keV band for the different classes of AGN. Solid line is the unweighted linear least squares fit to the data

variations is that they do not identify spectral components that are responsible for the observed variations measured over a band, however, they are the simplest one to study spectral variations in a model independent way. As blazars are known to show spectral variations between different epochs, correlation analysis between HR and total count rates (379 keV) need to be performed individually for each epoch. The majority of sources in our sample do not show any correlation between HR and flux variations. However, some sources do show correlations between flux and spectral variations. To characterise the spectral variability, we fitted the observed points in the HR v/s flux diagram using a linear function of the form HR = a × Flux(3−79keV) + b. This fit took into account the errors in both HR and flux following Press et al. (1992). In most of the objects there were indications of spectral variations, with both "harder when brighter trend (HWB, as the source flux increases the HR also increases) and a "softer when brighter trend (SWB, as the source flux increases, the HR decreases), but those correlations are weak and insignificant. Only in nine sources we found significant spectral variations with linear correlation coefficient greater than 0.5. Of these nine sources, three sources, Mrk 421 (a BL Lac object), the FSRQ 3C 273 and NGC 4945 (a Seyfert 2 galaxy) showed a HWB behaviour and the other six sources namely the Seyfert 1 galaxies NGC 5548, NGC 3227, NGC 4593, NGC 7582 and the Seyfert 2 galaxy NGC 1365 and NGC 7314 showed a SWB trend. The colour-flux diagram, the plot of HR v/s flux for those objects are shown in Fig. 3.4. The solid line in these figures are the weighted linear least squares fit to the data. The results of the linear fits are given in Table 3.11. The SWB trend seen in NGC 5548, NGC 1365, NGC 3227, NGC 4593, NGC 7314 and NGC 7582 is similar to what is generally seen in radio-quiet AGN (Sobolewska & Papadakis 2009). In radio-quiet AGN, the hard X-ray emission is believed to be produced by Comptonization processes, where the photons from the accretion disk are Comptonized by the electrons in the hot corona. In this scenario, variations in the UV/optical photons from the accretion disk can have an effect on the slope of the output X-ray spectrum subsequently leading to a softer when brighter trend (Caballero-Garcia et al. 2012). For the BL Lac object Mrk 421 a significant harder when brighter trend is seen in 8 epochs of observations. However, for the FSRQ 3C 273, in the three epochs where a correlation between HR and total flux is found, on two epochs a harder when brighter trend is found, while, in one epoch a softer when brighter trend is noticed. Blazars in general are found to show a harder when brighter behaviour. Such hardening when brightening behaviour more often seen in the HSP category (Giommi et al. 1990; Pian et al. 1998) among other things could be due to the shift of their broad band SEDs to higher energies (Brinkmann et al. 2003). The behaviour seen in Mrk 421 here is observed before as well (Takahashi et al. 1996). The another source which has shown a HWB trend (Fig. 3.4) is NGC 4945. According to Véron-Cetty & Véron (2010) it is an "unclassified Seyfert. This source having a circumnuclear star burst (Lenc & Tingay 2009) is detected in the γ-ray band by the Large Area Telescope on board the Fermi gamma-ray space telescope (Abdo et al. 2010a). It has been argued that the dominant contribution to the observed γ-ray emission is from the AGN of NGC 4945 (Wojaczyński & Niedźwiecki 2017), and therefore points to the presence of a relativistic jet. Thus the observed HWB trend in NGC 4945 is due to the dominant jet emission in the source.

3.4 Variation between soft and hard bands

For sources that have shown flux variations, we found close correlation between flux variations in the soft and hard bands (Fig. 3.5), which could suggest of the same physical processes responsible for the flux variations in both the bands. However, for a large fraction of the sources that have shown flux variations, the values of $F_{\rm var}$ in the soft and hard bands are found to be not identical, pointing to spectral variations in the sources. The mean weighted $F_{\rm var}$ values for Seyfert 1 galaxies in the soft and hard bands are 0.103 ± 0.061 and 0.093 ± 0.050 respectively. Similarly, in the soft band Seyfert 2 galaxies have a mean $F_{\rm var}$ value of 0.162 ± 0.124, while in the hard band the mean $F_{\rm var}$ value is 0.132 ± 0.079. Thus, on average, both Seyfert 1 and Seyfert 2 galaxies do not show any difference in variability between soft and hard bands. This is confirmed by both the U-test and KS test (see Sect. 3.6). This is also evident in Fig. 3.5 where the points are distributed around the line of slope unity. The weighted mean $F_{\rm var}$ values for BL Lacs in the soft and hard bands are 0.303 ± 0.179 and 0.316 ± 0.147 respectively. U test shows that in BL Lacs, there is no difference in variability between soft and hard bands. FSRQs, too show similar flux variations in the soft and hard bands with mean $F_{\rm var}$ values of 0.060 ± 0.042 and 0.064 ± 0.038 respectively. Statistical analysis using U-test and KS test also provides no evidence of difference in variations between soft and hard bands in FSRQs. In the case of NLSy1 galaxies, we found mean $F_{\rm var}$ values of 0.227 ± 0.119 and 0.157 ± 0.098 respectively in the soft and hard bands. Though, on average NLSy1 galaxies are more variable in soft band relative to hard band, the error bars are larger to conclusively establish that NLSy1 galaxies are more variable in the soft band relative to the hard band. Also, the number of NLSy1 galaxies is small. Both U and KS tests also point to no difference in the distribution of $F_{\rm var}$ values between soft and hard bands in NLSy1 galaxies. Considering the different classes of AGN, from statistical analysis using both the U-test and KS test, we found no difference in variability between the soft and hard bands in Sefyert 1 galaxies, Seyfert 2 galaxies, FSRQs and NLSy1 galaxies. In BL Lacs, U-test indicates of difference in variability between soft and hard bands, however, KS-test points to no difference between the soft and hard band variations. The results of the statistical analysis are given in Table 3.12.

3.5 Duty cycle of flux variations

AGN do not show flux variations on each time they are observed. In our combined sample only 61% of the sources showed flux variability exceeding the measurement noise characterised by $F_{\rm var}$. Therefore to characterize the incidence of observability of flux variability at X-ray energies we have calculated the duty cycle (DC) of variability using the definition of Romero et al. (1999). DC is a measure of the fraction of time over which the objects of a given class are found to vary to the total time of observations carried out on each objects in the class. Following Romero et al. (1999) DC is given as

$$DC = \frac{\sum_{i=1}^{n} N_i (1/\Delta t_i)}{\sum_{i=1}^{n} (1/\Delta t_i)} \times 100\% \tag{3.7}$$

Here, $\Delta t_i = \Delta t_0 (1+z)^{-1}$, is the duration corrected for cosmological redshift of each of the sources observed, N_i takes the value of 1, if an object is variable during the duration of observation Δt_i and 0 otherwise. Considering all the sources analysed in this work, we found NLSy1 galaxies to show the highest DC of variability of 85%, followed by BL Lacs (67%) and then Seyfert 1 and Seyfert 2 galaxies each with DC of variability of 51%. FSRQs showed the lowest DC of variations of about 29%. The observed differences in the DC of X-ray flux variations between BL Lacs and FSRQs can be attributed to the difference in the physical processes that contribute to the observed X-ray emission in the *NuSTAR* band. Though Seyfert 2 galaxies show large amplitude flux variations than Seyfert 1 galaxies, in terms of the detectability of flux variations, both Seyfert 1 and Seyfert 2 galaxies have similar DC of variability of 51%. The results of the DC of flux variability are given in Table 3.13.

3.6 Flux variability

We found that 61% of the sources (203/335) showed flux variability. The distribution of $F_{\rm var}$ for different classes of AGN along with their cumulative distribution are shown in Fig. 3.3. For this sample, we found difference in the mean $F_{\rm var}$ values between Seyfert 1 and Seyfert 2 galaxies in the soft, hard and total bands with Seyfert 2 galaxies more variable than Seyfert 1 galaxies. For example, in the soft band, Seyfert 1 galaxies have a weighted mean $F_{\rm var}$ value of 0.103 ± 0.061, while Seyfert 2 galaxies have a weighted mean $F_{\rm var}$ value of 0.162 ± 0.124. Though on average, Seyfert 2 galaxies are more variable than Seyfert 1 galaxies, the error bars are large to conclude that Seyfert 2 galaxies are more variable than Seyfert 1 galaxies. However, to confirm if the observed differences in the mean $\rm F_{var}$ values between Seyfert 1 and Seyfert 2 galaxies are statistically significant, we carried out two non-parametric tests, namely the Mann-Whitney U test (U-test) and the Kolmogorov-Smirnov test (KS-test). The U-test tests the null hypothesis that the distribution of $\rm F_{var}$ values between different classes of AGN or between different energy bands in a particular class of AGN is identical. The null hypothesis is rejected if the evaluated U-statistics is less than the critical U-value ($\rm U_{crit}$) at some confidence level. The KS test is also similar to the U-test. Here too, the null hypothesis that is tested is that the distributions that are compared are identical. The null hypothesis is rejected if the obtained D-value is greater than the critical D-value (D_{crit}) at some confidence level. For both U and KS tests, U_{crit} and D_{crit} were evaluated at the 5% confidence level. Statistical analysis using both the U-test and KS-test reject the null hypothesis that the distribution of $F_{\rm var}$ is identical between Seyfert 1 and Seyfert 2 galaxies in the soft, hard and total bands. Our results are in agreement with that of Beckmann et al. (2007) who found that Seyfert galaxies of type 1.5 to 2 show more hard X-ray flux variations than Seyfert 1 galaxies using data from *Swift*/BAT on year like time scales. Similar, results have also been found by Soldi et al. (2014). These earlier studies point to the difference in the hard X-ray variability between Seyfert 1 and Seyfert 2 galaxies on longer time scales. However, from long term X-ray variability studies using XMM-Newton, Lanzuisi et al. (2014) found no difference in the X-ray variability characteristics between type I and type II AGN. Here our analysis on timescales of the order of minutes to hours indicates that on shorter time scales Seyfert 2 galaxies are more variable than Seyfert 1 galaxies in the soft, hard and total energy bands. As Seyfert 1 and Seyfert 2 galaxies are the same except the orientation, it is expected that they have the same X-ray variability characteristics. This is because at X-ray frequencies, the difference between Seyfert 1 and Seyfert 2 galaxies, is based on the absorption column density along our line of sight (n_H; Maiolino et al. (1998)) with Seyfert 1 galaxies having $n_H < 10^{22}$ cm^{-2} (unobscured view of the central engine) and Seyfert 2 galaxies having $n_H > 10^{22}$ cm^{-2} (obscured view of the central engine through the torus). However, we see in our combined sample Seyfert 2 galaxies showing enhanced variability relative to Seyfert 1 galaxies. Therefore, the enhanced X-ray flux variation seen in Seyfert 2 galaxies relative to Seyfert 1 galaxies might be due to a combination of variations in the central engine as well as changes in the line of sight column density. Comparing the variability properties of radio-loud sources against radio-quiet sources we found that blazars are more variable than both Seyfert 1 and Seyfert 2 galaxies in soft, hard and total bands. For example in the 10−79 keV band, the weighted mean $F_{\rm var}$ value for blazars is 0.219 $\pm$

0.170, while for Seyfert galaxies the mean $F_{\rm var}$ values are 0.093 $\pm$ 0.050 and 0.132 $\pm$ 0.079 respectively for Seyfert 1 and Seyfert 2 galaxies. According to U-test, the distributions of $F_{\rm var}$ values between blazars and Seyfert galaxies (including Seyfert 1 and Seyfert 2 galaxies) are different in the hard and total bands. This is not supported by the KS test, which could be due to the limited number of blazars. However, more observations on a larger sample of blazars are needed to establish that on short time scales, in the X-ray band, blazars are more variable than Seyfert galaxies, a conclusion arrived in this work. This enhanced variability in blazars compared to Seyfert galaxies is expected if the hard X-ray emission in blazars is dominated by the emission processes in their relativistic jets. Among blazars, BL Lacs showed more variations than FSRQs in the soft, hard and total bands. In the soft band, the mean $F_{\rm var}$ values of FSRQs and BL Lacs are 0.060$\pm$0.042 and 0.303$\pm$0.179 respectively. In the hard band, FSRQs have a mean $F_{\rm var}$ of 0.064 $\pm$ 0.038, while BL Lacs have a weighted mean $F_{\rm var}$ of 0.316 $\pm$ 0.147. Thus, BL Lacs show large amplitude variations compared to FSRQs. Both the U-test and KS-test, indicates that the distribution of $F_{\rm var}$ of FSRQs and BL Lacs are different. The difference in the X-ray flux variability characteristics between FSRQs and BL Lacs can be attributed to the different physical processes that contribute to the X-ray emission. The observed X-ray flux variations in blazars (FSRQs and BL Lacs) is due to a complicated interplay between different physical processes and timescales, which among many could involve particle acceleration, radiative cooling Doppler boosting etc. (Massaro et al. 2004). The broad band spectral energy distribution (SED) of blazars has a double hump structure. The low energy hump with its peak in the optical/IR/X-ray energies is due to synchrotron process and the high energy hump peaking at X-ray/MeV energies is due to inverse Compton process (Fossati et al. 1998; Mao et al. 2016; Abdo et al. 2010b). Based on peak of the synchrotron bump in the broad band SED, blazars are further classified as low synchrotron peaked (LSP; $\nu_{peak} < 10^14$ Hz), intermediate synchrotron peaked (ISP, $10^{15} < \nu_{peak} < 10^{14}$ Hz) and high synchrotron peaked (HSP, $\nu_{peak} > 10^{15}$ Hz) blazars (Ackermann et al. 2015). Majority of the FSRQs are LSP blazars, while most of BL Lacs fall in the HSP category. In the case of HSPs, the X-ray emission with photons up to 10 keV and occasionally up to 100 keV (Pian 2002) is dominated by synchrotron process and are produced by the more energetic electrons in the jet that represent the highest energy tail of the synchrotron radiation having the shortest cooling timescale. As the synchrotron radiation in this part of the SED is produced by the most energetic electrons, they are sensitive to variations in the acceleration and colling processes, and hence could lead to rapid and large amplitude flux variations (Pian 2002). In FSRQs, the X-ray emission is produced through IC scattering of seed synchrotron photons, by the low energy electrons in the jet, and thus dominated by synchrotron self Compton emission process. Therefore, it is expected that the flux variations in FSRQs can be less dramatic due to the longer cooling time scales of the low energy electrons that contribute to the IC processes (Gupta et al. 2016). In our sample, there are 13 BL Lacs. According to the classification in the 3FGL catalog (Ackermann et al. 2015), 11 are HSPs and two (OJ 298 and S5 0716+714) are LSPs. Similarly, there are 11 FSRQs in sample and according to Ackermann et al. (2015) 9 belong to the LSP category and two have no entry in Ackermann et al. (2015). Thus, in our sample, most/all of the FSRQs belong to the LSP category while all but two of BL Lacs belong to the HSP category. Therefore, the observed differences in the X-ray flux variability properties of BL Lacs and FSRQs, with BL Lacs having more $F_{\rm var}$ than FSRQs could be attributed to the difference in their X-ray emission processes. For NLSy1 galaxies we found mean $F_{\rm var}$ values of 0.227 ± 0.119, 0.157 ± 0.098 and 0.207 ± 0.112 in the soft, hard and total bands respectively. This is larger than the mean $F_{\rm var}$ values of Seyfert 1 and Seyfert 2 galaxies. Statistical analysis using both U-test and KS-test confirms that NLSy1 galaxies are more variable than BLSy1 galaxies in all the three energy bands. Comparing the X-ray flux variability characteristics of NLSy1 galaxies with blazars (that includes FSRQs and BL Lacs), we found NLSy1 galaxies are more variable than blazars in the soft band and total band according to both U-test and KS-test. Statistically no difference in variation between NLSy1 galaxies and blazars was found in the hard band.

3.7 Correlation of Variability with physical properties of sources

3.7.1 $F_{\rm var}$ v/s redshift

We show in Fig. 3.6 the correlation between $F_{\rm var}$ and redshift for different classes of sources such as Seyfert 1 galaxies, Seyfert 2 galaxies, NLSy1 galaxies and blazars (including both FSRQs and BL Lacs). In the same figure is shown the unweighted linear least squares fit to the data. Linear least squares fit to the data hint for the presence of weak/no anti-correlation between variability and redshift in different classes of AGN. The absence of correlation if any between $F_{\rm var}$ and z in different types of AGN could be due to the limited redshift coverage for the different types. To cover a wide z range, we combined the data for all types of AGN and binned them in redshift with a bin width of 0.47. The correlation between $F_{\rm var}$ and z in this binned data is shown in Fig. 3.7. Unweighted linear least squares fit to the data gave

$$F_{\rm var} = (-0.007 \pm 0.008)z + (0.106 \pm 0.021) \tag{3.8}$$

with a linear correlation coefficient of -0.034. Thus, AGN variability tend to show no correlation with redshift. On analysis of long time scale variability, Zheng et al. (2017) has found that for a fixed luminosity, there is a decreasing trend of variability with increasing redshift.

3.7.2 $F_{\rm var}$ v/s black hole mass

To test the correlation of variability with black hole mass ($M_{\rm BH}$), we collected from literature, the black hole masses for the objects in our sample. Out of the 335 objects in our sample, we could gather $M_{\rm BH}$ values for 92 objects. They were taken from Bentz & Katz (2015), Woo & Urry (2002) and Vasudevan & Fabian (2007). We show in Fig. 3.8 the correlation of $F_{\rm var}$ in the total band against $M_{\rm BH}$. In this plot we have considered all classes of AGN, that includes 43 Seyfert 1 galaxies, 24 Seyfert 2 galaxies, 14 NLSy1 galaxies, 4 FSRQs and 7 BL Lacs. Unweighted linear least squares fit to the data yielded

$$F_{\rm var} = (-0.044 \pm 0.001)\log(M_{\rm BH}) + (0.421 \pm 0.002) \tag{3.9}$$

A weak anti-correlation with a linear correlation coefficient (R) of -0.39 is found between $F_{\rm var}$ in the 3−79 keV band on hour like time scales and $M_{\rm BH}$ for the combined sample of Seyfert 1 galaxies, Seyfert 2 galaxies, NLSy1 galaxies, FSRQs and BL Lacs. This indicates that AGN with more massive black holes are less variable. This anti-correlation between $F_{\rm var}$ and $M_{\rm BH}$ is shown in the left panel of Fig. 3.8. We also binned the data plotted in the left panel of Fig.3.8. For this binning, we excluded the data pertaining to the source OJ 287, as it has different values of black hole mass values available in literature and it is known to be a binary black hole system (Valtonen et al. 2016) from observations of quasi periodic behaviour in their long term optical light curves (Sillanpaa et al. 1988) with a period of roughly 12 years. In the binned data shown in the right panel of Fig. 3.8 the anti-correlation between $F_{\rm var}$ and black hole mass is more vivid. From unweighted linear least squares fit to the binned data with $M_{\rm BH}$ ranging from about $10^6 - 10^{10}$ $M_\odot$, we found

$$F_{\rm var} = (-0.036 \pm 0.005)\log(M_{\rm BH}) + (0.395 \pm 0.036) \tag{3.10}$$

with a strong negative correlation coefficient of -0.94. Such inverse correlation between variability and black hole mass is known earlier as well (Ponti et al. 2012; O'Neill et al. 2005). This relation between $F_{\rm var}$ and $M_{\rm BH}$ cannot be extended to sources with black hole masses $< 10^6$ $M_\odot$. From analysis of X-ray variability of low mass AGN ($M_{BH} < 10^6 M_\odot$) it has been found by Ludlam et al. (2015) and Pan et al. (2015) that the linear relation between variability and $M_{\rm BH}$ flattens at the low black hole mass region. In this study, NLSy1 galaxies show the highest DC of variations in the hard X-ray band on hour like time scales. Also, they are found to have mean $F_{\rm var}$ larger than Seyfert 1 galaxies, Seyfert 2 galaxies and FSRQs but lower than BL Lac objects. From analysis of ASCA data, Leighly (1999) found that at any X-ray luminosity, NLSy1 galaxies have larger $F_{\rm var}$ values than broad line Seyfert galaxies which is interpreted to them having low $M_{\rm BH}$ values than Seyfert galaxies. It is possible that the large $F_{\rm var}$ values obtained for NLSy1 galaxies is due them being powered by lighter black holes. This also fits in nicely with the anti-correlation observed between $F_{\rm var}$ and $M_{\rm BH}$ (Fig. 3.8). However, spectro-polarimetric observation of a NLSy1 galaxy points to it having heavier black hole similar to blazars (Baldi et al. 2016). If this is indeed found to be true on observations on a large sample of NLSy1 galaxies, then the enhanced $F_{\rm var}$ on hour like time scales in NLSy1 galaxies relative to other classes of AGN would not be driven by the anti-correlation between $F_{\rm var}$ and $M_{\rm BH}$, however, could be caused by different processes giving rise to the X-ray flux variations.

3.7.3 $F_{\rm var}$ v/s Luminosity

The intrinsic luminosity in the $2-10$ keV band was obtained using the relation

$$L_{2-10keV} = 4\pi d_L^2 \frac{F_{2-10keV}}{(1+z)^{2-\Gamma}} \tag{3.11}$$

where $F_{2-10keV}$ is the absorption corrected flux, d_L is the luminosity distance and Γ is the photon index obtained by simple power law fit to the spectra in the $2-10$ keV band. In this calculation of the X-ray luminosity, it is assumed that the emission from the AGN is isotropic. This is not a valid assumption if the emission is beamed which is possible in the case of FSRQs and BL Lac objects. The correlation between $F_{\rm var}$ in the $3-79$ keV band and the intrinsic luminosity in the $2-10$ keV band for the various classes of AGN are shown in Fig 3.9. In this Figure, we have 13 sources for BL Lacs, 11 sources for FSRQs, 18 sources for NLSy1 galaxies, while for Seyfert 1 and Seyfert 2 galaxies we have 74 and 87 sources respectively. For this correlation analysis we have excluded two sources in Seyfert 1 galaxy sample, namely 3C 309.1 and PG 1100+772 and two sources in Seyfert 2 sample namely SDSS J0758+3923 and PKS 1916−300 as they are clearly as they are clearly outliers in the $F_{\rm var}$ v/s luminosity diagram. Unweighted linear least squares fit to the data shown as blue solid lines in Fig. 3.9 indicates a weak negative correlation between $F_{\rm var}$ and the X-ray luminosity in the 2−10 keV band indicating that brighter AGN are less variable. We also checked for the correlation between $F_{\rm var}$ and the 2−10 keV luminosity in the sample that includes Seyfert 1 galaxies, Seyfert 2 galaxies, NLSy1 galaxies, FSRQs and BL Lacs. The relation between $F_{\rm var}$ and luminosity sample with the $F_{\rm var}$ values binned in luminosity is shown in Fig. 3.10. Here, the luminosity ranges from $10^{44} - 10^{47}$ erg s^{-1}. A clear anti-correlation is evident, and unweighted linear least squares fit to the data yielded

$$F_{\rm var}(3-79keV) = (-1.08 \pm 0.466) \times 10^{-49} L_{2-10keV} + (0.108 \pm 0.009) \quad (3.12)$$

Anti-correlation between luminosity and X-ray variability has been observed earlier (Lawrence & Papadakis 1993; Barr & Mushotzky 1986; O'Neill et al. 2005; Lanzuisi et al. 2014; Nandra et al. 1997; Ponti et al. 2012). Recently, Mayers et al. (2018) has also found a negative correlation between flux variation in the 0.2−10 keV band and luminosity in the 2−10 keV band based on data from XMM-Newton. Thus the anti-correlation between variability on time scales of months and luminosity (Mayers et al. 2018) is also seen in the flux variation in the hard band on hour like time scales and luminosity.

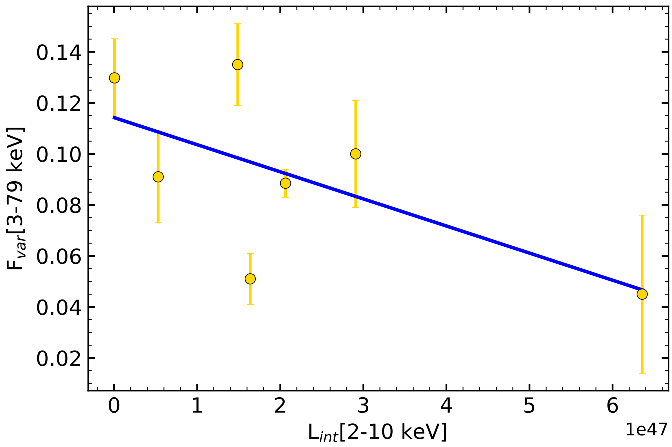

FIGURE 3.10: The plot of $F_{\rm var}$ in the total band against luminosity for the complete sample of sources that includes Seyfert 1 galaxies, Seyfert 2 galaxies, NLSy1 galaxies, FSRQs and BL Lacs. The sources are binned in luminosity with a bin width of 3.18×10^{46}. The solid line is the unweighted linear least squares fit to the data.

TABLE 3.13: Duty cycle of variability for different classes of AGN

Type	Objects	OBSIDs	DC(%)
FSRQs	24	47	29
BL Lacs	24	70	67
Sy1	121	193	51
Sy2	146	203	51
NLSy1	20	44	85
Blazars	48	117	42

3.8 Summary

To characterize the flux variability in the soft (3$-$10 keV), hard (10$-$79 keV) and total (3-$-$79 keV) X-ray band of different classes of AGN, we have carried out a systematic analysis of data from *NuSTAR* for a large sample of AGN. Key findings of this work are summarized below:

1. A total of 335 sources (24 BL Lacs, 24 FSRQs, 121 Seyfert 1 galaxies, 146

Seyfert 2 galaxies and 20 NLSy1 galaxies) over 557 sets of observations were studied in this work for hard X-ray flux variability on hour like time scales for the first time. About 60% of the sources in the sample showed X-ray flux variability.

2. In our sample, among the different categories of AGN, blazars are found to be more variable than their radio-quiet counterparts namely Seyfert 1 and Seyfert 2 galaxies. Seyfert 2 galaxies are found to be more variable than Seyfert 1 galaxies in the soft, hard and total energy bands. Within blazars, BL Lacs are found to be more variable than FSRQs. Considering the different classes of AGN, BL Lacs show high amplitude of variability, followed by NLSy1 galaxies, Seyfert 2 galaxies, Seyfert 1 galaxies and FSRQs.

3. There is no difference in variability between the soft and hard bands in Seyfert 1 galaxies, Seyfert 2 galaxies, NLSy1, FSRQs and BL Lacs.

4. Among the different classes of AGN, NLSy1 galaxies showed the highest DC of variability of about 85%. This was followed by BL Lacs with a DC of about 67%. Seyfert galaxies have a DC of ∼50% while FSRQs showed the lowest DC of variability of ∼30%.

5. When combining the different classes of AGN and binning them in $M_{\rm BH}$ and luminosity, we found a significant negative correlation between $F_{\rm var}$ and $M_{\rm BH}$ as well as $F_{\rm var}$ and luminosity in the 2−10 keV band. i.e brighter AGN are less variable, as well as AGN hosted by massive black holes are less variable. Even, when the different classes were considered separately, there is in indication of a weak anti-correlation of $F_{\rm var}$ with luminosity.

Chapter 4

Coronal properties of the Seyfert 1 galaxy 3C 120 with *NuSTAR* †

3C 120 is a X-ray bright Seyfert 1 galaxy at $z = 0.033$ (Burbidge 1967) and having a black hole mass of 5.6×10^7 $M_\odot$ (Bentz & Katz 2015). It is also classified as a broad line radio galaxy (BLRG) by Walker et al. (1987). It has a radio morphology similar to the FRI category of AGN (Fanaroff & Riley 1974). Its one sided jet has an inclination to the line of sight of $\sim 14^\circ$ (Eracleous & Halpern 1998) which is based on the apparent superluminal speed β_{app} reported by Zensus (1989). The jet is known to extend on scales up to 100 kpc (Walker et al. 1987). It has been found to be variable in X-rays. A broad Fe Kα line well fitted by a Gaussian with a σ of 0.8 keV and having an equivalent width of 400 eV has been found from ASCA observations (Halpern 1985). It has not been detected in γ-rays by the Compton Gamma Ray Observatory (CGRO,Lin et al. 1993). However, using data from the Oriented Scintillation Spectroscopy Experiment (OSSE,Johnson et al. 1993) on

†The contents of this chapter are published in
1. Rani and Stalin, 2018a, ApJ, 856, 120
2. Rani and Stalin, 2018b, JApA, 39, 15.

board CGRO, Wozniak et al. (1998) found the presence of a spectral break in 3C 120 between X-rays and soft γ-rays. 3C 120 was detected in *Fermi* using the first 15 months of data (Abdo et al. 2010c), but not detected in the second *Fermi*-LAT catalog (2FGL, Nolan et al. 2012) and the third *Fermi*-LAT catalog (3FGL, Acero et al. 2015) indicating that the source is variable in the high energy γ-rays. Using 180 and 365 days binning on the data obtained between August 2008 - December 2013, Sahakyan et al. (2015) found γ-ray flux variations. Using 5 days binned light curve Tanaka et al. (2015) noticed that 3C 120 was detected only at certain epochs. In this chapter, we focus on the broad band X-ray spectral analysis of 3C 120 using *NuSTAR*. This is the first time analysis of 3C 120 for coronal properties using *NuSTAR* data. However, from *BeppoSAX* observations, Zdziarski & Grandi (2001) have estimated a E_{cut} of 100−300 keV. Also, Wozniak et al. (1998) using the average OSSE spectrum together with ASCA data reported a E_{cut} of 130^{+150}_{-40} keV. Using data from several telescopes Lubiński et al. (2016) obtained a value of $kT_e = 176^{+24}_{-23}$ keV.

4.1 Analysis of the data

The NuSTAR spectrum of 3C 120 was generated using the procedures outlined in Chapter 2. Analysis of the spectrum along with model fittings was carried out using the *XSPEC* package. We first start the spectral analysis of 3C 120 data by fitting a phenomenological model in which we considered two absorption components, one is for our own galactic absorption and another is for the host galaxy absorption in addition to the continuum. This simple model was first fit to the data to identify the presence of more complex spectral components in the data. The considered model thus has the final form *TBabs* × *zTBabs* × *Pow*. In the fitting process, the galactic neutral hydrogen column density was fixed in *TBabs*

(Wilms et al. 2000) to the value of 1.11×10^{21} cm^{-2} obtained from Dickey & Lockman (1990) using the nH tool in HEASARC *. Column density in *zTBabs* was kept as a free parameter in the fitting and the redshift was fixed to $z = 0.033$. This gave a poor fit with a reduced $\chi^2 = 1.133$ ($\chi^2/\nu = 4299/3795$, where ν is the total degrees of freedom). The best fit model is shown in Figure 4.1 on the top along with residuals. The best fit parameters are given in Table 4.1. The residuals of the fit clearly showed the strong signature of the Fe $K\alpha$ emission line around 6.4 keV which appears because of X-ray reprocessing. There is also an indication of excess emission between 10−35 keV which could be due to Compton up-scattering of accretion disk photons in the corona. In order to improve our previous model, we replaced the continuum with an exponential high-energy cutoff power law, the *pexrav* model (Magdziarz & Zdziarski 1995) and added a redshifted Gaussian line (*zgauss*) to fit the excess emission around 6.4 keV. The inclination angle of the reflector was fixed at $\cos i = 0.95$, *i.e.*, $i \approx 17^\circ$, very close to the value of 14° found for the inclination of the jet of the source to the line of sight (Eracleous & Halpern 1998) and the abundances of elements were fixed to their solar values (Anders & Grevesse 1989). The observed spectrum with the model fit as well as the residual spectrum are shown in Figure 4.2. Model *TBabs* × *zTbabs* × *(zgauss* + *pexrav)* gave a better reduced $\chi^2 = 0.999$ ($\chi^2/\nu = 3788/3791$) than Model-1. A model that is more appropriate than pexrav is pexmon (Nandra et al. 2007). For the data sets analysed here, while using E_{cut} as a free parameter, pexmon led to unreliable values in the model parameters such as T etc. Alternatively, pexrav model fits to the data lead to convergence of the model parameters. Therefore, pexmon was not considered in all further analysis. The best fit parameters are given in Table 4.1. Using *TBabs* × *zTbabs* × *(zgauss* + *pexrav)*, We found a E_{cut} value of 83^{+10}_{-8} keV.

*https://heasarc.gsfc.nasa.gov/cgi-bin/Tools/w3nh/w3nh.pl

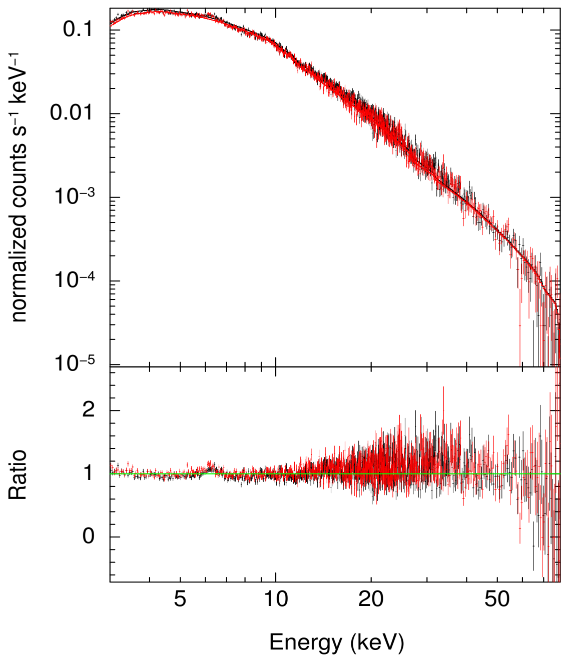

FIGURE 4.1: Normalized counts/sec versus energy for the model *tbabs* × *ztbabs* × *pow*. Here, black and red refers to FPMA and FPMB modules respectively.

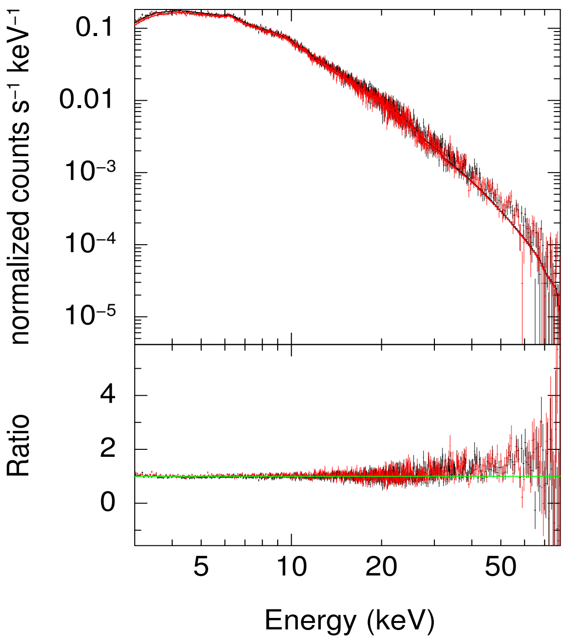

FIGURE 4.2: Normalized counts/sec versus energy for the model *tbabs* × *ztbabs* × *(zgauss + pexrav)* for the source. Here, black and red refers to FPMA and FPMB modules respectively.

4.1.1 CompTT model

We used the Comptonization model (*CompTT*; Titarchuk 1994) convolved with a reflection component so as to get the coronal parameters. This model has the form *TBabs* × *zTBabs* × *(zgauss+CompTT+refl(CompTT))*. The first component of this model *TBabs* (Wilms et al. 2000) includes galactic absorption, with the galactic neutral hydrogen column density frozen to the value of 1.11×10^{21} cm^{-2} obtained from Dickey & Lockman (1990) using the nH tool in HEASARC† and the second component *zTBabs* represents absorption intrinsic to the host galaxy of the source. Redshift was fixed to $z = 0.033$ and the column density *zTBabs* was kept as a free parameter in the fitting. The *CompTT* component in this model assumes a geometry for the corona (a slab or spherical) and models the intrinsic coronal continuum, and *refl* convolves it with reflection features (Baloković et al. 2015). For slab geometry the reduced χ^2 was 0.986 ($\chi^2/\nu = 3734/3788$) and for spherical geometry too it was 0.986 ($\chi^2/\nu = 3734/3788$). For the slab geometry, we found the mean value of $kT_e = 9^{+2}_{-3}$ keV and $\tau = 2.4^{+0.6}_{-1.1}$ considering primary and reflected emission. at the 90% confidence. For the spherical geometry the best fit yielded the mean value of $kT_e = 16^{+6}_{-7}$ keV and $\tau = 5.1^{+0.6}_{-0.4}$ for primary and reflected emission at the 90% confidence. The *CompTT* model gave huge error bars in the normalization constant. The observed spectrum along with the fit and residuals are shown in Figure 4.3 for the spherical geometry and Figure 4.4 for the slab geometry. The best fit parameters and their errors at 90% confidence levels are given in Table 4.1. The 2−10 keV flux determined from the fit is (5.19 ± 0.01) × 10^{-11} erg cm^{-2} sec^{-1}. This gives an unabsorbed luminosity of (1.29 ± 0.01) × 10^{44} erg sec^{-1}. Using the bolometric correction of 20.6 ± 0.1 found by Vasudevan & Fabian (2009) we obtained a bolometric luminosity of (26.656 ± 0.001) × 10^{44} erg sec^{-1}. For a BH mass of 5.6 × 10^7 $M_\odot$ (Bentz & Katz 2015), the calculated Eddington accretion rate is $\lambda_{Edd} = L_{bol}/L_{Edd} = 0.353$, where the Eddington luminosity,$L_{Edd} = 1.36 \times 10^{38}$ ($M_{BH}/M_\odot$) erg sec^{-1}. This is similar to

†https://heasarc.gsfc.nasa.gov/cgi-bin/Tools/w3nh/w3nh.pl

the value of $\lambda_{Edd} = 0.352$ found by Lubiński et al. (2016) using data from many telescopes including *INTEGRAL*.

4.1.2 CompPS

Though *CompTT* model well represents the observed spectrum, this has limitations such as its simplistic treatment of the seed photons that participate in the Comptonization process. We therefore fit the spectrum using one of the most advanced Comptonization models available in *XSPEC* namely *CompPS* (Poutanen & Svensson 1996). *CompPS* that produces the continuum through thermal Comptonization processes incorporates proper treatment of the Comptonization process through exact numerical solution of the radiative transfer equations. It also offers several choices for the geometries. In the fitting process, when all the parameters were kept free, the fitting failed to converge. Therefore, to avoid non-convergence owing to the presence of many free parameters in *CompPS* fitting, we fixed the centroid energy and deviation of the Fe Kα line to be 6.43 keV and 0.29 keV respectively obtained from *CompTT* for a slab geometry. The parameters obtained from the fit along with their associated errors including the Compton y parameter ($y = 4\tau\frac{KT}{m_e c^2}$, where τ is the Thomson optical depth (Zdziarski et al. 2000) and the normalization (N_{CompPS}) are given in Table 4.2. To compare our results with *CompTT*, we used *CompPS* model only for slab and spherical geometries. The seed photons were assumed to be 10 eV. The observed spectra along with the fit and residuals are shown in Figure 4.5 for the spherical and the slab geometries. For slab geometry we obtained a reduced ($\chi^2/\nu = 3773/3790$) of 0.996, whereas, for the spherical geometry the reduced ($\chi^2/\nu = 3783/3790$) was 0.998. For slab and spherical geometry, we found R values of $0.80^{+0.11}_{-0.10}$ and 0.43 ± 0.06 respectively. We found that the kT_e values obtained from *CompPS* model is larger than that obtained from *CompTT* for both spherical and slab geometries.

4.1.3 EQPAIR

The models used above to fit the *NuSTAR* data of 3C 120 assumes that the electrons involved in the Comptonization process are thermal electrons with a Maxwellian energy distribution. However, hybrid models for the corona that involves the contribution of both thermal and non-thermal electrons have been applied to AGN. For example, in NGC 4151, the contribution of non-thermal electrons is found to be less than 15% (Zdziarski et al. 1996; Johnson et al. 1997). The non-thermal fraction can also be as large as 30% (Fabian et al. 2017). 3C 120 is known to have a jet emission (Eracleous & Halpern 1998) and it is likely the observed X-ray emission is a combination of various components. We therefore model the spectrum with the *EQPAIR* model (Coppi 1999), the most advanced Comptonization model in XSPEC. This model evaluates the emission spectrum resulting from Comptonization, Coulomb collisions and pair production. This model can treat the Comptonization for a different nature of plasma (thermal, non-thermal and hybrid plasma) and even incorporates Compton hump from cold reflection. This is because in *EQPAIR*, only electrons with optical depth (τ_p) are accelerated with total power characterised by the compactness parameter l_h (such that $l_h = L_h \sigma_T / R m_e c^2$, where L_h is the luminosity or the power supplied to the electrons in the Comptonization region and R the size of the Comptonization region (Done & Gierliński 2003) that is split between thermal distribution with power (l_{th}) and non-thermal distribution with power l_{nth} and $l_h = l_{nth} + l_{th}$. These electrons then cool either through Compton scattering of soft photons or through Coulomb collisions. The parameter that plays an important role in characterising the overall spectral shape in *EQPAIR* is the parameter l_h/l_s. The soft compactness parameter (l_s) refers to the luminosity of the soft photons that is injected into the corona and the hard compactness parameter l_h refers to the power supplied to the accelerated electrons in the source. To model the observed spectrum with *EQPAIR*, we fixed the centroid energy of the Fe Kα emission line to the best fit value found from *CompTT* above for a slab geometry. However, in *EQPAIR* model the geometry is spherical and the photons are induced homogeneously throughout the spherical cloud. We assumed that the input source of soft photons in *EQPAIR* is *diskpn*, a black body spectrum (Gierliński et al. 1999) with a peak temperature of 10 eV . The seed photon distribution can be modified in the model by changing l_s which for this model fitting was fixed to 10. The inclination was fixed to 17 degrees and the iron abundance was taken to be solar. For the purpose of this modelling we considered the accelerated particles to be electrons from the thermal pool. The best fit parameters are given in Table 4.2. The observed and fitted spectra along with the residuals are given in Figure 4.5. Similar to *CompPS* and *CompTT* models, the fit of the data with *EQPAIR* model too provides a good description of the data with a reduced χ^2 of $1.047(\chi^2/\nu = 3972/3791)$. However, the temperature is not among the default output parameters returned by *EQPAIR* though it is calculated in the model. We therefore used the *chatter* command (*chatter* level = 15) (Coppi 1999) and obtained $kT_e = 23$. The error in kT_e was obtained using χ^2 minimization technique at the 90 % significance level. Thus, using the *EQPAIR* model we found $kT_e = 23^{+1}_{-7}$ keV. We found the best fit ratio of the hard to the soft compactness parameter, $l_h/l_s = 0.90 \pm 0.32$. This points to similar power in the irradiating soft photons that enter the source region and in the heating of the electrons. The *EQPAIR* model yields the value of ionization parameter of the reflector to be $\xi = 5.14 \pm 11.15$. The electron optical depth obtained by the fit was $\tau_p = 0.60 \pm 0.08$. The ratio l_{nth}/l_h, which gives the fraction of power supplied to energetic particles that goes into accelerating non-thermal particles was found to be 0.78 ± 0.10. The value of l_{nth}/l_h is zero for a purely thermal model, while it is unity for a purely non-thermal model. Though l_{nth}/l_h obtained from the fit deviates much from zero, the detection of a high energy cutoff in the *NuSTAR* spectrum not much beyond the sensitivity of *NuSTAR* (Rani & Stalin 2018a) and the non-detection of the source in $\gamma-$rays suggest that Comptonization by non-thermal electrons if any is non-significant. The χ^2 from EQPAIR model fit is poorer compared to CompPS and CompTT, though, the kT_e value from EQPAIR model fit agrees to that obtained from CompPS. Thus, it is likely that in 3C 120,

TABLE 4.1: Best fit parameters and errors (90% confidence) obtained from spectral fitting for different models.

Model Name	Parameter Name (units)	Parameter Values	χ^2/dof
TBabs*zTbabs*pow	N_H ($10^{22} cm^{-2}$)	0.33 ± 0.11	1.133
	Γ	1.85 ± 0.01	
	$N_{pow} \times 10^{-2}$	1.67 ± 0.04	
TBabs*zTbabs*(zgauss+pexrav)	E (keV)	6.45 ± 0.05	0.999
	σ (keV)	$0.15^{+0.10}_{-0.12}$	
	$N_{zgauss} \times 10^{-5}$	$3.34^{+0.76}_{-0.70}$	
	Γ	1.87 ± 0.02	
	$E_{\rm cut}$ (keV)	83^{+10}_{-8}	
	R	0.55 ± 0.07	
	$N_{pexrav} \times 10^{-2}$	1.73 ± 0.04	
CompTT			
TBabs*zTbabs*(zgauss+CompTT+refl(CompTT))	E (keV)	6.43 ± 0.06	0.986
(Spherical geometry)	σ (keV)	$0.29^{+0.10}_{-0.09}$	
	$N_{zgauss} \times 10^{-5}$	$5.50^{+1.05}_{-1.01}$	
	mean kT_e (keV)	16^{+6}_{-7}	
	mean τ	$5.1^{+0.6}_{-0.4}$	
	$N_{CompTT} \times 10^{6}$	$3.58^{+234}_{-2.99}$	
	R	0.29 ± 0.07	
	$N_{refl(CompTT)} \times 10^{-2}$	$2.82^{+2.63}_{-2.67}$	
CompTT			
TBabs*zTbabs*(zgauss+CompTT+refl(CompTT))	E (keV)	6.43 ± 0.06	0.986
(Slab geometry)	σ (keV)	$0.29^{+0.10}_{-0.09}$	
	$N_{zgauss} \times 10^{-5}$	$5.41^{+1.63}_{-1.05}$	
	mean kT_e (keV)	9^{+2}_{-3}	
	mean τ	$2.4^{+0.6}_{-1.1}$	
	$N_{CompTT} \times 10^{7}$	$1.17^{+590}_{-1.16}$	
	R	$0.30^{+0.07}_{-0.08}$	
	$N_{refl(CompTT)} \times 10^{-2}$	$2.79^{+0.25}_{-0.23}$	

for the observations analysed here, the electrons involved in the Comptonization process are predominantly thermal.

TABLE 4.2: Best fit parameters and errors (90% confidence) obtained from spectral fitting for different models. Column information are the same as in Table 4.1 .In CompPS model the parameters marked with * were fixed to the best fit values obtained from CompTT for a slab geometry. The errors in the parameters obtained from EQPAIR are the 1 σ error returned by the model fits.

Model Name	Parameter Name (units)	Parameter Values	χ^2/dof
CompPS			
TBabs*zTbabs*(zgauss+CompPS)	E (keV)	6.43*	0.996
(Slab geometry)	σ (keV)	0.29*	
	kT_e (keV)	25 ± 2	
	Compton y parameter	2.2 ± 0.1	
	R	$0.80^{+0.11}_{-0.10}$	
	ξ	$2.36\times 10^{-3}{}^{+0.237}_{-0.003}$	
	$N_{CompPS} \times 10^{+8}$	3.23 ± 0.03	
CompPS			
TBabs*zTbabs*(zgauss+CompPS)	E (keV)	6.43*	0.998
(Spherical geometry)	σ (keV)	0.29*	
	kT_e (keV)	26^{+2}_{-0}	
	Compton y parameter	$2.99^{+2.99}_{-0.18}$	
	R	0.43 ± 0.06	
	ξ	$2.13\times 10^{-3}{}^{+0.161}_{-0.002}$	
	$N_{CompPS} \times 10^{+7}$	$5.26^{+0.49}_{-0.06}$	
EQPAIR			
TBabs*zTbabs*(zgauss+EQPAIR)	l_h/l_s	0.90 ± 0.32	1.047
	l_{nt}/l_h	0.78 ± 0.10	
	kT_e (keV)	23^{+1}_{-7}	
	τ_p	0.60 ± 0.08	
	R	0.19 ± 0.03	
	ξ	5.14 ± 11.15	
	$N_{EQPAIR} \times 10^{-3}$	0.69 ± 0.03	

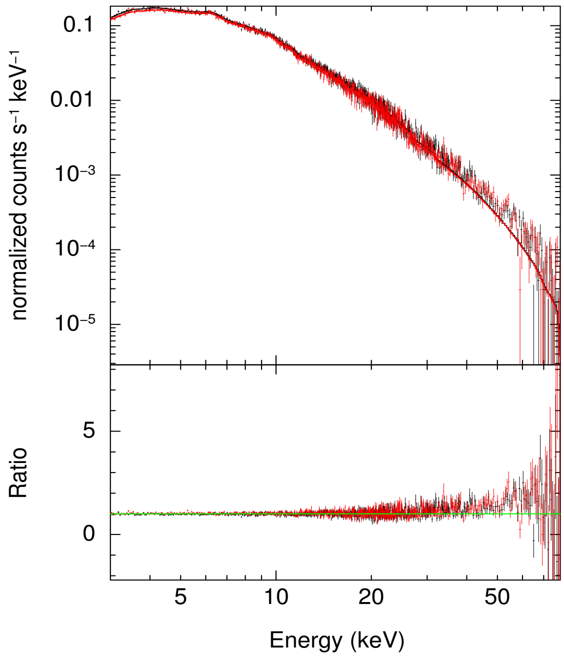

FIGURE 4.3: The figure shows the observed spectrum (Normalized counts/sec versus Energy) along with the fitted model TBabs × ZTBabs × (zgauss+compTT+refl(compTT)) (for a spherical geometry) in FPMA (black) and FPMB(red). The ratio of observations to the fitted model is also shown for FPMA (black) and FPMB (red).

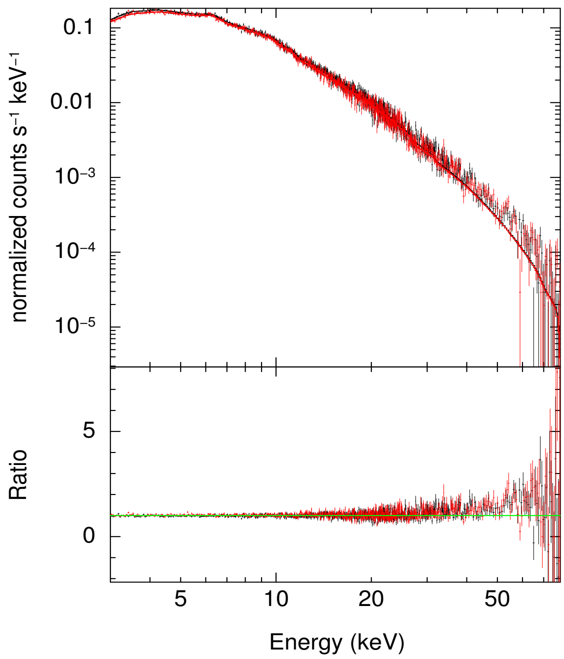

FIGURE 4.4: Same as in Figure 4.3 except for the slab geometry.

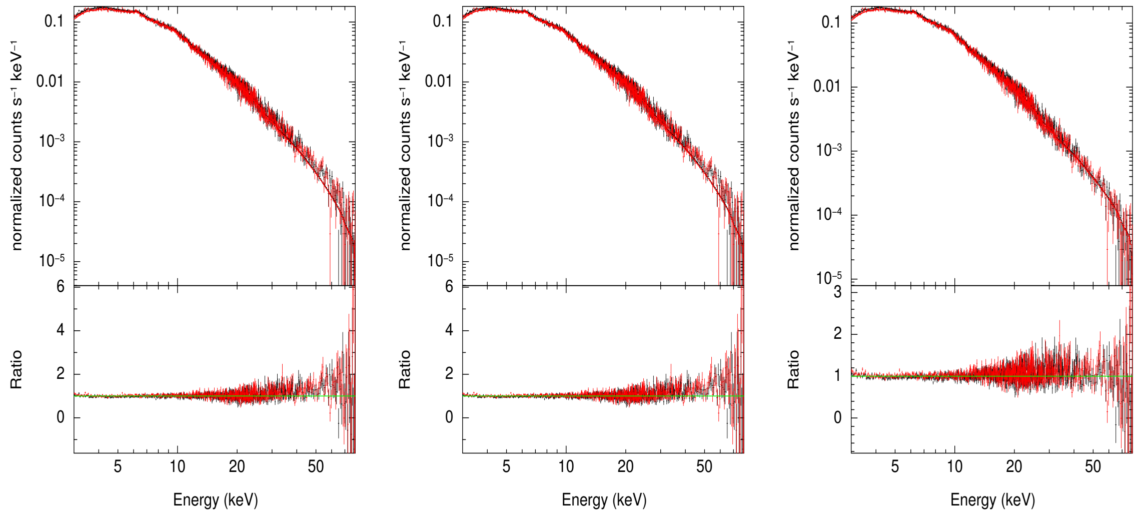

FIGURE 4.5: The left panel shows the observed spectrum (Normalized counts/sec versus Energy) along with the fitted model TBabs $\times$ zTbabs $\times$ (zgauss+compPS) (for a slab geometry) for the FPMA(black) and FPMB(red). Middle panel is same as first except for the spherical geometry. The right panel shows the observed spectrum fitted with *EQPAIR* (TBabs $\times$ zTbabs $\times$ (zgauss+EQPAIR)).

4.2 Discussion

4.2.1 Coronal properties

The availability of high quality *NuSTAR* data from observations of about 120 ks has enabled the determination of the coronal properties of 3C 120. The time averaged spectrum covering the 3−79 keV band, when fitted with the phenomenological power law model gave the continuum power law index of $\Gamma = 1.85 \pm 0.01$ (Rani & Stalin 2018a). However, values of 1.70 and 2.08 were found from XMM (Vasudevan & Fabian 2009) and INTEGRAL (Lubiński et al. 2016) observations. From *BeppoSAX* observations, Zdziarski & Grandi (2001) found the continuum to be well described by a power law with $\Gamma \sim 1.85 \pm 0.05$, which is in close agreement with what is found from *NuSTAR* data 1.87 ± 0.02 (Rani & Stalin 2018a). The difference in the photon index values obtained from different sets of observations acquired from different telescopes could point to spectral variations in the source.

Using the *pexrav* model with the inclusion of a Gaussian component to account for the presence of the Fe Kα line in the spectrum, we found values of $\Gamma = 1.87 \pm 0.02$ and $E_{cut} = 83^{+10}_{-8}$ keV. 3C 120 has been observed before by *BeppoSAX* and OSSE. By modelling the *BeppoSAX* data with an e-folded power law or a thermal Comptonization model, Zdziarski & Grandi (2001) found a value of $E_{cut} = 150^{+230}_{-30}$ keV. Using *ASCA* observation that was contemporaneous with an OSSE observation, and modelling the spectra with a broken power law multiplied by an exponential factor, Wozniak et al. (1998) found $E_{cut} = 110^{+130}_{-50}$ keV. Within error bars, the value of E_{cut} obtained from *NuSTAR* data using simple model fits matches with that known from *BeppoSAX* and OSSE data, however, has improved precision, with a manifold reduction in the errors. As these observations were taken at different epochs, it is also likely the E_{cut} is variable, but, this cannot be ascertained because of the large error bars in its values from earlier observations. The Fe Kα line is well fit by a Gaussian incorporated in *CompTT* with σ of $0.29^{+0.09}_{-0.10}$ keV and $0.29^{+0.09}_{-0.10}$ keV respectively for the slab and spherical geometry. This is much narrower than the value of $\sigma = 0.8$ keV obtained from ASCA observations (Grandi et al. 1997). In this work, we applied physical models to the data as well as simple phenomenological models. We fitted *CompTT*, to the observed spectrum and used it to characterise the temperature and optical depth of the electrons in the corona for two geometries, namely a sphere and a slab. The goodness of the fit (with a nearly identical chi-square per degree of freedom of $\chi^2/\nu \approx 3734/3788$) is found to be insensitive to the assumption of the coronal geometry as assumption of both the slab and spherical geometry fit the data equally well and we obtained $kT_e = 9^{+2}_{-3}$ keV for slab geometry and $kT_e = 16^{+6}_{-7}$ keV for the spherical geometry. These two model assumptions about the geometry of the corona gave different values of the optical depth with $\tau = 2.4^{+0.6}_{-1.1}$ and $\tau = 5.1^{+0.6}_{-0.4}$ for the slab and spherical geometry. This is expected because the optical depth for a slab geometry is measured vertically while for a sphere it is measured radially. Using *CompPS* an advanced Comptonization model available in XSPEC, we found kT_e values of 25 ± 2 and 26^{+2}_{-0} for the slab and spherical geometry. Within errors, these values of kT_e

matches with that obtained from the fit of the *EQPAIR* model to the *NuSTAR* data that returned a value of $kT_e = 23^{+1}_{-7}$ keV. This value of kT_e is much lower than the value of kT_e of 176 keV obtained by Lubiński et al. (2016). This discrepancy might be attributed to the presence of a significant jet contribution during the epoch of observations done from INTEGRAL. Considering *CompPS* model, the derived value of kT_e is nearly identical for both the slab and sphere geometry of the corona. This could mean that the shape of the X-ray spectra emerging out of these two geometries is quite similar and the available spectral data from *NuSTAR* is not sufficient to distinguish between these two geometries.

4.2.2 Nature of the corona in 3C 120

3C 120 is classified as a Seyfert 1 galaxy (Burbidge 1967) and is also identified as a BLRG by Walker et al. (1987). It has an one sided jet and is also known to be a γ-ray emitter in *Fermi* data (Sahakyan et al. 2015; Tanaka et al. 2015), which provides additional evidence for the presence of a powerful relativistic jet, already seen in radio observations (Harris et al. 2004). It is known that BLRGs have harder X-ray spectra in comparison to radio-quiet Seyfert galaxies (Zdziarski & Grandi 2001). However, spectral fits to the *NuSTAR* data analysed here using *pexrav* model gave a photon index Γ of 1.87 ± 0.02. This value is similar to that known for non-jetted Seyfert 1 galaxies and different from the X-ray spectrum of AGN with relativistic jets (blazars) that have $\Gamma < 1.5$ (Sambruna et al. 2006; Gianní et al. 2011). Though the derived X-ray spectral index points to negligible contribution of the jet emission we checked for the signature of jets in our data by looking at the multi-wavelength properties during the epoch of *NuSTAR* observations. Using the light curves taken in the optical from the Catalina Realtime Transient Survey (CRTS; Drake et al. 2009) and in the 15 GHz band in the radio from the Owens Valley Radio Observatory (OVRO, Richards et al. 2011), we found that 3C 120 was in a moderately low flux state during the time of *NuSTAR* observation analysed here. The optical and radio light curves are given in Figure 4.6 with the epoch of *NuSTAR* observations indicated as a blue dashed line. Also, during the epoch of the *NuSTAR* observations used here, the source was not detected in γ-rays by *Fermi* (Tanaka et al. 2015). The F_{var} for 3C 120 in the soft and hard bands are 0.065 $\pm$ 0.002 and 0.052 $\pm$ 0.003 respectively. This is much lower than the average F_{var} in X-rays shown by the blazar class of AGN (Soldi et al. 2014; Rani et al. 2017) Also, the variations seen in the *NuSTAR* data is similar to that of Seyfert galaxies and not blazars (Rani et al. 2017). Model fits to the observed spectrum using *CompPS* that considers thermal Comptonization gave a value of $kT_e = 26^{+2}_{-0}$ keV for a spherical geometry. On the other hand, fits to the observed spectrum using *EQPAIR* that treats Comptonization from hybrid plasma gave $kT_e = 23^{+1}_{-7}$ keV. Comparing CompTT and CompPS models for a spherical geometry using F-test we find a F-value of 1.013. The test does not rule out the null hypothesis that the two chi-square distributions are the same at the 90% confidence level. Between CompPS and EQPAIR model fits for a spherical geometry we find a F-value of 1.0637, larger than the $F_{critical}$ value for a 90% confidence, rejecting the null hypothesis that the two chi-square distributions are the same. As the chi-square value of CompPS matches close to unity compared to EQPAIR, we consider CompPS model better represents the spectrum of 3C 120. Therefore, based on both spectral (presence of X-ray high energy cut-off and the X-ray photon index being close to that known for Seyfert galaxies) and timing analysis (non-detection of the source in γ-rays during the epoch of *NuSTAR* observations), it is clear that the X-rays observed by *NuSTAR* from 3C 120 is similar to that found in non-jetted Seyfert 1 galaxies considering a model of a thermal Comptonizing corona producing the X-ray in 3C 120. We note that the strength of the reflection component obtained here showed significant differences between various model fits, which might the due to the low S/N of the data beyond 30 keV.

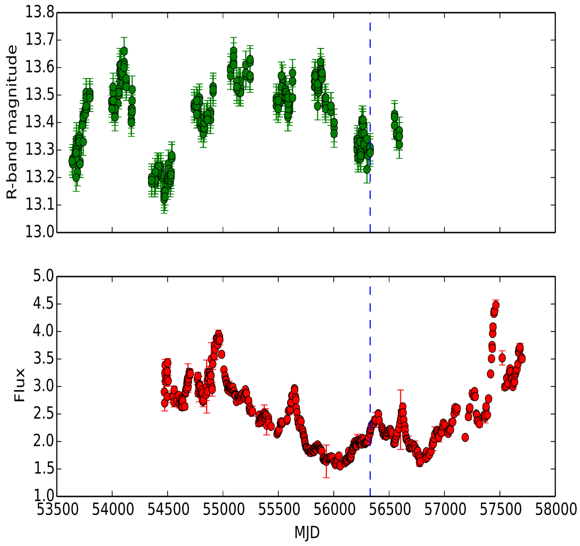

FIGURE 4.6: Long term optical V-band light curves from CRTS (top panel) and 15 GHz radio light curves from OVRO (bottom panel). The epoch of *NuSTAR* observation studied here is indicated by the blue dashed line.

4.3 Summary

We have carried out the spectral analysis of the Seyfert 1 galaxy 3C 120 using ∼120 ks observations from *NuSTAR*. The results of our analysis are summarized below:

1. $TBabs \times zTBabs \times Pow$ model provided a bad fit to the data. The residuals of the simple phenomenological model fit to the data sets of 3C 120 indicated the presence of the Fe $K\alpha$ emission line. Also, excess emission was seen beyond 10 keV which is due to Compton reflection of X-ray photons by the accretion disk.

2. Fit to the data of 3C 120, gave a value of E = 6.45 ± 0.05 keV and $\sigma = 0.15^{+0.10}_{-0.12}$ keV for the Fe $K\alpha$ line.

3. Using phenomenological model fits to the data of 3C 120, we find a high energy cut off $E_{cut} = 83^{+10}_{-8}$ keV, photon index $\Gamma = 1.87 \pm 0.02$ and a reflection fraction of R = 0.55 $\pm$ 0.07.

4. From fit of *CompTT* model to the time averaged spectrum we found evidence for the presence of weak Fe Kα line in the data at 6.4 keV with an equivalent width of 60 $\pm$ 5 eV. The line is best fit by a Gaussian with a σ of 0.29 keV.

5. Using the Comptonization model *CompPS* to fit the observed spectrum, we derived the kinetic temperature of the coronal electrons to be $kT_e = 25 \pm 2$ keV with a Compton y parameter of $y = 2.2 \pm 0.2$ for a slab geometry. This is similar to the value of the kinetic temperature of $kT_e = 26^{+2}_{-0}$ keV obtained for a spherical geometry with a y of $2.99^{+2.99}_{-0.18}$. Also, fitting the observed spectrum with *EQPAIR* gave a best fit value of $kT_e = 23^{+1}_{-7}$ keV. Thus, fits to the data with the two most advanced Comptonization models available in *XSPEC* namely *CompPS* and *EQPAIR* gave similar values of coronal temperature. It is likely that the electrons participating in the comptonization process is predominantly thermal. Comptonization by non-thermal electrons if any is in-significant as (i) the source is not detected in γ-rays during the epoch of *NuSTAR* observations and (ii) the X-ray photon index is similar to that known for Seyfert galaxies

6. 3C 120 is known to have a large scale radio jet and is also a γ-ray emitter. However, *NuSTAR* data analysed here has made possible the detection of coronal spectral signatures, constrain kT_e and the reflection features, which are found similar to that known for radio-quiet Seyfert galaxies. This indicates that the contribution of jet emission to the X-ray is negligible in the *NuSTAR* data and is likely to be weak during the epoch of *NuSTAR* observations. Additional support to this is provided by similar value of kT_e obtained by both *CompPS* and *EQPAIR* model fits to *NuSTAR* observations. This is also supported by the low/moderate radio and optical flux states as well as

non-detection by *Fermi* during the epoch of *NuSTAR* observations. To constrain the contribution of jet emission if any to the X-ray emission from 3C 120 requires observations at energies higher than that covered by *NuSTAR*.

Chapter 5

Study of AGN Coronae using *NuSTAR* †

One of the aims of this thesis is to increase the number of AGN with E_{cut} measurements and to check for correlations if any between E_{cut} values and other physical properties of the sources. Towards this we have carefully selected a sample of 12 objects, the details of which are given in Chapter 2. In Chapter 4, we have given the results obtained on one of the sources in our sample, namely 3C 120. Here we give the results of the E_{cut} measurements for other sources in the sample. In addition to this, we also present an investigation of the correlation between E_{cut} with various physical properties of the sources.

†The contents of this chapter are published in
1. Rani and Stalin, 2018b, JApA, 39, 15
2. Rani et al., 2019, MNRAS, 484, 5113.

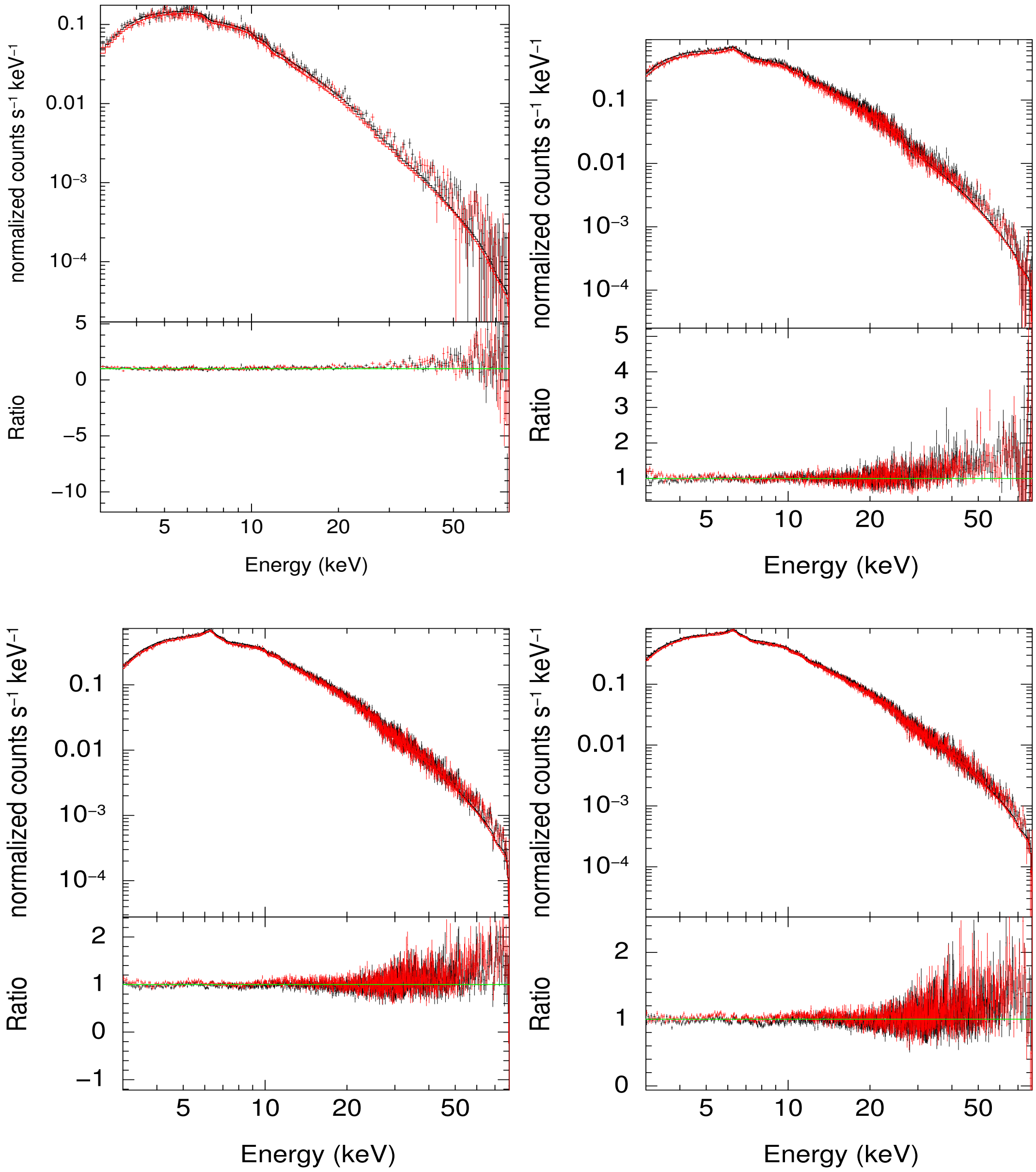

FIGURE 5.1: Observed spectra along with model fits TBabs × zTbabs × (zgauss + pexrav) and the ratio spectrum. The top panel is for the source Mrk 348 (left) and NGC 4151 for the OBSID 60001111002 (right). The bottom panel is for the sources NGC 4151 for the OBSID 60001111003 (left) and the OBSID 60001111005 (right).

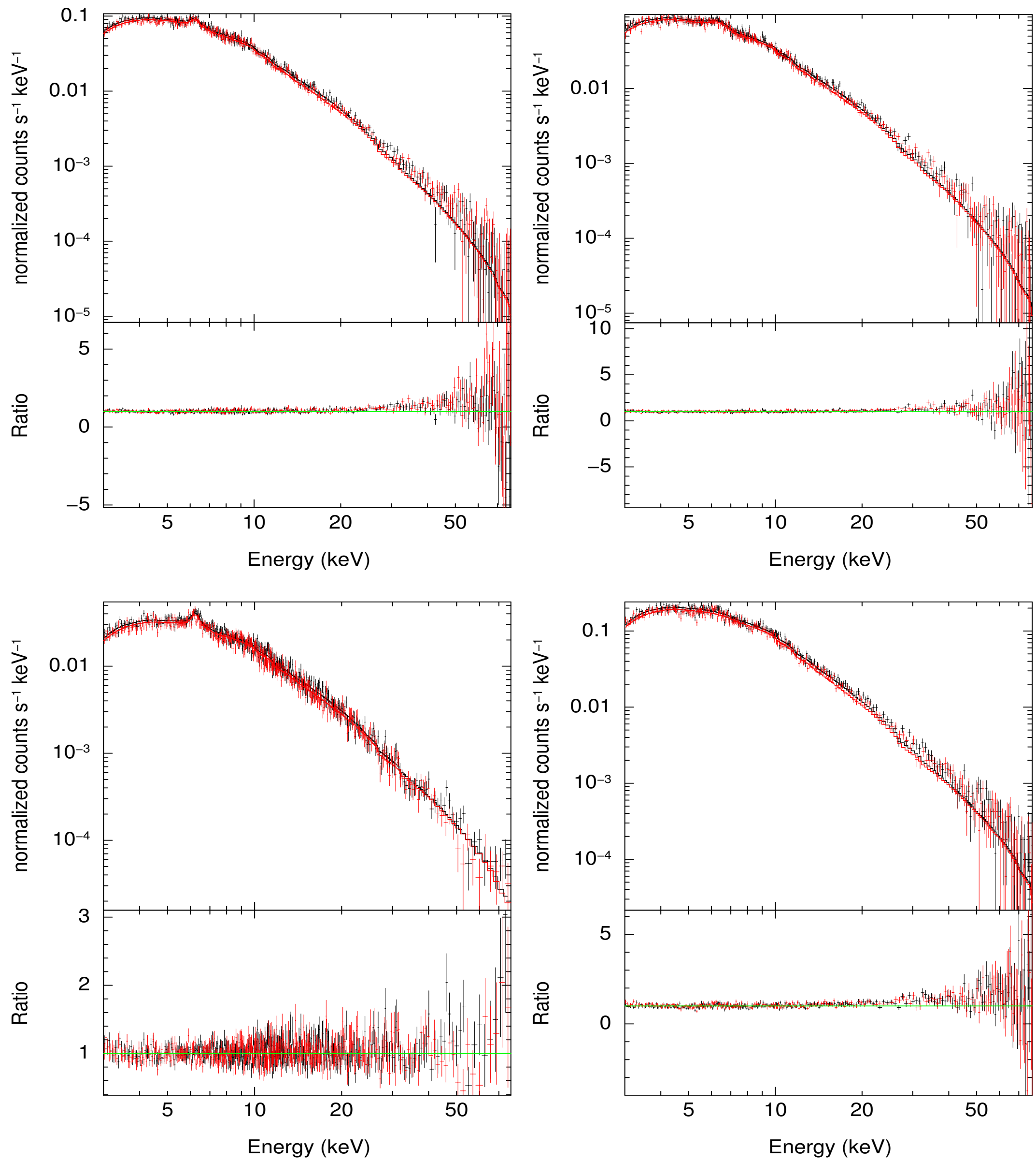

FIGURE 5.2: Observed spectra along with model fits TBabs × zTbabs × (zgauss + pexrav) and the ratio spectrum. The top panel is for the source Mrk 1040 for the OBSID 60101002002 (left) and the OBSID 60101002004 (right). The bottom panel is for the sources ESO 362−G18 (left) and NGC 2992 (right). For NGC 2992 the fitted model is TBabs × zTbabs × pexrav

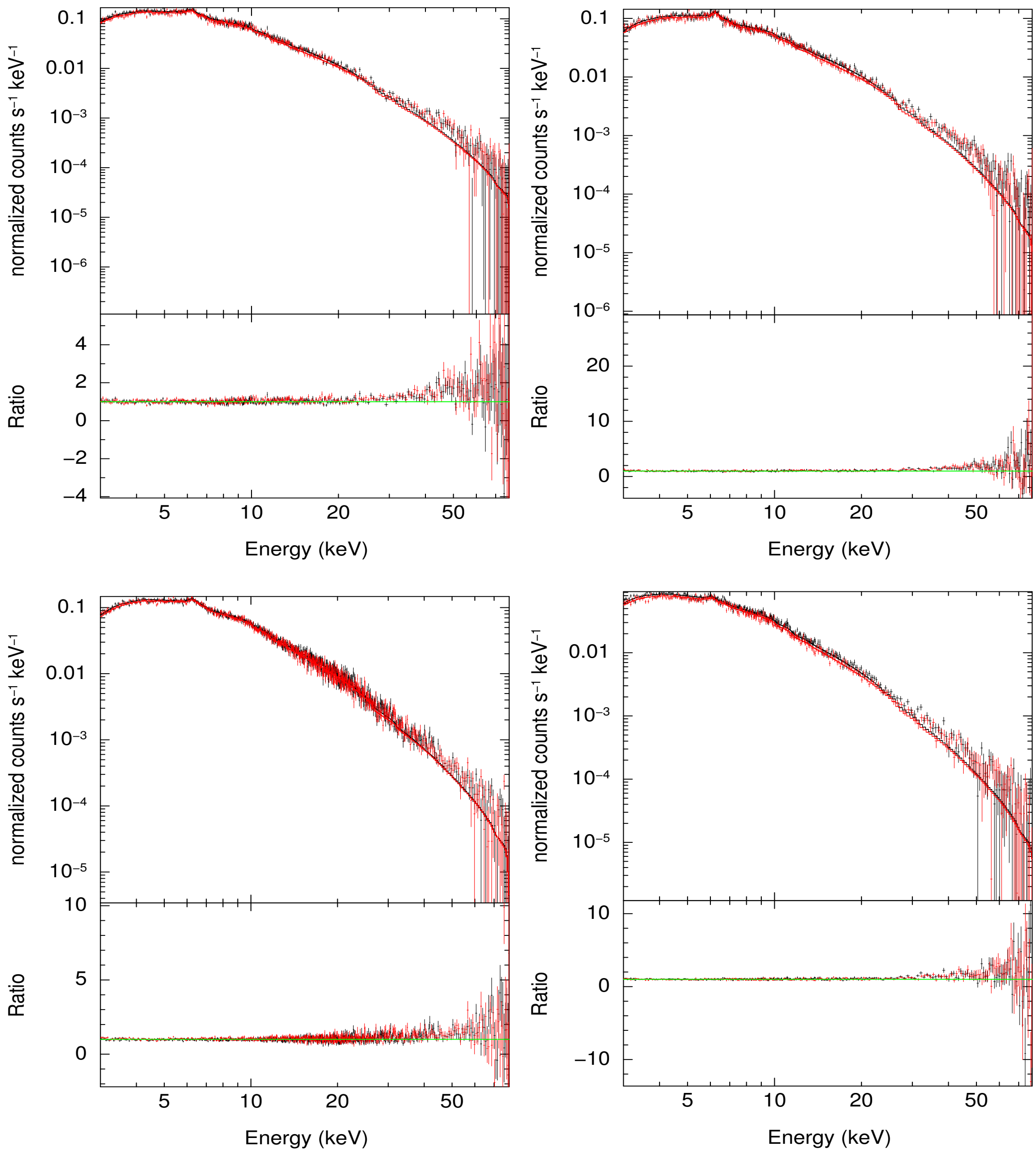

FIGURE 5.3: Normalized counts/sec versus energy for the model `TBabs` × `zTbabs` × `(zgauss+pexrav)` given for both FPMA (black) and FPMB (red) modules and the ratio plots. The top panel is for the source NGC 3783 for the OBISD 60101110002 (left) and 60101110004(right). The bottom panel is for the sources 4U 1344−60 (left) and ESO 141G055 (right).

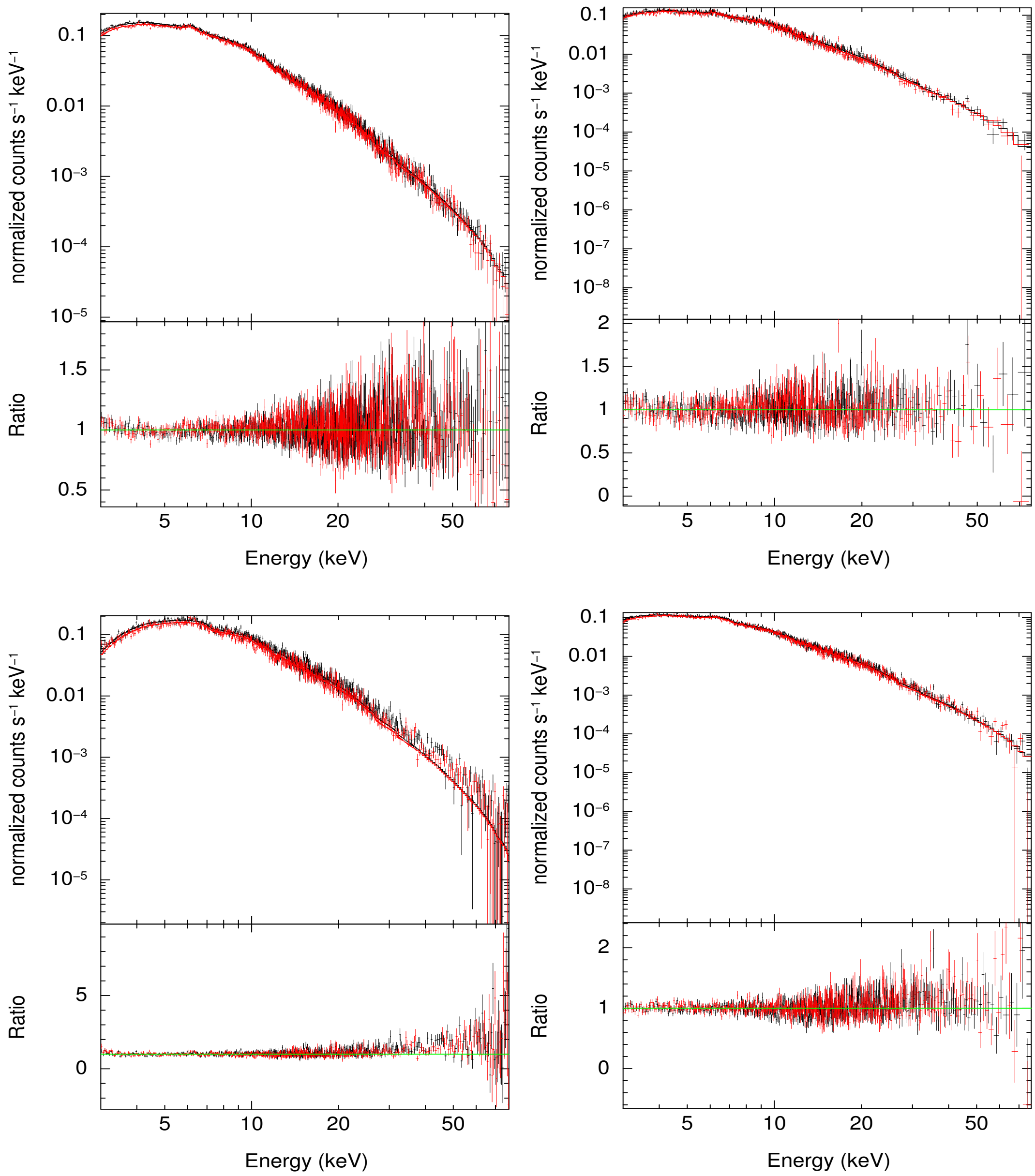

FIGURE 5.4: Observed *NuSTAR* spectra along with the model fit using the model `TBabs` × `zTbabs` × `(zgauss+pexrav)` given for both FPMA (black) and FPMB (red) modules and the ratio spectra. The top panel is for the source Mrk 509 for the OBSID 60101043002 (left) and the OBSID 60101043004 (right). The bottom panel is for the source NGC 7172 (left) and NGC 7314 (right). For the source NGC 7172 the `zgauss` component of the model was not used.

TABLE 5.1: Best fitting model parameters for the sources using the model TBabs × zTbabs × pow. Columns are (1) name, (2) OBSID, (3) galactic column density in units of 10^{20} cm^{-2} (values marked with * were fixed to the value obtained from Dickey & Lockman (1990)), (4) intrinsic column density in units of 10^{22} cm^{-2}, (5) X-ray photon index, (6) normalization factor and (7) reduced χ^2

Name	OBSID	$N_{H(TBabs)}$	$N_{H(zTBabs)}$	Γ	$N_{pow} \times 10^{-2}$	χ^2/dof
(1)	(2)	(3)	(4)	(5)	(6)	(7)
Mrk 348	60160026002	5.84*	$9.42^{+0.59}_{-0.58}$	1.74±0.02	$1.72^{+0.11}_{-0.10}$	0.67
Mrk 1040	60101002002	7.23*	1.63±0.37	1.86±0.02	1.00±0.05	0.79
	60101002004	4.11*	$1.28^{+0.40}_{-0.39}$	1.85±0.02	0.90±0.05	0.80
ESO 362−G18	60201046002	1.76*	$2.20^{+0.73}_{-0.72}$	1.57±0.02	2.31±0.13	1.25
NGC 2992	60160371002	5.26*	2.90±0.42	1.90±0.02	$2.44^{+0.14}_{-0.13}$	0.67
NGC 3783	60101110002	8.26*	2.12±0.35	1.72±0.02	1.25±0.05	0.88
	60101110004	4.11*	$3.32^{+0.41}_{-0.40}$	1.68±0.02	0.99±0.05	0.90
4U 1344−60	60201041002	1.07*	2.12±0.24	1.81±0.01	1.44±0.04	1.08
ESO141G055	60201042002	5.11*	0.70±0.33	1.88±0.02	0.87±0.04	0.91
Mrk 509	60101043002	4.11*	1.08±0.27	1.81±0.01	1.41±0.03	1.35
	60101043004	4.11*	$1.22^{+0.62}_{-0.61}$	1.77±0.02	1.19±0.06	1.13
NGC 7172	60061308002	1.65*	9.95±0.44	1.83±0.02	$2.34^{+0.11}_{-0.10}$	0.82
NGC 7314	60201031002	1.46*	0.77±0.37	1.87±0.01	1.18±0.04	1.43
NGC 4151	60001111002	2.30*	7.30±0.14	1.69±0.005	6.51±0.02	1.29
	60001111003	2.30*	10.01±0.10	1.61±0.003	5.60±0.01	1.86
	60001111005	2.30*	8.31±0.08	1.64±0.003	6.62±0.01	1.92

5.1 Model-1

We first used the simple absorbed power law model `TBabs` × `zTBabs` × `powlaw` to fit each of the AGN spectra. `TBabs` (Wilms et al. 2000) was used to model the Galactic absorption whereas `zTBabs` was used to consider the absorption due to host galaxy of the source. For this model, we used Anders & Grevesse (1989) set of solar abundances and the Balucinska-Church & McCammon (1992) photoelectric cross sections. The galactic neutral hydrogen column density was frozen to the value obtained from Dickey & Lockman (1990) for all the sources. In this model

Table 5.2: Best fitting model parameters for the sources using the model TBabs × zTbabs × (zgauss+pexrav). However, for sources, Mrk 348, NGC 2992 and NGC 7172, *zgauss* is not used. The columns are: (1) Name of the sources, (2) OBSIDs, (3) peak of the Fe Kα line in keV, (4) width of the Fe Kα line in keV, (5) photon index, (6) E_{cut} in keV, (7) reflection fraction, (8) normalization in units of 10^{-2} and (9) χ^2 per degree of freedom

Name	OBSID	E (keV)	σ (keV)	Γ	E_{cut} (keV)	R	N_{pexrav}	χ^2/dof
(1)	(2)	(3)	(4)	(5)	(6)	(7)	(8)	(9)
Mrk 348	60160026002	—	—	1.68±0.05	79^{+39}_{-19}	$0.38^{+0.26}_{-0.22}$	$1.61^{+0.12}_{-0.10}$	0.67
Mrk 1040	60101002002	$6.35^{+0.05}_{-0.05}$	$0.11^{+0.07}_{-0.11}$	1.91±0.04	99^{+39}_{-22}	$0.88^{+0.26}_{-0.23}$	$1.07^{+0.06}_{-0.05}$	0.75
	60101002004	$6.44^{+0.10}_{-0.09}$	$0.30^{+0.13}_{-0.11}$	1.94±0.04	114^{+61}_{-30}	$0.95^{+0.29}_{-0.25}$	$0.99^{+0.06}_{-0.05}$	0.76
ESO 362−G18	60201046002	$6.33^{+0.04}_{-0.04}$	$0.13^{+0.06}_{-0.07}$	$1.71^{+0.03}_{-0.05}$	>241	$0.70^{+0.26}_{-0.14}$	$0.27^{+0.01}_{-0.02}$	0.97
NGC 2992	60160371002	—	—	1.84±0.04	150^{+129}_{-65}	$0.07^{+0.23}_{-0.07}$	$2.28^{+0.13}_{-0.12}$	0.67
NGC 3783	60101110002	$6.24^{+0.05}_{-0.06}$	$0.12^{+0.08}_{-0.12}$	1.88±0.04	77^{+15}_{-11}	$1.86^{+0.37}_{-0.32}$	$1.52^{+0.09}_{-0.08}$	0.79
	60101110004	$6.30^{+0.03}_{-0.04}$	$0.00^{+0.11}_{-0.00}$	1.87±0.04	63^{+11}_{-8}	$2.46^{+0.50}_{-0.34}$	1.25±0.08	0.80
4U 1344−60	60201041002	$6.36^{+0.04}_{-0.04}$	$0.12^{+0.07}_{-0.12}$	1.95±0.03	91^{+13}_{-10}	$1.54^{+0.20}_{-0.19}$	1.71±0.06	0.92
ESO141G055	60201042002	$6.31^{+0.07}_{-0.06}$	$0.08^{+0.12}_{-0.07}$	1.94±0.04	69^{+14}_{-10}	$1.20^{+0.27}_{-0.24}$	$0.94^{+0.05}_{-0.04}$	0.86
Mrk 509	60101043002	$6.40^{+0.04}_{-0.04}$	$0.14^{+0.06}_{-0.07}$	1.83±0.02	160^{+31}_{-23}	$0.27^{+0.05}_{-0.04}$	1.46±0.04	1.10
	60101043004	$6.40^{+0.09}_{-0.06}$	$0.00^{+1.09}_{-0.00}$	1.78±0.04	143^{+72}_{-36}	$0.23^{+0.10}_{-0.09}$	$1.20^{+0.07}_{-0.06}$	1.06
NGC 7172	60061308002	—	—	1.87±0.04	69^{+14}_{-10}	$1.09^{+0.26}_{-0.23}$	$2.51^{+0.15}_{-0.14}$	0.80
NGC 7314	60201031002	$6.36^{+0.08}_{-0.09}$	$0.50^{+0.14}_{-0.10}$	2.03±0.03	—	$1.02^{+0.18}_{-0.16}$	1.40±0.05	1.05
NGC 4151	60001111002	6.26±0.05	0.19±0.06	1.66±0.03	59±4	$1.47^{+0.07}_{-0.06}$	5.16±0.2	0.94
	60001111003	6.25±0.02	0.23±0.03	1.46±0.02	64±3	$0.76^{+0.07}_{-0.06}$	3.58±0.09	1.12
	60001111005	6.26±0.02	0.20±0.004	1.51±0.02	70±3	0.74±0.06	4.60±0.1	1.12

the free parameters were the photon index Γ and the normalization. In some of the sources, we found evidence of iron Kα line and reflection component in the residuals, along with high energy turnover. The fitting results along with the galactic neutral hydrogen column density that was used and frozen during the fit are given in Table 5.1.

5.2 Model-2

We noticed turnover in the residuals obtained by fitting the model `TBabs` × `zTBabs` × `powlaw` to the data. This clearly suggested of the presence of cut-off in

TABLE 5.3: Up to date list of sources having E_{cut} measurements from *NuSTAR* and associated details. For sources that are analysed in this work and having more than one OBSID, the lowest values of E_{cut} is given in the table. The values of E_{cut},Γ, M_{BH} and λ_{Edd} quoted in this table are taken from the references given in the last column.

No.	Name	α_{2000}	δ_{2000}	z	V (mag)	Type	E_{cut} (keV)	Γ	M_{BH}	λ_{Edd}	Reference
1	Mrk 348	00:48:47.2	31:57:25.0	0.014	14.59	Sy1h	79^{39}_{19}	1.68 ± 0.05	7.2	0.149	This work
2	Mrk 1040	02:28:14.4	31:18:41.0	0.016	14.74	Sy1	99^{+39}_{-22}	1.91 ± 0.04	6.4	1.030	This work
3	3C 120	04:33:11.1	05:21:15.0	0.033	15.05	Sy1.5	83^{+10}_{-08}	1.87 ± 0.02	7.7	0.353	A
4	Ark 120	05:16:11.4	−00:09:00.0	0.033	13.92	Sy1	183^{+83}_{-43}	1.87 ± 0.02	8.2	0.085	C,J
5	ESO 362−G18	05:19:35.8	−32:39:27.0	0.013	13.37	Sy1.5	> 241	$1.71^{+0.03}_{-0.05}$	7.7	0.012	This work
6	MCG +8-11-11	05:54:53.6	46:26:21.0	0.020	14.62	Sy1.5	175^{+110}_{-50}	1.77 ± 0.04	7.2	0.754	C,H
7	NGC 2992	09:45:42.0	−14:19:35.0	0.008	13.78	Sy1.9	150^{+129}_{-65}	1.84 ± 0.04	7.7	0.029	This work
8	MCG-5-23-16	09:47:40.2	−30:56:54.0	0.008	13.69	Syi	116^{+6}_{-5}	1.85 ± 0.01	7.8	0.031	A
9	NGC 3783	11:39:01.8	−37:44:19.0	0.009	13.43	Sy1.5	63^{+11}_{-8}	1.87 ± 0.04	6.9	0.146	This work
10	NGC 4151	12:10:32.5	39:24:21.0	0.003	11.85	Sy1.5	59 ± 4.0	1.66 ± 0.02	7.6	0.100	This work,K
11	PG 1247+268	12:50:05.7	26:31:07.0	2.042	15.92	QSO	89^{+112}_{-34}	$2.35^{+0.09}_{-0.08}$	8.9	0.024	C,I
12	NGC 5273	13:42:08.3	35:39:15.0	0.003	13.12	Sy1.9	143^{-96}_{40}	$1.81^{+0.02}_{-0.03}$	6.8	1.10	A
13	4U 1344−60	13:47:36.0	−60:37:03.0	0.013	19.00	Sy1	91^{+13}_{-10}	1.95 ± 0.03	8.2	0.014	This work
14	IC 4329A	13:49:19.3	−30:18:34.0	0.016	13.66	Sy1.2	186 ± 14	1.73 ± 0.01	6.8	0.082	A
15	NGC 5506	14:13:14.8	−03:12:26.0	0.007	14.38	Sy1i	720^{+130}_{-190}	1.91 ± 0.03	8.0	0.013	A
16	GRS 1734-292	17:37:28.3	−29:08:02	0.021	21.0	Sy1	53^{+11}_{-08}	1.65 ± 0.05	8.5	0.033	A
17	3C 382	18:35:03.4	32:41:47.0	0.058	15.39	Sy1	214^{147}_{-63}	$1.68^{+0.03}_{0.02}$	9.2	0.109	A
18	ESO 103-035	18:38:20.5	−65:25:39.0	0.013	14.53	Sy2	183^{+83}_{-43}	1.87 ± 0.02	8.2	0.085	D,G
19	3C 390.3	18:42:09.0	79:46:17.0	0.056	15.38	Sy1.5	117^{+18}_{14}	1.70 ± 0.01	8.4	0.240	A
20	ESO141-G55	19:21:14.3	−58:40:13.0	0.037	13.64	Sy1.2	69^{+14}_{-10}	1.94 ± 0.04	7.5	0.370	This work
21	NGC 6814	19:42:40.7	−10:19:23	0.005	14.21	Sy1.5	155^{+70}_{-35}	$1.71^{+0.04}_{-0.03}$	7.0	0.003	C,H
22	4C 74.26	20:42:37.3	75:08:02.0	0.104	15.13	Sy1	183^{+51}_{-35}	$1.84^{+0.03}_{-0.02}$	9.6	0.037	A
23	Mrk 509	20:44:09.7	−10:43:24.0	0.035	13.12	Sy1.5	143^{+72}_{-36}	1.78 ± 0.04	7.9	0.215	This work
24	IGR 2124.7+5058	21:24:39.4	50:58:25.0	0.020	15.4 R	Sy1	80^{+11}_{-09}	1.59 ± 0.02	7.5	0.400	E,G
25	J2127.4+5654	21:27:44.9	56:56:40	0.014	18.79	Sy1n	108^{+11}_{-10}	2.08 ± 0.01	7.2	0.090	A
26	NGC 7172	22:02:01.9	−31:52:08.0	0.009	13.61	Sy2	69^{+14}_{-10}	1.87 ± 0.04	8.3	0.004	This work
27	QSO B2202-209	22:05:09.9	−01:55:18.0	1.770	17.50	QSO	153^{+103}_{-54}	1.82 ± 0.05	9.1	1.150	A
28	NGC 7314	22:35:46.1	−26:03:02.0	0.005	13.11	Sy1h		2.03 ± 0.003	5.9	0.181	This work
29	Ark 564	22:42:39.3	29:43:32.0	0.025	14.16	S3	42 ± 3	2.27 ± 0.08	6.4	1.100	A
30	NGC 7469	23:03:15.6	08:42:26.0	0.017	13.04	Sy1.5	170^{+60}_{-40}	1.78 ± 0.02	7.0	0.300	F

A:Rani & Stalin (2018b); B: Rani & Stalin (2018a), C: Tortosa et al. (2018b); D: Vasudevan & Fabian (2009), E:Tazaki et al. (2010), F: Middei et al. (2018) G: Buisson et al. (2018), H:Tortosa et al. (2018b), I:Lanzuisi et al. (2016), J:Porquet et al. (2018),K:Woo & Urry (2002) the spectrum. Also, in the residual spectra of simple power law model (model-1) fits to the data there were indications of the presence of the fluorescent Fe Kα line. This line is present in the X-ray spectra of most of the AGN (Mushotzky et al. 1993), consisting of both broad and narrow components. Therefore, Fe Kα component was included in the spectral analysis of the sources analysed here. From model-1 fits, we found that for three sources namely Mrk 348, NGC 2992 and NGC 7172, the Fe Kα line was not visibly present in their observed spectra. Therefore, for those three sources, while fitting model-2, the Gaussian component to model the Fe Kα line was not used, while it was used in the other 8 sources. The parameters of the component that were extracted from the spectral analysis are the peak energy of the line, the width of the line and the normalization. Also, in the observed hard X-ray emission of AGN, both E_{cut} and reflection are believed to play an important role. Therefore to obtain E_{cut}, we replaced the `powerlaw` in model-1 with the `Pexrav` component and refitted each AGN spectra. `Pexrav` (Magdziarz & Zdziarski 1995) includes both primary emission in the form of a power law with an exponential cut-off and the reflection component, wherein it calculates the spectrum of the X-ray source on reflection from an optically thick neutral slab. In this model, the output parameter R, gives a measure of the reflection component present in the observed spectrum. If the source is isotropic, R is related to the solid angle as $R \sim \Omega/2\pi$ and this value of R depends on the angle of inclination i between the perpendicular to the accretion disk and the line of sight to the observer. During the spectral fitting, we used the default value of the inclination angle of $i = 45°$ and abundances present in the model. As i is fixed to the default value for all the fitting, the values of R derived from the fit only gives an indication of the amplitude of reflection. The nH values for the `zTBabs` component of the model was frozen to the value obtained from model-1. The components that were left free during this model fit were E_{cut}, peak of the Fe Kα line, standard deviation of the Fe Kα line, reflection parameter and normalization for both `zguass` and `pexrav` components of the model. The model fit along with the residual spectrum are shown in Figure 5.1 $-$ 5.4 and fitting results are given in

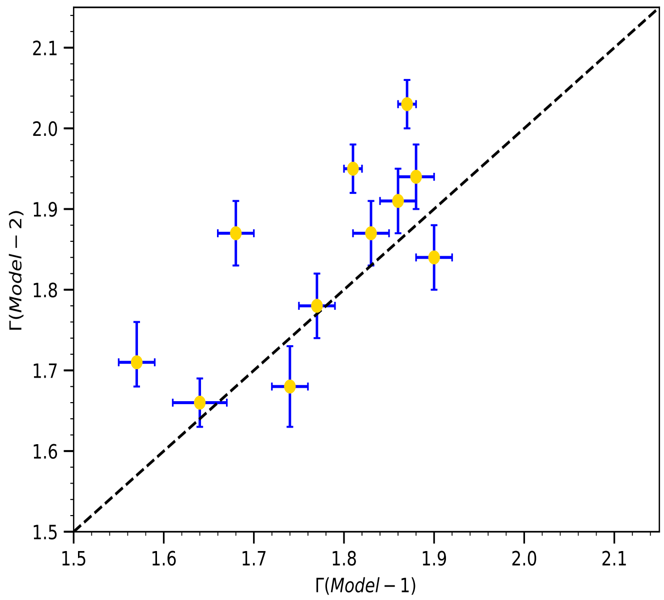

FIGURE 5.5: Γ obtained from model-1 against Γ obtained from model-2

Table 5.2. In three out of the eleven sources analysed here, namely, Mrk 348, NGC 2992 and NGC 7172 Fe Kα line is not seen. In the standard model of AGN, broad Fe Kα line is expected to be ubiquitously present in spectra of AGN, however, there are exceptions (Bhayani & Nandra 2011). The apparent non-detection of Fe Kα line in the spectra of AGN could be due to them viewed at large angles to the line of sight to the observer subsequently leading to weaker reflection (Bhayani & Nandra 2011), low signal-to-noise ratio (S/N) spectra, very high ionised accretion disk (Ross & Fabian 1993; Zycki & Czerny 1994) or a combination of the above. All the three sources for which Fe Kα line is not seen here are viewed at larger angles having classification of Sy1h, Sy1.9 and Sy2 in the Véron-Cetty & Véron (2010) catalog respectively. Thus, the apparent lack of Fe Kα line in them could be due to weaker reflection owing to larger viewing angle, however, more detailed spectral analysis is needed to clearly pin point the causes for the absence of Fe Kα line in these sources. As the aim of this work is to find E_{cut}, detailed spectral analysis of the sources are not attempted here.

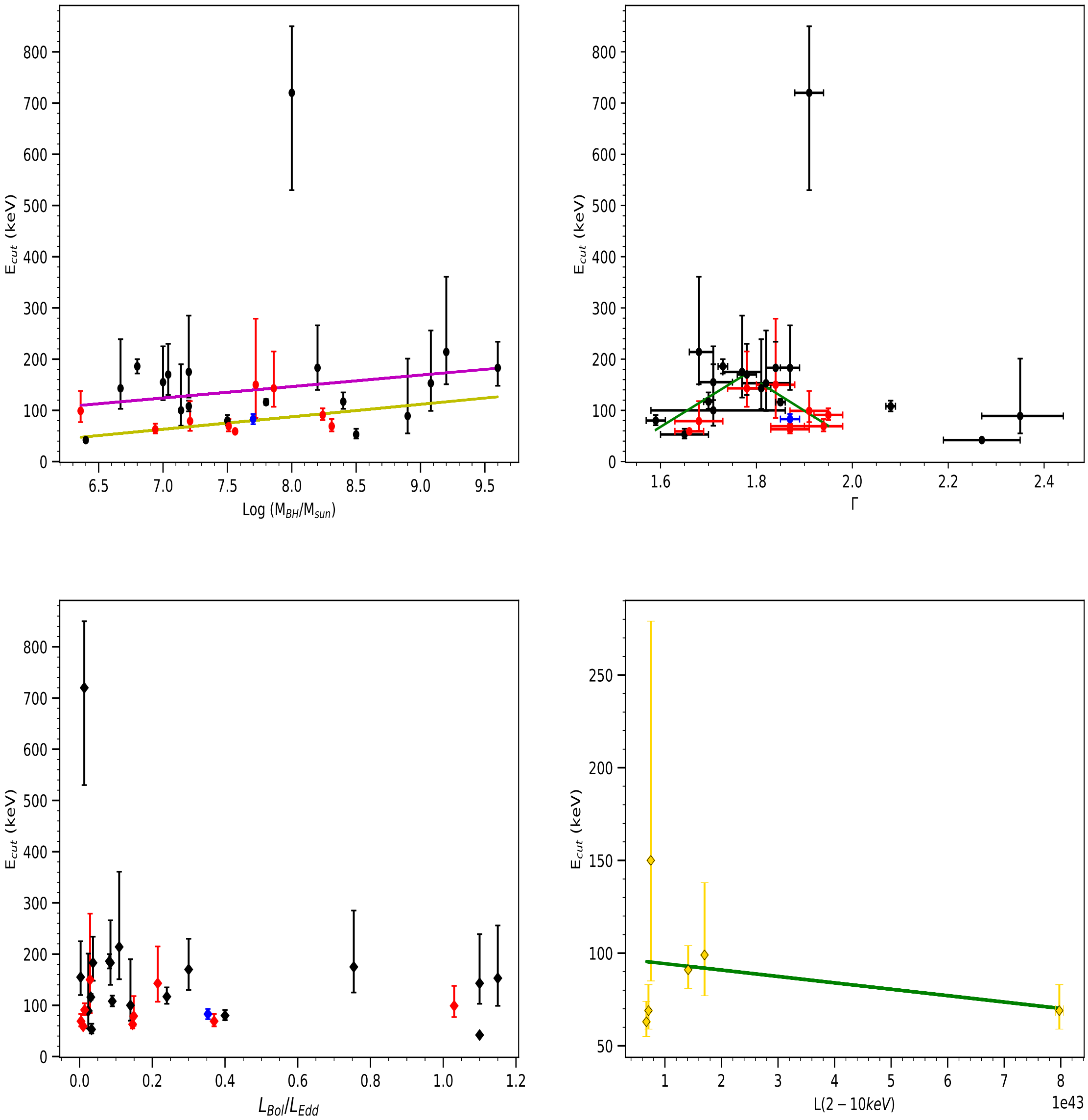

FIGURE 5.6: Correlation between E_{cut} and M_{BH} (top-left panel), E_{cut} and Γ (top-right panel), E_{cut} and λ_{Edd} (bottom-left panel) and E_{cut} vs luminosity in the 2−10 keV band for sources with $1.78 < \Gamma < 2.0$ (bottom-right panel). The red points belong to the sources analysed in this work, the two blue points are from our earlier work on two sources 3C 120 and NGC 4151, while the black points are for the sources collected from literature. The green lines in the top-right panel are the unweighted linear least squares fit to sources with $\Gamma < 1.78$ and $1.78 < \Gamma < 2.0$ respectively.

5.3 Model-3

While the fits to the spectra using the model `TBabs × zTbabs × (zgauss+pexrav)` is acceptable, we replaced the Gaussian component in Model-2 with the relativistic line emission model `RELLINE` (Dauser et al. 2010) and refit the spectra. The parameters obtained using `RELLINE` model are similar to that obtained using `TBabs × zTbabs × (zgauss+pexrav)` model. There is negligible improvement in the parameters obtained with Model-2 suggesting little/no blurring. Hence, in all further discussions we consider the parameters obtained by the model `TBbs × zTbabs × (zgauss+pexrav)`.

5.4 Reflection parameter

All the 11 sources studied in this work are Seyfert galaxies, however based on Véron-Cetty & Véron (2010) they have varied classifications such as Sy1, Sy1.2, Sy1.5, Sy1.9, Sy1h and Sy2. Clubbing all sources with classifications up to Sy1.5 as Sy1 galaxies, sources beyond Sy1.5 as Seyfert 2 galaxies and Sy1h as Sy2 galaxies, we found four Seyfert 2 galaxies and seven Seyfert 1 galaxies The unweighted mean value of R for the Seyfert 2 galaxies in our sample is 0.58 ± 0.51, while that for the Seyfert 1 galaxy sample, we obtained an unweighted mean value of 1.05 ± 0.66. Given the large error bars, both Sy1 and Sy2 galaxies have similar mean R value, however, this large error bar is attributable to the small number statistics. Given this limitation, the mean value of R for Seyfert 2 galaxies points to have a lower value compared to the mean R value of Seyfert 1 galaxies. The decrease of reflection in Seyfert 2 relative to Seyfert 1 galaxies would be in agreement with the Unification scenario (Urry & Padovani 1995). Reprocessing in AGN is from the accretion disk and for Seyfert 1 galaxies that are observed pole on, we are able to see more of the reprocessed radiation, while in Seyfert 2 galaxies that are observed edge on, the reprocessed component is expected to be less. From an analysis of Swift/BAT spectra for a large sample of AGN, Ricci et al. (2017) found obscured sources to have less values of R compared to their counterparts that are seen pole on.Thus our results on R, though suffer from small number statistics are in agreement with that found by Ricci et al. (2017) from an analysis of the spectra taken from Swift/BAT for a larger number of sources. However, from an analysis of the stacked Swift/BAT spectra, Vasudevan et al. (2013b) found that obscured sources have more reflection component than their unobscured counterparts. The origin of this difference between the values obtained from spectral analysis of individual sources and analysis of the stacked spectra of different categories of sources is not clear.

5.5 Photon index

The photon indices obtained by both the model fits ranged between 1.57 to 2.03. Comparing the photon indices obtained from both the model fits, we noticed that the Γ obtained by model-1 (a simple power law fit) is flatter than the Γ obtained from model-2 for all the sources except 2, namely Mrk 348 and NGC 2992. The steeper Γ obtained from model-2 is also consistent with the observations of the presence of high energy cut-off in most of the AGN. Unweighted mean values obtained from both model-1 and model-2 are 1.77 $\pm$ 0.12 and 1.86 $\pm$ 0.10 respectively. The plot of the Γ obtained from model-1 against Γ obtained from model-2 is shown in Fig. 5.5. Also, shown in the same figure is a line of unity slope. It is very clear from the Figure, that the Γ from model-2 is steeper than the Γ obtained from model-1.

5.6 Cut-off energy

Of the 11 sources analysed here, we obtained E_{cut} for 9 sources, for one source a lower limit is obtained while for one source, we could not constrain E_{cut}. For sources for which we were able to obtain E_{cut}, the obtained values range between 160 keV < E_{cut} < 59 keV. For 5 sources in our sample, the obtained E_{cut} values were less than 80 keV and is within the energy range for which *NuSTAR* is sensitive. For our sample of 9 sources, we found a mean E_{cut} value of 91 keV with a standard deviation of 32 keV. This is lower than that obtained by Malizia et al. (2014), who on analysis of 41 AGN found a mean E_{cut} value of 128 keV and a standard deviation of 46 keV. This comparison needs to be taken with caution as changes in the E_{cut} values, that reflect coronal temperature variations are also noticed for sources when observed at different times (Zoghbi et al. 2017; Zhang et al. 2018).

5.7 Correlation of E_{cut} with other parameters

In this chapter, we have reported the results of our analysis on the spectra of 11 AGN. By modelling the observed X-ray spectra of 11 AGN using data from *NuSTAR* using an empirical description of the observations as a power law with an exponential cut-off, we were able to derive Γ for 11 sources. Out of the 11 sources, we could obtain E_{cut} for 9 sources, and a lower limit for one source. Using these new measurements along with data for other sources culled from literature that has *NuSTAR* measurements, we could collect data for a total of 30 sources (Table 5.3). The Γ values for this enlarged complete sample, range from 1.6 to 2.4, while the E_{cut} take values lesser then 250 keV, except for one sources namely NGC 5506 having a value of $E_{cut} = 720^{+130}_{-190}$. This range of E_{cut} from *NuSTAR* also lies in the range of E_{cut} values obtained from non-focussing instruments such as BeppoSAX and INTEGRAL. However, the values of E_{cut} from *NuSTAR* have low errors compared to the values obtained from earlier missions operating in the energy range similar to *NuSTAR*. This is likely due to the high sensitivity of *NuSTAR* compared to earlier missions. For these 30 sources with quality E_{cut} measurements from *NusTAR*, we tried to look for correlation if any between E_{cut} and various properties of the sources, such as Γ, BH mass and Eddington ratio. We obtained a complicated pattern between E_{cut} and Γ. This is shown in Fig. 5.6. For sources with Γ less than 1.78, we found a positive correlation (correlation coefficient = 0.6) between E_{cut} and Γ, while if we consider sources with $1.78 < \Gamma < 2.0$, we found a negative correlation (correlation coefficient = 0.6) between E_{cut} and Γ. Beyond $\Gamma > 2.0$, no trend of E_{cut} with Γ is noticed, however, this apparent no-correlation is based on three sources. Thus this analysis gives indications of the existence of complicated correlation between E_{cut} and Γ. Though the reasons for this complicated behaviour is not clear presently, the existence of it too needs to be confirmed from more precise measurements of E_{cut} on a larger number of sources. For the sources lying in the negative correlation line in the E_{cut} versus Γ diagram, we plot in Fig. 5.6 the E_{cut} of those sources against their luminosity in the 2−10 keV band. We noticed a weak negative correlation with a correlation coefficient of 0.3 wherein sources with low E_{cut} have larger luminosity. This behaviour can be explained due to electrons in the corona being more effectively cooled via Comptonization in luminous sources, thereby leading to low E_{cut} as well as steeper Γ (Zhang et al. 2018). We however, note that the weak negative correlation obtained here is based on 6 measurements. Observations of more sources are needed to confirm or refute this observed correlation. From BeppoSAX measurement of nine sources, using data in the range of $0.1 - 200$ keV, Perola et al. (2002) found for the first time a strong positive correlation between E_{cut} and Γ. In their sample of nine sources, two have lower limits and some from the remaining seven have large error bars. From simulated Swift/BAT data Ricci et al. (2017) found a negative correlation between E_{cut} and Γ while Tortosa et al. (2018b) using a sample of 19 sources, found no correlation between E_{cut} and Γ. We also looked for correlation between E_{cut} and Eddington ratio ($\lambda_{Edd} = L_{Bol}/L_{Edd}$).

To estimate L_{Bol} for our sources we calculated the intrinsic (absorption corrected and k-corrected) continuum luminosity in 2− 10 keV using the following relation

$$L_{int} = 4\pi d_L^2 \frac{F_{int}}{(1+z)^{2-\Gamma}} \tag{5.1}$$

where F_{int} is the absorption corrected 2−10 keV flux and d_L is the luminosity distance. From L_{int}, L_{Bol} was calculated as $L_{Bol} = 20 \times L_{int}$ (Vasudevan & Fabian 2007). We did not find any correlation between E_{cut} and Eddington ratio. The correlation between E_{cut} and BH mass is shown in the top panel of Fig. 5.6. Also, shown in the same figure are unweighted linear least squares fit (magenta line) and weighted linear least squares fit (yellow line). There is an indication of a weak positive correlation. Recently, Tortosa et al. (2018b) found an anti-correlation between the coronal temperature and optical depth (τ) from an analysis of a sample of Seyfert galaxies. We in this work have first time measurement of E_{cut} for nine Seyfert galaxies. We tried to investigate the location of our nine new sources in the $KT_e - \tau$ plane and see if they lie on the trend found by Tortosa et al. (2018b). To calculate τ we used the approximation given by Pozdniakov et al. (1979) as

$$\Gamma = 1 + \frac{[2/(\theta+3) - log(\tau)]}{log(12\theta^2 + 25\theta)} \tag{5.2}$$

Similarly for KT_e, we used $KT_e = E_{cut}/2$ (Petrucci et al. 2001). We show in Fig. 5.7 the location of our sources in the KT_e versus τ plane both for slab and spherical geometry of the corona. Also, shown in the same figure are the sources with KT_e measurements from Tortosa et al. (2018b) as well as the relation found by Tortosa et al. (2018b) separately for the slab and spherical geometry. Our sources nicely lie in the trend found by Tortosa et al. (2018b).

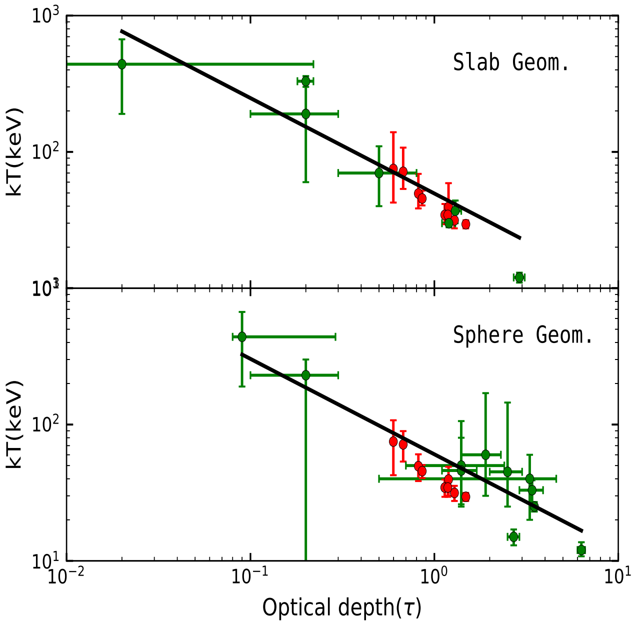

FIGURE 5.7: Coronal temperature versus optical depth for Seyfert galaxies in the case of slab geometry (top panel) and spherical geometry (bottom panel). The green filled circles are the measurements from Tortosa et al. (2018b) while the red filled circles are the new measurements from this work. The black solid lines are the relation from Tortosa et al. (2018b) separately for the disk and spherical shape of the corona.

5.8 Location of sources in the $\theta - l$ plane

We have E$_{cut}$ measurements for nine sources. To plot the location of our sources in the θ - l plane we converted out E$_{cut}$ measurements to θ using Equation (1.2) given in Chapter 1, where we used $K_BT_e = E_{cut}/2$ (Petrucci et al. 2001). Similarly for calculating l we used Equation (1.1) given in Chapter 1. Here, for the coronal radius we assumed a value of $10R_G$ (Fabian et al. 2015), as we do not have any measurement of the coronal size for our sources. For the luminosity of the sources, we used the absorption corrected 0.1−200 keV flux obtained from our spectral fits and converted to luminosity using the luminosity distance. Black hole masses for the sources were taken from literature. We show in Fig. 5.8 the location of our sources in the $\theta - l$ plane. Also shown in the same diagram is the pair line for

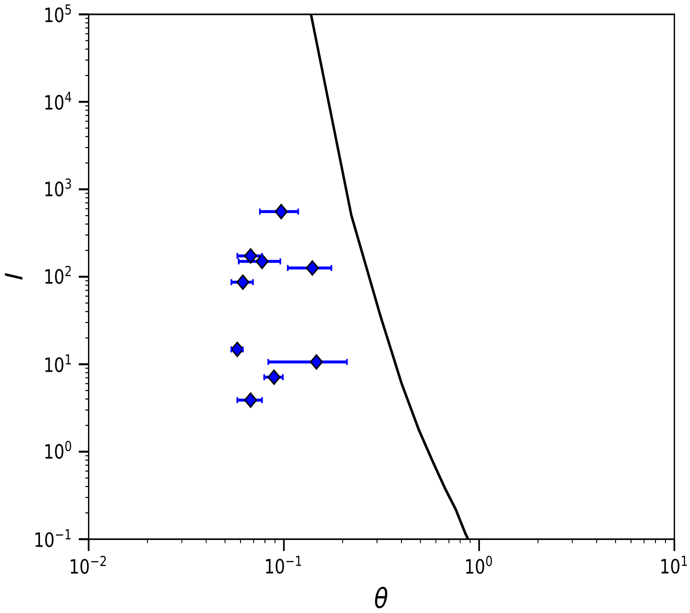

FIGURE 5.8: Location of our sources in the $\theta - l$ plane. The black solid line corresponds to the pair line for the slab coronal geometry.

a slab geometry (Stern et al. 1995; Fabian et al. 2015). All the sources for which E_{cut} has been derived in this work lie within the theoretical pair line, similar to that found by Fabian et al. (2015) and Kamraj et al. (2018).

5.9 Comparison with the coronal properties of other AGN

Because of the degeneracies involved in the evaluation of the properties of the corona from the observed X-ray spectrum, it is needed to simultaneously measure the power law slope and the cut off energy. Measurements of this demands high quality X-ray spectra. Measurements of E_{cut} were known for several AGN from observatories such as *BeppoSAX* and INTEGRAL. However, most of these measurements have large error bars. Recently, observations from *NuSTAR* have started to provide reliable estimates of E_{cut} in few AGN, even though it might not be sensitive to sources with E_{cut} much larger that its spectral coverage. To compare the coronal measurements reported here for Seyfert galaxies with that of other AGN, we searched the literature for the availability of coronal properties of AGN based on observations either from *NuSTAR* alone or *NuSTAR* observations coupled with other telescopes. Focussing only on those sources that have E_{cut} measurements we arrived at a sample of thirty sources. They are given in Table 5.3. Also, the sources listed in Table 5.3 belong to different types of AGN that includes both radio-quiet Seyferts and BLRGs (3C 390.3 and 3C 120, 3C 382 and 3C 390.3). Analysis of a larger sample of AGN do indicate differences between BLRGs and radio-quiet Seyfert 1 galaxies, with BLRGs having, on average lesser Compton reflection, weaker Fe Kα line and harder hard X-ray spectra compared to radio-quiet Seyfert 1 galaxies (Wozniak et al. 1998). These differences between BLRGs and radio-quiet Seyfert 1 galaxies are further confirmed by Zdziarski & Grandi (2001), however, the authors state that the distribution of these parameters in these two populations of sources is not distinct. Zdziarski & Grandi (2001) obtained mean values of Γ = 1.74 $\pm$ 0.04 and 1.95 $\pm$ 0.05 for BLRGs and radio-quiet Seyferts respectively. The value of Γ obtained for 3C 120 by us (Rani & Stalin 2018b) is closer to what is known for radio-quiet Seyfert 1 galaxies and is steeper than the other two BLRGs 3C 282 and 3C 390.3. This also supports the dormant state of the jet of 3C 120 during the epoch of *NuSTAR* observations reported here. Though the kT_e values of 3C 120 (Rani & Stalin 2018b) and 3C390.3 Lohfink et al. (2015) agree within a factor of two, the value of kT_e obtained for 3C 382 (Ballantyne et al. 2014) another BLRG is much larger. Therefore, based on existing data from *NuSTAR*, it is very difficult to say if the coronal properties of radio-loud AGN (BLRGs) and radio-quiet AGN (radio-quiet Seyfert 1 galaxies) are similar or different. Understanding the connection between radio-emission and coronal properties if any needs observations on a large number of sources of both types analysed in a homogeneous manner. For this modest sample of sources with *NuSTAR* observations culled from literature, we looked for correlation of E_{cut} with other physical parameters of the sources such as Γ and the black hole mass. No correlation could be established (Figure 5.6). Therefore, more and more measurement of kT_e on a large sample that comprises both radio-loud and radio-quiet AGN are needed to know for the existence or absence of such correlations and largely to better understand the nature of the corona in AGN.

5.10 Summary and conclusion

We have carried out X-ray spectral analysis of a sample of 11 sources, using data from *NuSTAR*. The aims of this work are two fold (a) to provide new measurements of E_{cut} in AGN and (b) look for correlations between E_{cut} values obtained only from *NuSTAR data* and other physical parameters of the sources. The results of this work are summarized below

1. In eight out of 11 sources, FeKα line was found, while for three sources, namely Mrk 348, NGC 2992 and NGC 7172, FeKα line could not be seen in their spectra.
2. Among the eleven sources whose spectra were analysed, E_{cut} values were obtained for nine sources. For one sources, ESO 362-G18, a lower limit to the E_{cut} value was estimated, while for NGC 7314, our spectral fits did not yield any E_{cut} value.
3. Using the new E_{cut} values obtained in this work along with those collected from literature, we could gather E_{cut} measurements for 30 sources. In this enlarged sample of 30 sources, we found no correlation between E_{cut} and M_{BH} and E_{cut} and λ_{Edd}. However, we noticed a complicated correlation between E_{cut} and Γ. For values of Γ less than 1.78, E_{cut} is positively correlated

with Γ, while for Γ values between 1.78 and 2.0, E_{cut} is negatively correlated with Γ.

Though there has been an increase in the number of AGN with E_{cut} measurements from *NuSTAR*, it is still insufficient. Therefore, to study various correlations and to put any constraints on the theory based on observations the number of E_{cut} measurements need to be increased. This also requires physical model fits to the observed data to infer many other parameters of the system, rather than phenomenological model fits, requiring high quality data from *NuSTAR*.

Chapter 6

Conclusions and Future Work

Flux variability behaviour of AGN is an established phenomenon. Since the first observation about six decades ago, AGN have been studied for flux variations at all accessible wavelengths on a range of time scales from minutes to years. In particular studying AGN flux variability on short time scales of the order of minutes is extremely important as it will help probe the inner most region of AGN that is not accessible to any direct imaging techniques. In spite of the many studies that are already available, we still do not have a clear understanding of the physical processes that causes flux variations in AGN. Among the various wavelengths that are suitable to probe the central regions of AGN through monitoring observations, hard X-ray band is the most suited as it is known to originate in the immediate vicinity of the black hole, and it is less prone to the effects of absorption. Though several studies exist on the flux variability behaviour of AGN on long time scales at energies less than 10 keV (Nandra et al. 1997; Fiore et al. 1998; Turner et al. 1999; Uttley et al. 2002; Markowitz et al. 2003; Soldi et al. 2008), our knowledge on the hard X-ray variability characteristics of AGN are very limited, particularly on time scales of the order of hours (Petrucci et al. 2000; Reis et al. 2012; Soldi et al. 2014; Paliya et al. 2015). Also, in all available studies on the hard X-ray flux characteristics of AGN, no comparative analysis of the flux variability between different types of AGN were available. This is needed and is also important as such a study, in addition to providing clues on the processes that cause flux variations in different classes of AGN can also test the unification model.

It is believed that the primary X-ray continuum emission is AGN is due to inverse Compton Scattering of UV and optical photons from the accretion disk by a hot compact region called the corona. This produces a power law X-ray continuum with a high energy cut-off. The shape of the power law continuum contains important information on the nature of the corona. Cut off measurements for AGN do exist in literature but they are from low sensitive instruments particularly at energies beyond 10 keV and thus have large error bars. Quality E_{cut} measurements are available for about a dozen AGN. Therefore, more sensitive instruments beyond 10 keV are needed to increase our E_{cut} measurements on more number of AGN. The launch of *NuSTAR* in the year 2012, the first hard X-ray focussing instrument and sensitive to the energy range between 3−79 keV has enabled the study of both hard X-ray flux variability as well as understanding the nature of the corona in AGN.

The strategy followed in this present thesis is to constrain the physical processes happening close to the central region of AGN, by carrying out spectral and timing analysis of the hard X-ray emission from AGN. From timing studies, the thesis aimed to address the differences if any in the hard X-ray variability characteristic of different classes of AGN on hour like time scales. Towards this we selected a sample of 335 AGN, that includes 24 BL Lac objects, 24 FSRQs, 20 NLsy1 galaxies, 121 Seyfert 1 galaxies and 146 Seyfert 2 galaxies. From spectral studies, the thesis aimed to understand the nature of the corona in AGN. For this we selected a sample of 12 AGN, having high S/N ratio data with net count in the 3−79 keV band greater than 0.1. Both the studies utilized the data from the hard X-ray telescope *NuSTAR*. The major findings of the present thesis are:

1. A total of 557 sets of observations on 335 sources were analysed for hard

X-ray flux variability. About 60% of the sources that were analysed showed flux variability. Among the various types of AGN, blazars (that includes FSRQs and BL Lacs) are found to be more variable than their radio-quiet counterparts namely the Seyfert galaxies. The increased variability in blazars relative to Seyfert galaxies could be due to the contribution of relativistic jets to the observed X-ray emission in blazars.

2. Among the different categories of AGN, NLSy1 galaxies showed the highest DC of variability of about 85%. This was followed by BL Lacs with a DC of about 67%. Seyfert galaxies have a DC of about 50%. FSRQs showed the lowest DC of about 30%.

3. Significant negative correlation was noticed between $F_{\rm var}$ and $M_{\rm BH}$ as well as $F_{\rm var}$ and luminosity in the 2-10 keV bands. Thus brighter AGN are less variable. Also, AGN hosted by massive black holes are less variable.

4. Of the 12 sources for which spectral analysis was carried out, E_{cut} measurements for 10 sources were obtained for the first time. For one source ESO 362-G18, we could obtain a lower limit to the E_{cut} value, while for NGC 7314, our spectral fits did not yield any E_{cut} value.

5. Combining our new E_{cut} measurements with those culled from literature, we could gather E_{cut} measurements for a total of 30 sources. Analysing these 30 sources, we noticed a complicated correlation between E_{cut} and Γ. For values of Γ less than 1.78 E_{cut} is positively correlated with Γ, while for Γ values between 1.78 and 2.0 E_{cut} is negatively correlated with Γ.

Outline of future research: Although BL Lacs showed large DC of variability relative to Seyfert galaxies, practically nothing is known at present if there is any difference in the hard X-ray variability between different classes of blazars divided based on the position of their synchrotron peak in their broad band spectral energy distribution. This requires the availability of more data on blazars which is likely to become available in the near future.

Also, in our sample, NLSy1 galaxies showed the highest DC of variability among all the other classes of AGN. NLSy1 galaxies have gained more prominence over the last decade after the discovery of γ-ray emission in about a dozen NLSy1 galaxies. Also, we still do not yet have a clear picture if these NLSy1 galaxies are hosted by low mass black holes or spiral galaxies. The timing studies carried out in this thesis will be carried forward, by performing the spectral analysis of these sources. The timing results, along with the spectral analysis which we intend to do in the future could provide some lead to the peculiar observational signatures shown by NLSy1 galaxies relative to the Seyfert category of AGN. Also, we plan to continue our efforts towards determination of E_{cut} measurements for a large sample of AGN utilizing more physical model fits to their observed X-ray spectra.

Bibliography

Abdo A. A., et al., 2010a, *Astrophys. J. Suppl.*, 188, 405

Abdo A. A., et al., 2010b, *Astrophys. J.*, 716, 30

Abdo A. A., et al., 2010c, *Astrophys. J.*, 720, 912

Acero F., et al., 2015, *Astrophys. J. Suppl.*, 218, 23

Ackermann M., et al., 2015, *Astrophys. J.*, 810, 14

Anders E., Grevesse N., 1989, , 53, 197

Arnaud K. A., 1996, in Jacoby G. H., Barnes J., eds, Astronomical Society of the Pacific Conference Series Vol. 101, Astronomical Data Analysis Software and Systems V. p. 17

Baldi R. D., Capetti A., Robinson A., Laor A., Behar E., 2016, *Mon. Not. Roy. Astron. Soc.*, 458, L69

Ballantyne D. R., et al., 2014, *Astrophys. J.*, 794, 62

Baloković M., et al., 2015, *Astrophys. J.*, 800, 62

Balucinska-Church M., McCammon D., 1992, *Astrophys. J.*, 400, 699

Barr P., Mushotzky R. F., 1986, *Nature*, 320, 421

Barthelmy S. D., et al., 2005, *Space Sci. Rev.*, 120, 143

Beckmann V., Barthelmy S. D., Courvoisier T. J.-L., Gehrels N., Soldi S., Tueller J., Wendt G., 2007, *Astron. Astrophys.*, 475, 827

Bentz M. C., Katz S., 2015, *Pub. Astron. Soc. Pac.*, 127, 67

Bhayani S., Nandra K., 2011, *Mon. Not. Roy. Astron. Soc.*, 416, 629

Boller T., Brandt W. N., Fink H., 1996, *Astron. Astrophys.*, 305, 53

Brenneman L. W., et al., 2014, *Astrophys. J.*, 781, 83

Brinkmann W., Papadakis I. E., den Herder J. W. A., Haberl F., 2003, *Astron. Astrophys.*, 402, 929

Buisson D. J. K., Fabian A. C., Lohfink A. M., 2018, *Mon. Not. Roy. Astron. Soc.*, 481, 4419

Burbidge E. M., 1967, *Astrophys. J. Lett.*, 149, L51

Caballero-Garcia M. D., Papadakis I. E., Nicastro F., Ajello M., 2012, *Astron. Astrophys.*, 537, A87

Cappi M., Matsuoka M., Comastri A., Brinkmann W., Elvis M., Palumbo G. G. C., Vignali C., 1997, *Astrophys. J.*, 478, 492

Chartas G., Kochanek C. S., Dai X., Poindexter S., Garmire G., 2009, *Astrophys. J.*, 693, 174

Cirasuolo M., Celotti A., Magliocchetti M., Danese L., 2003, *Mon. Not. Roy. Astron. Soc.*, 346, 447

Coppi P. S., 1999, in Poutanen J., Svensson R., eds, Astronomical Society of the Pacific Conference Series Vol. 161, High Energy Processes in Accreting Black Holes. p. 375 (`arXiv:astro-ph/9903158`)

Dadina M., 2007, *Astron. Astrophys.*, 461, 1209

Dauser T., Wilms J., Reynolds C. S., Brenneman L. W., 2010, *Mon. Not. Roy. Astron. Soc.*, 409, 1534

Dickey J. M., Lockman F. J., 1990, *Ann. Rev. Astron. Astrophys.*, 28, 215

Done C., Gierliński M., 2003, *Mon. Not. Roy. Astron. Soc.*, 342, 1041

Dove J. B., Wilms J., Maisack M., Begelman M. C., 1997, *Astrophys. J.*, 487, 759

Drake A. J., et al., 2009, *Astrophys. J.*, 696, 870

Edelson R., Turner T. J., Pounds K., Vaughan S., Markowitz A., Marshall H., Dobbie P., Warwick R., 2002, *Astrophys. J.*, 568, 610

Eracleous M., Halpern J. P., 1998, *Astrophys. J.*, 505, 577

Fabian A. C., 1999, Proceedings of the National Academy of Science, 96, 4749

Fabian A. C., Ballantyne D. R., Merloni A., Vaughan S., Iwasawa K., Boller T., 2002, *Mon. Not. Roy. Astron. Soc.*, 331, L35

Fabian A. C., et al., 2009, *Nature*, 459, 540

Fabian A. C., Lohfink A., Kara E., Parker M. L., Vasudevan R., Reynolds C. S., 2015, *Mon. Not. Roy. Astron. Soc.*, 451, 4375

Fabian A. C., Lohfink A., Belmont R., Malzac J., Coppi P., 2017, *Mon. Not. Roy. Astron. Soc.*, 467, 2566

Fanaroff B. L., Riley J. M., 1974, *Mon. Not. Roy. Astron. Soc.*, 167, 31P

Fiore F., Laor A., Elvis M., Nicastro F., Giallongo E., 1998, *Astrophys. J.*, 503, 607

Fitch W. S., Pacholczyk A. G., Weymann R. J., 1967, *Astrophys. J. Lett.*, 150, L67

Foschini L., Ghisellini G., Tavecchio F., Bonnoli G., Stamerra A., 2011, *Astron. Astrophys.*, 530, A77

Fossati G., Maraschi L., Celotti A., Comastri A., Ghisellini G., 1998, *Mon. Not. Roy. Astron. Soc.*, 299, 433

Gianní S., de Rosa A., Bassani L., Bazzano A., Dean T., Ubertini P., 2011, *Mon. Not. Roy. Astron. Soc.*, 411, 2137

Gierliński M., Zdziarski A. A., Poutanen J., Coppi P. S., Ebisawa K., Johnson W. N., 1999, *Mon. Not. Roy. Astron. Soc.*, 309, 496

Giommi P., Barr P., Pollock A. M. T., Garilli B., Maccagni D., 1990, *Astrophys. J.*, 356, 432

Goodrich R. W., 1989, *Astrophys. J.*, 342, 224

Grandi P., Sambruna R. M., Maraschi L., Matt G., Urry C. M., Mushotzky R. F., 1997, *Astrophys. J.*, 487, 636

Guilbert P. W., Fabian A. C., Rees M. J., 1983, *Mon. Not. Roy. Astron. Soc.*, 205, 593

Gupta A. C., Kalita N., Gaur H., Duorah K., 2016, *Mon. Not. Roy. Astron. Soc.*, 462, 1508

Haardt F., Maraschi L., 1991, *Astrophys. J. Lett.*, 380, L51

Haardt F., Maraschi L., 1993, *Astrophys. J.*, 413, 507

Haardt F., Maraschi L., Ghisellini G., 1994, *Astrophys. J. Lett.*, 432, L95

Haardt F., Maraschi L., Ghisellini G., 1997, *Astrophys. J.*, 476, 620

Halpern J. P., 1985, *Astrophys. J.*, 290, 130

Harris D. E., Mossman A. E., Walker R. C., 2004, *Astrophys. J.*, 615, 161

Harrison F. A., et al., 2013, *Astrophys. J.*, 770, 103

Ho L. C., Filippenko A. V., Sargent W. L. W., 1993, in American Astronomical Society Meeting Abstracts #182. p. 817

Ivezić Ž., et al., 2002, *Astron. J.*, 124, 2364

Johnson W. N., et al., 1993, *Astrophys. J. Suppl.*, 86, 693

Johnson W. N., McNaron-Brown K., Kurfess J. D., Zdziarski A. A., Magdziarz P., Gehrels N., 1997, *Astrophys. J.*, 482, 173

Kamraj N., Harrison F. A., Baloković M., Lohfink A., Brightman M., 2018, *Astrophys. J.*, 866, 124

Kara E., Fabian A. C., Cackett E. M., Uttley P., Wilkins D. R., Zoghbi A., 2013, *Mon. Not. Roy. Astron. Soc.*, 434, 1129

Kara E., García J. A., Lohfink A., Fabian A. C., Reynolds C. S., Tombesi F., Wilkins D. R., 2017, *Mon. Not. Roy. Astron. Soc.*, 468, 3489

Kellermann K. I., Sramek R., Schmidt M., Shaffer D. B., Green R., 1989, *Astron. J.*, 98, 1195

Kellermann K. I., Lister M. L., Homan D. C., Ros E., Zensus J. A., Cohen M. H., Russo M., Vermeulen R. C., 2003, in Takalo L. O., Valtaoja E., eds, Astronomical Society of the Pacific Conference Series Vol. 299, High Energy Blazar Astronomy. p. 117 (`arXiv:astro-ph/0211398`)

Kotilainen J. K., León-Tavares J., Olguín-Iglesias A., Baes M., Anórve C., Chavushyan V., Carrasco L., 2016, *Astrophys. J.*, 832, 157

Lanzuisi G., et al., 2014, *Astrophys. J.*, 781, 105

Lanzuisi G., et al., 2016, Astron. Astrophys., 590, A77

Lawrence A., Papadakis I., 1993, *Astrophys. J. Lett.*, 414, L85

Leighly K. M., 1999, *Astrophys. J. Suppl.*, 125, 317

Lenc E., Tingay S. J., 2009, *Astron. J.*, 137, 537

Lin Y. C., et al., 1993, *Astrophys. J. Lett.*, 416, L53

Lohfink A. M., et al., 2015, *Astrophys. J.*, 814, 24

Lohfink A. M., et al., 2017, *Astrophys. J.*, 841, 80

Lubiński P., Zdziarski A. A., Walter R., Paltani S., Beckmann V., Soldi S., Ferrigno C., Courvoisier T. J.-L., 2010, *Mon. Not. Roy. Astron. Soc.*, 408, 1851

Lubiński P., et al., 2016, *Mon. Not. Roy. Astron. Soc.*, 458, 2454

Ludlam R. M., Cackett E. M., Gültekin K., Fabian A. C., Gallo L., Miniutti G., 2015, *Mon. Not. Roy. Astron. Soc.*, 447, 2112

Magdziarz P., Zdziarski A. A., 1995, *Mon. Not. Roy. Astron. Soc.*, 273, 837

Maiolino R., Salvati M., Bassani L., Dadina M., della Ceca R., Matt G., Risaliti G., Zamorani G., 1998, *Astron. Astrophys.*, 338, 781

Malizia A., Molina M., Bassani L., Stephen J. B., Bazzano A., Ubertini P., Bird A. J., 2014, *Astrophys. J. Lett.*, 782, L25

Mao P., Urry C. M., Massaro F., Paggi A., Cauteruccio J., Künzel S. R., 2016, *Astrophys. J. Suppl.*, 224, 26

Maraschi L., Tavecchio F., 2003, *Astrophys. J.*, 593, 667

Markowitz A., Edelson R., Vaughan S., 2003, *Astrophys. J.*, 598, 935

Massaro E., Perri M., Giommi P., Nesci R., 2004, *Astron. Astrophys.*, 413, 489

Massaro E., Giommi P., Leto C., Marchegiani P., Maselli A., Perri M., Piranomonte S., Sclavi S., 2009, *Astron. Astrophys.*, 495, 691

Matt G., et al., 2015, *Mon. Not. Roy. Astron. Soc.*, 447, 3029

Matthews T. A., Sandage A. R., 1963, *Astrophys. J.*, 138, 30

Mayers J. A., et al., 2018, arXiv e-prints,

McHardy I., 2010, in Belloni T., ed., Lecture Notes in Physics, Berlin Springer Verlag Vol. 794, Lecture Notes in Physics, Berlin Springer Verlag. p. 203 (`arXiv:0909.2579`), doi:10.1007/978-3-540-76937-8˙8

McHardy I. M., Gunn K. F., Uttley P., Goad M. R., 2005, *Mon. Not. Roy. Astron. Soc.*, 359, 1469

Mickaelian A., 2015, Iranian Journal of Astronomy and Astrophysics, 2, 1

Middei R., et al., 2018, *Astron. Astrophys.*, 615, A163

Mushotzky R. F., Done C., Pounds K. A., 1993, *Ann. Rev. Astron. Astrophys.*, 31, 717

Nandra K., George I. M., Mushotzky R. F., Turner T. J., Yaqoob T., 1997, *Astrophys. J.*, 476, 70

Nandra K., O'Neill P. M., George I. M., Reeves J. N., 2007, *Mon. Not. Roy. Astron. Soc.*, 382, 194

Nicastro F., et al., 2000, *Astrophys. J.*, 536, 718

Nolan P. L., et al., 2012, *Astrophys. J. Suppl.*, 199, 31

O'Neill P. M., Nandra K., Papadakis I. E., Turner T. J., 2005, *Mon. Not. Roy. Astron. Soc.*, 358, 1405

Oh K., et al., 2018, *Astrophys. J. Suppl.*, 235, 4

Osterbrock D. E., Pogge R. W., 1985, *Astrophys. J.*, 297, 166

Paliya V. S., Böttcher M., Diltz C., Stalin C. S., Sahayanathan S., Ravikumar C. D., 2015, *Astrophys. J.*, 811, 143

Paliya V. S., Rajput B., Stalin C. S., Pandey S. B., 2016, *Astrophys. J.*, 819, 121

Pan H.-W., Yuan W., Zhou X.-L., Dong X.-B., Liu B., 2015, *Astrophys. J.*, 808, 163

Perola G. C., Matt G., Cappi M., Fiore F., Guainazzi M., Maraschi L., Petrucci P. O., Piro L., 2002, *Astron. Astrophys.*, 389, 802

Petrucci P. O., et al., 2000, *Astrophys. J.*, 540, 131

Petrucci P. O., et al., 2001, *Astrophys. J.*, 556, 716

Petrucci P.-O., et al., 2013, *Astron. Astrophys.*, 549, A73

Pian E., 2002, , 19, 49

Pian E., et al., 1998, *Astrophys. J. Lett.*, 492, L17

Ponti G., Papadakis I., Bianchi S., Guainazzi M., Matt G., Uttley P., Bonilla N. F., 2012, *Astron. Astrophys.*, 542, A83

Porquet D., et al., 2018, Astron. Astrophys., 609, A42

Poutanen J., Svensson R., 1996, *Astrophys. J.*, 470, 249

Poutanen J., Svensson R., Stern B., 1997, in Winkler C., Courvoisier T. J.-L., Durouchoux P., eds, ESA Special Publication Vol. 382, The Transparent Universe. p. 401 (`arXiv:astro-ph/9701168`)

Pozdniakov L. A., Sobol I. M., Siuniaev R. A., 1979, Pisma v Astronomicheskii Zhurnal, 5, 279

Press W. H., Teukolsky S. A., Vetterling W. T., Flannery B. P., 1992, Numerical recipes in C. The art of scientific computing

Rani P., Stalin C. S., 2018a, Journal of Astrophysics and Astronomy, 39, 15

Rani P., Stalin C. S., 2018b, *Astrophys. J.*, 856, 120

Rani P., Stalin C. S., Rakshit S., 2017, *Mon. Not. Roy. Astron. Soc.*, 466, 3309

Ravasio M., Tagliaferri G., Ghisellini G., Tavecchio F., Böttcher M., Sikora M., 2003, *Astron. Astrophys.*, 408, 479

Rees M. J., 1984, *Ann. Rev. Astron. Astrophys.*, 22, 471

Reis R. C., et al., 2012, *Astrophys. J.*, 745, 93

Ricci C., Walter R., Courvoisier T. J.-L., Paltani S., 2011, *Astron. Astrophys.*, 532, A102

Ricci C., et al., 2017, *Astrophys. J. Suppl.*, 233, 17

Ricci C., et al., 2018, *Mon. Not. Roy. Astron. Soc.*, 480, 1819

Richards J. L., et al., 2011, *Astrophys. J. Suppl.*, 194, 29

Risaliti G., Elvis M., Fabbiano G., Baldi A., Zezas A., 2005, *Astrophys. J. Lett.*, 623, L93

Risaliti G., Nardini E., Salvati M., Elvis M., Fabbiano G., Maiolino R., Pietrini P., Torricelli-Ciamponi G., 2011, *Mon. Not. Roy. Astron. Soc.*, 410, 1027

Romero G. E., Cellone S. A., Combi J. A., 1999, *Astron. Astrophys. Suppl.*, 135, 477

Ross R. R., Fabian A. C., 1993, *Mon. Not. Roy. Astron. Soc.*, 261, 74

Rybicki G. B., Lightman A. P., 1979, Radiative processes in astrophysics

Sahakyan N., Zargaryan D., Baghmanyan V., 2015, *Astron. Astrophys.*, 574, A88

Sambruna R. M., et al., 2006, *Astrophys. J.*, 646, 23

Seyfert C. K., 1943, *Astrophys. J.*, 97, 28

Shakura N. I., Sunyaev R. A., 1973, *Astron. Astrophys.*, 24, 337

Sillanpaa A., Haarala S., Valtonen M. J., Sundelius B., Byrd G. G., 1988, *Astrophys. J.*, 325, 628

Smith A. G., 1996, in Miller H. R., Webb J. R., Noble J. C., eds, Astronomical Society of the Pacific Conference Series Vol. 110, Blazar Continuum Variability. p. 3

Sobolewska M. A., Papadakis I. E., 2009, *Mon. Not. Roy. Astron. Soc.*, 399, 1597

Soldi S., et al., 2008, *Astron. Astrophys.*, 486, 411

Soldi S., et al., 2014, *Astron. Astrophys.*, 563, A57

Stern B. E., Poutanen J., Svensson R., Sikora M., Begelman M. C., 1995, *Astrophys. J. Lett.*, 449, L13

Tagliaferri G., et al., 2000, *Astron. Astrophys.*, 354, 431

Takahashi T., et al., 1996, *Astrophys. J. Lett.*, 470, L89

Takahashi T., et al., 2007, *Pub. Astron. Soc. Japan*, 59, 35

Tanaka Y. T., et al., 2015, *Astrophys. J. Lett.*, 799, L18

Tazaki F., Ueda Y., Ishino Y., Eguchi S., Isobe N., Terashima Y., Mushotzky R. F., 2010, *Astrophys. J.*, 721, 1340

Tazaki F., Ueda Y., Terashima Y., Mushotzky R. F., 2011, *Astrophys. J.*, 738, 70

Titarchuk L., 1994, *Astrophys. J.*, 434, 570

Tortosa A., et al., 2016, preprint, (`arXiv:1612.05871`)

Tortosa A., et al., 2018a, *Mon. Not. Roy. Astron. Soc.*, 473, 3104

Tortosa A., Bianchi S., Marinucci A., Matt G., Petrucci P. O., 2018b, Astron. Astrophys., 614, A37

Turner T. J., George I. M., Nandra K., Turcan D., 1999, *Astrophys. J.*, 524, 667

Ubertini P., et al., 2003, *Astron. Astrophys.*, 411, L131

Ulrich M.-H., Maraschi L., Urry C. M., 1997, *Ann. Rev. Astron. Astrophys.*, 35, 445

Urry C. M., Padovani P., 1995, *Pub. Astron. Soc. Pac.*, 107, 803

Ursini F., et al., 2015, *Mon. Not. Roy. Astron. Soc.*, 452, 3266

Uttley P., McHardy I. M., Papadakis I. E., 2002, *Mon. Not. Roy. Astron. Soc.*, 332, 231

Valtonen M. J., et al., 2016, *Astrophys. J. Lett.*, 819, L37

Vasudevan R. V., Fabian A. C., 2007, *Mon. Not. Roy. Astron. Soc.*, 381, 1235

Vasudevan R. V., Fabian A. C., 2009, *Mon. Not. Roy. Astron. Soc.*, 392, 1124

Vasudevan R. V., Brandt W. N., Mushotzky R. F., Winter L. M., Baumgartner W. H., Shimizu T. T., Schneider D. P., Nousek J., 2013a, *Astrophys. J.*, 763, 111

Vasudevan R. V., Mushotzky R. F., Gandhi P., 2013b, *Astrophys. J. Lett.*, 770, L37

Vaughan S., Edelson R., Warwick R. S., Uttley P., 2003, *Mon. Not. Roy. Astron. Soc.*, 345, 1271

Véron-Cetty M.-P., Véron P., 2010, *Astron. Astrophys.*, 518, A10

Wagner S. J., Witzel A., 1995, *Ann. Rev. Astron. Astrophys.*, 33, 163

Walker R. C., Benson J. M., Unwin S. C., 1987, *Astrophys. J.*, 316, 546

Wilkes B. J., Elvis M., 1987, *Astrophys. J.*, 323, 243

Wilms J., Allen A., McCray R., 2000, *Astrophys. J.*, 542, 914

Wojaczyński R., Niedźwiecki A., 2017, *Astrophys. J.*, 849, 97

Woo J.-H., Urry C. M., 2002, *Astrophys. J.*, 579, 530

Wozniak P. R., Zdziarski A. A., Smith D., Madejski G. M., Johnson W. N., 1998, *Mon. Not. Roy. Astron. Soc.*, 299, 449

Zamorani G., et al., 1981, *Astrophys. J.*, 245, 357

Zdziarski A. A., Grandi P., 2001, *Astrophys. J.*, 551, 186

Zdziarski A. A., Johnson W. N., Magdziarz P., 1996, *Mon. Not. Roy. Astron. Soc.*, 283, 193

Zdziarski A. A., Poutanen J., Johnson W. N., 2000, *Astrophys. J.*, 542, 703

Zensus J. A., 1989, in Maraschi L., Maccacaro T., Ulrich M.-H., eds, Lecture Notes in Physics, Berlin Springer Verlag Vol. 334, BL Lac Objects. p. 3, doi:10.1007/BFb0031137

Zhang J.-X., Wang J.-X., Zhu F.-F., 2018, *Astrophys. J.*, 863, 71

Zheng X. C., et al., 2017, *Astrophys. J.*, 849, 127

Zoghbi A., et al., 2017, *Astrophys. J.*, 836, 2

Zycki P. T., Czerny B., 1994, *Mon. Not. Roy. Astron. Soc.*, 266, 653